



TECHNISCHE
UNIVERSITÄT
DARMSTADT

Critical Phenomena in the Phase Diagrams of QCD-like Theories

Vom Fachbereich Physik
der Technischen Universität Darmstadt

zur Erlangung des Grades
eines Doktors der Naturwissenschaften (Dr.rer.nat.)

genehmigte Dissertation von
M.Sc. Nils Strodthoff
aus Bremen

Darmstadt 2013
D17

Referent: Priv. Doz. Dr. Lorenz von Smekal
Korreferent: Prof. Dr. Jochen Wambach

Tag der Einreichung: 16.10.2012
Tag der Prüfung: 28.11.2012

Summary

QCD is the well-established theory of strong interactions but of such a complex nature that outstanding open questions remain even after almost 40 years since its discovery. In this thesis we concentrate on aspects of finite density QCD and the deconfinement transition, which we study, however, not in QCD itself but in QCD-like theories that are obtained by deformations of the QCD Lagrangian.

In particular, we study effective models for 2-color QCD, adjoint QCD and QCD with isospin chemical potential as the three prototypical examples for QCD-like theories without a fermion sign problem and investigate their corresponding phase diagrams. One main tool in our analysis is the Functional Renormalization Group, which allows to consistently include quantum and thermal fluctuations and to study critical phenomena. A particular focus lies on two-color QCD, which provides a transparent demonstration of the impact of baryonic degrees of freedom: without them its phase diagram resembles that of corresponding 3-color model calculations including a critical endpoint which vanishes, however, inside the diquark condensation phase once one properly includes the diquarks as lightest baryonic degrees of freedom. Interesting relations to effective models for the BEC-BCS crossover in (non-relativistic) ultracold atomic gases arise, which are most transparently demonstrated in the comparison between QCD with isospin chemical potential and imbalanced Fermi gases. In the second part we study the deconfinement transition in 2+1 dimensional pure $SU(N)$ lattice gauge theories using universality methods.

Zusammenfassung

QCD ist die akzeptierte Theorie der starken Wechselwirkung. Sie ist jedoch so komplex, dass sogar fast 40 Jahre nach ihrer Entdeckung noch immer zahlreiche Fragen offenstehen. In dieser Arbeit konzentrieren wir uns auf Aspekte der QCD bei endlicher Dichte und des Deconfinement Phasenübergangs, welche wir jedoch nicht in der QCD direkt, sondern in QCD-artigen Theorien untersuchen, die man durch Deformation der QCD Lagrangedichte erhält.

Insbesondere studieren wir effektive Modelle für 2-Farb QCD, adjungierte QCD und QCD mit Isospin chemischem Potential, als die drei prototypischen Beispiele für QCD-artige Theorien ohne ein Fermion-Vorzeichenproblem, und untersuchen die entsprechenden Phasendiagramme. Ein wichtiges Werkzeug in dieser Analyse ist die Funktionale Renormierungsgruppe, die es erlaubt, konsistent Quanten- und thermische Fluktuationen zu berücksichtigen, und damit eine akkurate Beschreibung kritischer Phänomene ermöglicht. Ein besonderer Fokus liegt auf der 2-Farb QCD, die eine sehr transparente Veranschaulichung für die Relevanz baryonischer Freiheitsgrade liefert: ohne diese ähnelt ihr Phasendiagramm denen entsprechender 3-Farb-Modellrechnungen einschließlich eines kritischen Endpunktes. Dieser verschwindet jedoch in der Diquarkkondensationsphase, sobald die Diquarks als leichteste baryonische Freiheitsgrade konsistent berücksichtigt werden. Es ergeben sich interessante Parallelen zu der effektiven Beschreibung des BEC-BCS Crossovers in (nicht-relativistischen) ultrakalten Quantengasen, die am transparentesten anhand des Vergleichs zwischen QCD mit Isospin chemischen Potential und polarisierten Fermi Gasen demonstriert werden können. Im zweiten Teil der Arbeit untersuchen wir den Deconfinement Phasenübergang in 2+1 dimensionaler reiner $SU(N)$ Eichtheorie auf dem Gitter unter Verwendung von Universalitätsmethoden.

Contents

1. Introduction	1
2. The Functional Renormalization Group	11
2.1. Flow of the Effective Average Action	12
2.2. Flow of 2-Point Functions: Pole Masses and Spectral Functions	20
I. Effective Models for QCD-like Theories	29
3. Quark-Meson-Diquark Models for QCD-like Theories	31
3.1. Introduction	31
3.2. Symmetries and Model Construction	35
3.3. QMD Model for QC_2D : Mean-Field Analysis	46
3.4. QMD Model for QC_2D : FRG Analysis	57
3.5. Outlook: Extensions of the QMD Model for QC_2D	69
4. QCD with Isospin Chemical Potential	77
4.1. Symmetries and Model Construction	78
4.2. Phase Diagram of QCD with Isospin Chemical Potential	79
II. Universal Aspects of $SU(N)$ Gauge Theories in 2+1 Dimensions	87
5. $SU(N)$ Gauge Theories in 2+1 Dimensions—Universality and Self-Duality	89
5.1. Introduction	89
5.2. Twisted Boundary Conditions, Vortices, Universality and Self-Duality	90
5.3. Critical Couplings from Universality and Self-Duality	97
6. Summary and Outlook	103
A. Notations and Conventions	107
B. Flow Equations for the 2-point Functions in the $O(N)$ Model	109
C. $SU(2N)/Sp(N)$ and $SU(2N)/SO(2N)$ Cosets and their Properties	111
C.1. Coset Generators	111

Contents

C.2. Coset Properties	113
C.3. Transformation Properties of $\Psi^T \Sigma_i \Psi$	114
D. Flow Equations for the (P)QMD Model	115
D.1. Massive Energy Projectors	115
D.2. Flow of the Effective Potential in the PQMD Model	117
D.3. Improved Truncation	119
Bibliography	127

While the results presented in this thesis represent the author's original work several results were obtained in collaboration with other authors. Results on the spectral function in Chapter 2 were obtained in collaboration with Kazuhiko Kamikado, Lorenz von Smekal and Jochen Wambach. Parts of Chapter 3 are published in [1] together with Bernd-Jochen Schaefer and Lorenz von Smekal and Chapter 4 is partially based on [2]. The results from Chapter 5 are published in [3, 4] and were obtained in collaboration with Sam Edwards and Lorenz von Smekal.

1

Introduction

The strong force governs a wide range of phenomena, from nuclear physics to strong interaction processes at particle colliders, from color confinement in the vacuum to the quark-gluon plasma at extremely large temperatures determining the evolution of the universe microseconds after the Big Bang or neutron matter at extreme densities inside neutron stars. It is, besides electromagnetism and the weak force, one of the three fundamental forces described by the Standard Model of particle physics which constitutes together with gravity our present understanding of the laws of physics at the most fundamental level.

QCD as such dates back to the year 1973, the year of the discovery of asymptotic freedom by Gross, Wilczek and Politzer who were awarded the Nobel Prize in 2004 for this discovery [5]. However, even almost 40 years later several outstanding questions remain. What makes QCD so difficult to treat and at same time so fascinating as a research topic is the fact that it shows a number of non-perturbative phenomena like confinement, dynamical chiral symmetry breaking and color-superconductivity at large densities. The second complication comes from the fact that not only the effective couplings but also the relevant degrees of freedom are scale-dependent. While at large scales QCD is a theory of quarks and gluons the relevant degrees of freedom at lower scales are merely mesons and baryons. There are well-established effective theories valid at certain scales such as chiral perturbation theory for the low energy sector of QCD but to correctly incorporate the change in relevant degrees of freedom represents a major challenge for first principle approaches to QCD.

The main focus of this thesis lies in the study of QCD-like theories which are obtained by slight modifications of the QCD Lagrangian. Although these studies do not have direct predictive power for the 3-color case, they can help us to gain a better understanding of the mechanisms underlying QCD or even strongly coupled systems in general. In this thesis we concentrate on the one hand on aspects of QCD at finite

1. Introduction

density, which are studied within an effective model approach to QCD-like theories, and on the other hand on the confinement problem, which is studied in pure lattice gauge theory without quarks here particularly in 2+1 dimensions.

In the description of the QCD phase diagram, which aims at mapping out the state of strongly interacting matter as a function of temperature and density, the understanding of critical phenomena is essential. Here one requires appropriate theoretical tools to describe these phenomena accurately. In particular the question of the existence and the location of the critical point, where a first order phase boundary between the hadronic and the quark-gluon plasma phase disappears and turns into a crossover, serves as a benchmark of our understanding of the QCD phase diagram which can ultimately be tested in dedicated future experimental programs.

QCD—the theory of strong interactions

The QCD Lagrangian consists of a gauge sector described by a non-Abelian gauge theory with gauge group $SU(3)$ which is coupled to a matter sector of N_f flavors of quarks transforming in the fundamental representation of the gauge group. The Lagrangian reads explicitly

$$\mathcal{L}_{\text{QCD}} = -\frac{1}{4}G_{\mu\nu}^a G_a^{\mu\nu} + \bar{\psi}_i(i\not{D} - m_i)\psi_i, \quad (1.1)$$

with field strength tensor $G_{\mu\nu}^a = \partial_\mu A_\nu^a - \partial_\nu A_\mu^a - gf^{abc}A_\mu^b A_\nu^c$ and (color-)covariant derivative $D_\mu^{ab} = \partial_\mu \delta^{ab} + igA_\mu^c T_c^{ab}$, where f^{abc} denote the $SU(3)$ structure constants, T_c the generators of the fundamental representation and g the QCD gauge coupling which constitutes apart from the current quark masses m_i the only free parameter of the theory. The Lagrangian (1.1) is invariant under local gauge transformations $\Omega \in SU(N)$ of the form

$$\psi(x) \rightarrow \Omega(x)\psi(x), \quad A_\mu \rightarrow \Omega \left(A_\mu - \frac{i}{g}\partial_\mu \right) \Omega^\dagger. \quad (1.2)$$

QCD possesses two remarkable properties, *asymptotic freedom* and *confinement*, which have important physical consequences. Asymptotic freedom states the fact that the β -function which describes the scale dependence of the QCD coupling $\alpha_s = g^2/(4\pi)$ is negative, see Fig. 1.1(a), which implies that QCD gets weakly coupled at large momentum scales, i.e. large momentum transfers, thus allowing the use of perturbation theory. The downside is the fact that the coupling obtained from integrating such perturbative β -functions shows a Landau pole. This is, however, not a physical singularity but simply signals the breakdown of perturbation theory. Correspondingly, the description of phenomena at small scales such as bound state phenomena or confinement requires the use of non-perturbative techniques. The scale Λ_{QCD} where the coupling becomes of order one sets the only scale in the theory and represents the typical scale where non-perturbative effects set in.

Secondly, under confinement we understand the absence of color charged asymptotic

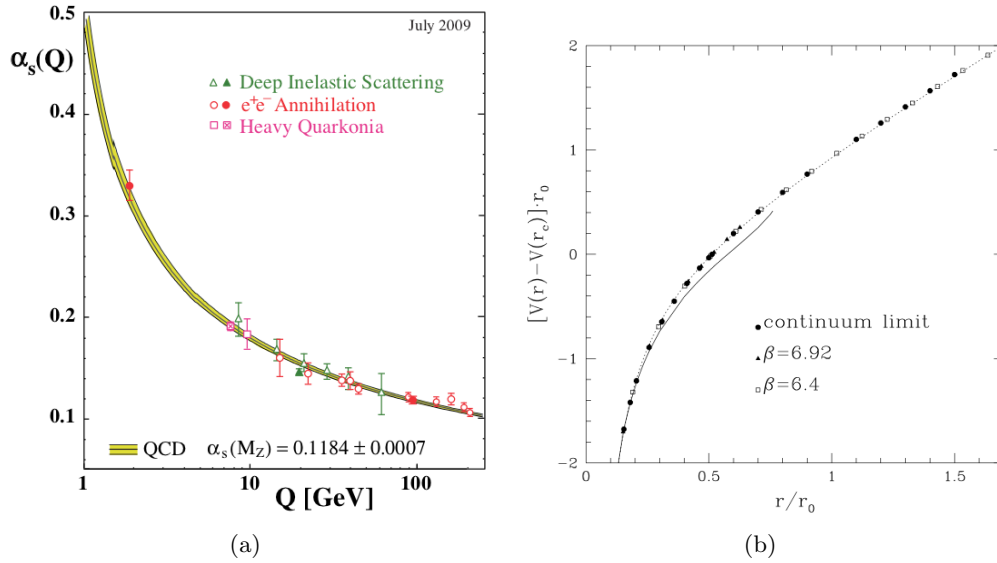


Figure 1.1.: Asymptotic freedom and confinement:

- (a) Scale dependence of the strong coupling constant α_s [6],
- (b) Static quark potential from pure $SU(3)$ lattice gauge theory [7]

states in the particle spectrum. Quark confinement can be understood in a simple picture where we image the chromoelectric flux between a quark and an antiquark to be squeezed into a flux-tube of small cross-section and constant energy density leading to a linear rise of the potential energy with the separation distance. Phenomenologically this picture can be used to explain Regge trajectories, i.e. the almost linear rise in spin with the squared mass, observed in meson resonances. The linear rise in the static quark potential can be observed directly in pure gauge theory on the lattice, see Fig. 1.1(b). The precise mechanism behind confinement is, however, still under debate. We will briefly introduce one such mechanism, the center vortex picture of confinement, in Chapter 5. In a theory with finite quark masses it is of course energetically favorable for the flux string to break at a certain separation via the formation of quark-antiquark pairs leading to a flattening of the static quark potential.

Chiral and deconfinement phase transitions

Before we come to the discussion of the QCD phase diagram, we have to discuss the chiral and the deconfinement phase transition along with the corresponding order parameters, which are associated to global symmetries of the QCD Lagrangian, namely *chiral symmetry* and *center symmetry*.

Firstly, the massless QCD Lagrangian from Eq. (1.1) with N_f quark flavors is invariant under independent global $U(N_f)$ transformations of the left/right-handed Weyl spinors $\psi_{L/R} = \frac{1}{2}(1 \pm \gamma^5)\psi$, i.e. transformations of the form $\psi_{L/R} \rightarrow U_{L/R}\psi_{L/R}$

1. Introduction

with $U_{L/R} \in U(N_f)$, giving rise to a symmetry group $U(N_f)_L \times U(N_f)_R$ or equivalently $SU(N_f)_V \times SU(N_f)_A \times U(1)_B \times U(1)_A$ in terms of vector/axial transformations, here written as acting on Dirac spinors again, given by

$$\psi \rightarrow e^{i\phi_i T_i} \psi \quad \text{and} \quad \psi \rightarrow e^{i\gamma^5 \phi_i T_i} \psi, \quad (1.3)$$

respectively, where T_i are the generators of $SU(N_f)$. Here, $U(1)_B$ ($U(1)_A$) transformations correspond to phase rotations of the left/right-handed quarks with the same (complex conjugate) phase factor. The axial $U(1)_A$ symmetry is broken anomalously at the quantum level. But even the remaining chiral symmetry group $SU(N_f)_V \times SU(N_f)_A$ is not realized in the ground state but broken spontaneously by effects of gluonic interactions to $SU(N_f)_V$ giving rise to $N_f^2 - 1$ Goldstone bosons. This is signaled by a nonvanishing *chiral condensate* $\langle \bar{\psi} \psi \rangle$, which plays the analogous role of the magnetization in a spin system. The remaining continuous global symmetry is given by $SU(N_f)_V \times U(1)_B$, where $U(1)_B$ is associated to baryon number conservation. Note that a finite current quark mass m_i mixes left- and right-handed components in the Lagrangian and thus breaks chiral symmetry explicitly, analogous to an external magnetic field in a spin system. However, it remains an approximate symmetry at least for the case of two light quark flavors whose current quark masses are small compared to the intrinsic scale Λ_{QCD} . The pions as (pseudo-) Goldstone bosons are then not exactly massless as in the chiral limit, but acquire a mass as described by the Gell-Mann-Oakes-Renner relation. As shown by Pisarski and Wilczek [8] for two massless quark flavors the finite-temperature chiral phase transition can be second order and was argued to be in the universality class of the $O(4)$ Heisenberg model [9]. For finite quark masses one observes on the lattice that the transition turns into a rapid crossover as chiral symmetry is only asymptotically restored.

Secondly, let us consider the opposite mass limit in the QCD Lagrangian (1.1), namely the limit of infinitely heavy quarks, which corresponds to the pure gauge limit. As gauge bosons do not represent the center of the gauge group, which is the discrete group Z_N in the case of an $SU(N)$ gauge theory, the pure gauge action is invariant under center transformations, see Eq. (1.2), which are, however, only periodic in the time direction up to a center element, i.e. $U(\vec{x}, \beta = 1/T) = zU(\vec{x}, 0)$ with $z \in Z_N$. We define the *Polyakov loop* via

$$P(\vec{x}) = \frac{1}{N_c} \mathcal{P} \text{Tr}_c \exp \left(\int_0^\beta d\tau A_0(\tau, \vec{x}) \right), \quad (1.4)$$

which is gauge invariant and transforms non-trivially under such center transformations as $P \rightarrow zP$. Here \mathcal{P} denotes path ordering and the trace is taken in the fundamental representation. At zero chemical potential the thermal expectation value $\langle P \rangle$ of the Polyakov loop serves as an order parameter for the deconfinement transition just like any quantity which transforms non-trivially under center transformations [10]. In the confined phase, where $\langle P \rangle = 0$, the theory is invariant under center transformations whereas in the deconfined phase, where $\langle P \rangle \neq 0$, the center symmetry is broken.

Thus deconfinement is associated with a breaking of center symmetry. Physically speaking, the negative logarithm of the expectation value of the Polyakov loop has an interpretation in terms of one half of the free energy $F_{q\bar{q}}$ of an infinitely separated static quark/anti-quark pair, which is finite in the deconfined phase and becomes infinite in the confined phase. As for chiral symmetry, which is only an exact symmetry in the chiral limit, center symmetry is only a symmetry of the pure gauge theory. Finite quark masses explicitly break center symmetry as quarks unlike gluons are sensitive to center transformations. This turns the deconfinement transition, which is a first order transition in pure $SU(3)$ gauge theory, into a rapid crossover with $T_c \approx 160$ MeV for 2+1 quark flavors at zero chemical potential [11]. An important question at this point is if the restriction of the discussion of the standard model to the QCD sector alone is perhaps too simple since the quarks carry also a fractional electric charge. The combined strong and electromagnetic interactions might then turn the transition into a proper phase transition again. This idea was investigated in first lattice studies [12, 13].

An interesting puzzle in finite temperature QCD is the question of the relation between the chiral and the deconfinement transition as lattice simulations indicate that the two transitions coincide for fundamental quarks [14]. A dynamical mechanism is expected to link the chiral dynamics in the matter sector to the confining dynamics of the gauge sector. Here an analytical description would be wishful, even in simplified models [15], which could provide an explanation for this phenomenon perhaps much like chiral symmetry breaking can be understood in terms of the gauge-coupling-dependent fixed-point structure of four-fermi interactions [16].

A glimpse at the QCD phase diagram

The understanding of a large number of physical processes in Nature involving the strong force do not only require knowledge about QCD in the vacuum but rather about its properties at finite temperatures and densities. This is the focus of the research on the *QCD phase diagram*, which aims at mapping out the state of strongly interacting matter as a function of temperature and density or equivalently baryon chemical potential which would then ultimately allow to understand a large number of different phenomena ranging from the early universe over neutron stars to heavy ion collisions [17]. The evolution of the early universe is described by finite temperature but approximately zero baryon chemical potential. The other axis of the phase diagram at small temperatures but large baryon chemical potential is relevant for the physics of neutron stars, where theoretical predictions of the equation of state can be directly tested against the increasingly strong constraints from neutron star observations [18, 19]. Finally, a successful theoretical understanding of present and future heavy-ion-collision experiments requires knowledge about the QCD phase diagram at finite temperatures and intermediate densities. It is, however, important to note that the purely static information from the QCD phase diagram is only one part of the full picture as dynamical effects such as the thermalization process and, correspondingly, questions of non-equilibrium dynamics play an important role. But even in the static case one

1. Introduction

has to investigate effects of finite volumes and for example strong magnetic fields in order to account for the typical conditions realized in heavy-ion-collision experiments.

The QCD phase diagram is subject to large research campaigns [20, 21, 22]. But in spite of joint theoretical and experimental efforts firm knowledge about the phase diagram of strongly interacting matter is still very limited. One reason for the theoretical difficulties in mapping out the phase diagram is the fact that Lattice QCD as first-principle approach to QCD suffers from a *sign problem* which designates the fact that the fermion determinant becomes complex at finite chemical potential and can thus no longer be interpreted as probability measure for standard Monte Carlo methods. The complex measure is, however, not just a technical complication but is required to describe physics such as different free energies of static color (anti-)charges at finite chemical potential [23]. It is important to note that the imaginary parts cancel when calculating expectation values and the sign problem just prevents an importance sampling configuration by configuration. The sign problem, its consequences and in particular QCD-like theories with positive fermion determinants will be discussed in detail in Chapter 3.

At zero chemical potential and for 2+1 quark flavors with physical quark masses lattice simulations predict that both the deconfinement and the chiral transition turn into rapid crossovers with coinciding transition temperatures which have converged to a value of 157(3) MeV [11]. These crossovers connect a confined *hadronic phase* and a *quark gluon-plasma (QGP) phase*, a deconfined phase where chiral symmetry is asymptotically restored, and are one of the few established facts about the QCD phase diagram. Furthermore, inside the hadronic phase one finds an experimentally well-established nuclear matter liquid-gas transition with a critical endpoint at a temperature of approximately 15 MeV while at very large chemical potentials perturbation theory predicts the occurrence of color-superconducting phases with different pairing patterns [24]. These phases are characterized by Cooper pairing of quarks induced by attractive 1-gluon exchange at asymptotically high chemical potentials as described by BCS theory. However, in particular the region of intermediate chemical potentials is rather poorly understood.

A commonly agreed minimal version of the QCD phase diagram which is consistent with these established facts is sketched in Fig. 1.2(a) where the hadronic phase and the QGP are separated via a first order transition at small temperatures and large chemical potentials. As it eventually has to turn into a crossover at zero chemical potential one expects the first order transition to end in a critical endpoint. This scenario is supported by effective model calculations for example in Polyakov-Nambu-Jona-Lasinio (PNJL) or Polyakov-Quark-Meson (PQM) models. However, already at this point it is worthwhile to point out that such model calculations completely neglect baryonic degrees of freedom, which are known to be particularly important at small temperatures and intermediate densities around the nuclear matter transition [19]. From the experimental point of view this argument is supported by the strong chemical potential dependence of chemical freeze-out lines in heavy-ion collisions at center-of-mass energies below about 10 GeV per nucleon pair [25] which is typically attributed to a rapid rise in baryonic density in this particular region of the phase

diagram.

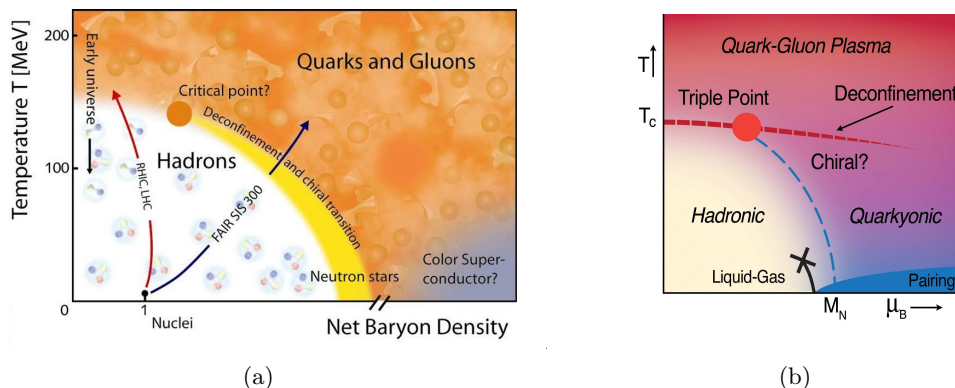


Figure 1.2.: Sketches of the QCD phase diagram:

- (a) Popular minimal QCD phase diagram [26],
- (b) Large- N_c inspired QCD phase diagram [27]

Alternative scenarios were inspired by large- N_c considerations [28, 29], where, unlike in 3-color QCD at finite temperature, the baryon density becomes an actual order parameter, and an additional *quarkyonic phase* arises which is characterized by confined matter with a high baryon density and possibly restored chiral symmetry. A large- N_c inspired sketch of the 3-color phase diagram [27] is shown in Fig. 1.2(b), where a triple point arises as coexistence point of the hadronic, the quarkyonic and the QGP phase. As the large- N_c limit does take in some sense baryonic degrees of freedom into account, this aspect of the QCD phase diagram might be reflected more realistically here than in the sketch of Fig. 1.2(a). We will reiterate the importance of baryonic degrees of freedom in an effective model calculation for 2-color QCD in Chapter 3.

The question of the existence and precise location of the critical endpoint serves as a benchmark for our understanding of the QCD phase diagram. From the theoretical side one aims at reconciling different methods to make predictions which can then ultimately be tested experimentally for example at the future CBM experiment at FAIR [22]. From the theoretical point of view, the existence of a CEP seems to be a rather unstable statement as not only the proper inclusion of baryonic degrees of freedom might lead to a disappearance of the critical point but also the inclusion of additional interaction channels such as vector or 't Hooft determinant interactions as observed in NJL model studies [30]. Another possible scenario is the occurrence of inhomogeneous crystalline phases in this particular region of the phase diagram where an inhomogeneous condensate is thermodynamically favored over a homogeneous one, which has for example been observed in NJL model studies [31]. Even though these statements may sound rather pessimistic for an experimental search for the critical endpoint it is, however, important to note that many of the scenarios discussed above lead to new distinguished points in the phase diagram such as triple points or Lifshitz points whose experimental signatures then have to be investigated, instead.

1. Introduction

QCD-like theories

Due to its complexity it is a promising approach to investigate not only QCD itself but also QCD-like theories obtained from various deformations of the QCD Lagrangian which may provide further insights into certain aspects of the full theory.

The most obvious modification is perhaps to vary the numbers of quark flavors which is particularly suited to study the chiral aspects of QCD. One popular account is to restrict the discussion of the matter sector to two light quark flavors. The low-temperature regime is then very well described by chiral perturbation theory, i.e. in the form of a non-linear sigma model which corresponds to a non-linear realization of chiral symmetry, where one parametrizes the vacuum manifold, i.e. the coset of chiral symmetry breaking, as central variable. However, this description necessarily breaks down at larger temperatures and alternative effective descriptions are required like the realization of the chiral symmetry breaking pattern $SU(2)_L \times SU(2)_R \times U(1)_B \rightarrow SU(2)_V \times U(1)_B$, which is locally isomorphic to $SO(4) \rightarrow SO(3)$, in terms of a linear sigma model which yields an accurate effective description of the chiral phase transition in 2-flavor QCD. Also the limit of a large number of flavors has been investigated [32, 33] as a controllable deformation of QCD to study the mechanism of chiral symmetry breaking and the phase structure as a function of the number of flavors.

In order to study the deconfinement transition, or to circumvent the sign problem, and hence to improve our understanding of QCD at finite density, it is insightful to consider also different gauge groups in the simplest case by adjusting the number of colors N_c . In the pure gauge limit we will be particularly interested in this thesis in cases where the deconfinement transition is a second order phase transition and hence universality arguments apply. Whereas this is only the case for $SU(2)$ in 3+1 dimensions, it applies to both $SU(2)$ and $SU(3)$ when reducing the number of spatial dimensions from three to two, see Chapter 5. Introducing quarks it is also helpful to study QCD-like theories with just two colors which are free from a fermion sign problem and will be discussed in detail in Chapter 3. Apart from considering a finite number of colors important insights were gained from large- N_c considerations, where the number of colors is sent to infinity [28] or even N_c along with the number of quark flavors N_f at a fixed ratio [29]. Even more radically, one can exchange the gauge group altogether and consider for example $SO(N)$, $Sp(N)$ or exceptional gauge groups such as G_2 [34, 35]. In the large- N_c limit interesting cross relations between different QCD-like theories with gauge groups $SO(2N_c)$, $Sp(N_c)$ in the presence of isospin and baryon chemical potential arise via an orbifold equivalence [36]. Also for finite N_c , at least on the level of chiral effective models, one can find maps between different theories such as 2-flavor 2-color QCD with baryon chemical potential and 2-flavor 3-color QCD with isospin chemical potential. But perhaps more surprisingly, effective descriptions for QCD-like theories can be set in direct correspondence to non-relativistic effective Lagrangians used for the description of the BEC-BCS crossover in ultracold atomic gases, which then manifests itself in common features in the phase diagrams of matter in such vastly different environments.

In this sense such investigations are not even specific to QCD and should be

considered as more than purely academic exercises as they can help to improve our understanding of the actual mechanisms underlying QCD or strongly coupled systems in general thereby allowing to connect seemingly different branches of physics like high energy physics, atomic physics or condensed matter physics.

Critical phenomena and universality

Universality in its broadest sense refers to a loss of memory of microscopic details of a given theory. The concept is intimately related to the occurrence of RG fixed points. The RG flow, to be discussed in detail in Chapter 2, describes the evolution from a microscopic classical action to the full quantum effective action and thus at the same time an evolution from a microscopical to a macroscopical description as all macroscopic properties of the system are determined by the effective action. Approaching an RG fixed point, the system becomes independent of the initial choice of parameters which correspond to IR irrelevant directions of the fixed point and is, apart from a few IR relevant parameters which remain to be fine-tuned, independent of the initially specified microscopic details of the theory.

The prototypical example of such a situation is the behavior of physical systems at a continuous phase transition, which is characterized by a diverging correlation length ξ . Near a second order phase transition for example, many thermodynamic properties of a system no longer depend on the microscopical details of the theory and can be grouped into universality classes of theories which share the same behavior at criticality. The universality hypothesis states that the universality class only depends on dimensionality, the symmetry group and the number of field components, see for example [37, 38]. These universality classes are characterized by critical exponents which describe scaling laws of physical observables around the phase transition. For example the order parameter ψ , the correlation length ξ , the specific heat C or the susceptibility χ show power law singularities as the reduced temperature $t = \frac{T-T_c}{T_c}$ approaches zero,

$$\psi \sim (-t)^\beta \text{ (for } t < 0), \quad \xi \sim |t|^{-\nu}, \quad C \sim |t|^{-\alpha}, \quad \chi \sim |t|^{-\gamma}, \quad (1.5)$$

which defines the critical exponents β, ν, α and γ . Furthermore, one defines critical exponents δ and η via scaling laws for the external source J and the spatial correlation function of the order parameter at criticality ($t = 0$)

$$J \sim \psi^\delta, \quad \langle \psi(0)\psi(r) \rangle \sim r^{-d+2-\eta}. \quad (1.6)$$

These critical exponents are, however, not all independent but connected via scaling relations [37] such as

$$(2 - \alpha) = \beta(\delta + 1), \quad \gamma = \nu(2 - \eta). \quad (1.7)$$

Below the upper critical dimension in addition hyperscaling relations apply whereas above and at this critical dimension mean-field critical exponents become exact.

1. Introduction

In particular in Section 3.4.2 we will investigate the chiral symmetry breaking transition in 2-color QCD with two quark flavors which corresponds to a symmetry breaking pattern $SO(6) \rightarrow SO(5)$ in close analogy to the well-studied chiral transition of $O(4)$ universality class in 3-color 2-flavor QCD. In Chapter 5 we discuss another example of universality in pure $SU(N_c)$ gauge theories in 2+1 dimensions whose universal behavior is that of N_c -state Potts models in two dimensions.

Outline of the thesis

After this brief introduction to the main topics of the thesis the following chapter is devoted to the Functional Renormalization Group (FRG) as one of the central tools employed in this thesis. In particular, we will sketch the derivation of the central equation in this approach, the Wetterich equation, which describes the scale evolution of the effective average action. We will also discuss the corresponding flow equations for 2-point functions in a particularly simple truncation and discuss the computation of real-time quantities such as pole masses or spectral functions. We will begin Chapter 3 with a general introduction to QCD-like theories with positive fermion determinants and outline the construction of the corresponding effective chiral Lagrangians. Here the 2-color case will be investigated in great detail both in the mean-field approximation and in an FRG approach and possible future extensions will be discussed in the form of an outlook section. In the course of the analysis we will discuss many topics which are not specific for example to 2-color QCD but of general relevance for effective model calculations, both in the mean-field approximation and in the FRG, such as a proper mass definition required for parameter fixing or the impact of thermal and vacuum contributions on the phase diagram. Chapter 4 deals with the case of isospin chemical potential which will be shown to be closely related to the 2-color case but allows in addition to study the interplay of both finite isospin and baryon chemical potentials. Furthermore, its phase diagram shows interesting similarities to that of imbalanced Fermi gases. The second part of the thesis is marked by Chapter 5 where we study the deconfinement transition in pure $SU(N)$ gauge theories on the lattice based on universality methods. An overall summary and a general outlook is presented in Chapter 6.

2

The Functional Renormalization Group

The Functional Renormalization Group (FRG) is a powerful tool to address in particular non-perturbative effects in quantum field theory and statistical physics and stands in the tradition of Wilsonian renormalization group approaches [39, 40].

The central object in the approach pioneered by Wetterich [41] is the *effective average action* Γ_k which can be seen as a scale-dependent generalization of the effective action, see [42, 43, 44, 45, 46] for general reviews and introductions. The scale k can be pictured as momentum scale associated to an IR regulator which essentially suppresses fluctuations from momentum modes with momenta smaller than k . The effective average action thus contains fluctuations from momentum modes with momenta larger than k and the evolution of the effective average action with the scale k is described by an exact flow equation which can then be used to gradually integrate out quantum and thermal fluctuations thereby interpolating between a classical bare action specified at some UV scale $k = \Lambda_{UV}$ and the full quantum effective action at $k = 0$, where the regulator is completely removed. The flow equation together with the specification of the bare action at UV scale $k = \Lambda_{UV}$ can be seen as definition of the quantum field theory. The full flow equation can rarely be solved exactly as this would correspond to an exact evaluation of the path integral and one usually has to resort to truncations. One of the particular strengths of the FRG lies here in its flexibility with respect to different non-perturbative expansion schemes.

In this chapter we will introduce the flow equation for the effective average action, and discuss different truncation schemes as well as numerical solution methods. In the following section we consider the flow of the 2-point function in a particularly simple truncation mainly focusing on the computation of real-time quantities such as pole masses and spectral functions.

2.1 Flow of the Effective Average Action

2.1.1. Generating functionals

We start by introducing some basic concepts such as different generating functionals with particular relevance in functional approaches, see e.g. [47, 48] for general introductions. For conceptual simplicity we will consider a single real scalar field and restrict ourselves to zero temperature in this section. To solve a quantum field theory it is sufficient to compute the partition function

$$Z[J] = \int \mathcal{D}\phi e^{-S[\phi] + \int_x J(x)\phi(x)} \quad (2.1)$$

as all correlation functions can be obtained by taking appropriate functional derivatives with respect to the source J such as 2-point functions

$$\langle \phi(x)\phi(y) \rangle = \frac{1}{Z[J=0]} \frac{\delta^2 Z[J]}{\delta J(x)\delta J(y)} \Bigg|_{J=0} = \langle \phi(x) \rangle \langle \phi(y) \rangle + \langle \phi(x)\phi(y) \rangle_c. \quad (2.2)$$

As the last equation already suggests, the partition function as generating functional contains redundant information as it contains disconnected contributions. It is more convenient to work with the *Schwinger functional* $W[J] = \log Z[J]$, which is the generating functional of connected Green's functions [47]. In the following we will, however, work with a different generating functional, the *effective action* $\Gamma[\Phi]$, which is defined as Legendre transform of the Schwinger functional

$$\Gamma[\Phi] = \int_x J\Phi - W[J], \quad (2.3)$$

with classical field $\Phi(x)$ defined via

$$\Phi(x) = \langle \phi(x) \rangle = \frac{\delta}{\delta J(x)} W[J]. \quad (2.4)$$

As a property of the Legendre transformation, the effective action is a convex functional of Φ . $\Gamma[\Phi]$ is the generating functional of 1-particle irreducible vertices and full propagators [47]. The dynamics of the field expectation value Φ is governed by the quantum equation of motion

$$\frac{\delta}{\delta \Phi(x)} \Gamma[\Phi] = J(x), \quad (2.5)$$

which is an exact equation in the sense that it includes all contributions from both thermal and quantum fluctuations. Evaluating the effective action for a constant field configuration $\bar{\Phi}$ yields the *effective potential* $U(\bar{\Phi})$ up to a volume factor, $\Gamma(\bar{\Phi}) = \mathcal{V}U(\bar{\Phi})$, which evaluated at its minimum coincides with the thermodynamic grand potential. Thus its value yields the negative of the pressure and further thermodynamic

observables such as particle densities, entropy density or energy density can be obtained via appropriate derivatives.

It is important to note that as all generating functionals are functionally related they contain in principle the same information. The fact that the knowledge of a generating functional completely specifies the underlying QFT suggests that it might be rather difficult to compute these in closed form expressions and indeed this is practically only possible in a few exceptional cases like in free field theories. Here lies the particular strength of renormalization group approaches which do not aim at integrating out all fluctuations at once but rather gradually (at least numerically) momentum-shell by momentum-shell in momentum space.

2.1.2. The flow equation for the effective average action

In this section we derive the flow equation for the scale-dependent effective average action. We try to illustrate the relations to the previous section as transparently as possible but to keep the formulation more general we consider a vector (ϕ_i) of fields which may contain both fermionic and bosonic fields such as the row vector $(\phi(p))_i = (\varphi(p), \psi(p), \bar{\psi}^T(-p))$, see also [49] for further details. Here the index refers to different components of ϕ and further internal indices are suppressed. Furthermore, we define a generalized scalar product which includes both a summation over internal indices and an integration over position/momentum space. The same applies to traces which are always understood as traces over internal indices and position/momentum space. We start by defining a scale-dependent partition function $Z_k[J]$ in analogy to Eq. (2.1) via

$$Z_k[J] = \int \mathcal{D}\phi \exp(-S[\phi] - \Delta S_k[\phi] + J_a^T \cdot \phi_a), \quad (2.6)$$

where we introduced a regulator functional

$$\Delta S_k[\phi] = \frac{1}{2} \phi_a^T \cdot (R_k)_{ab} \cdot \phi_b = \frac{1}{2} \int_p \phi_a^T(-p) (R_k)_{ab}(p) \phi_b(p). \quad (2.7)$$

The choice of the regulator R_k is in principle arbitrary within the following limitations:

1. It has a finite IR limit $p^2/k^2 \rightarrow 0$, i.e. it serves as an IR regulator.
2. It vanishes in the limit $k^2/p^2 \rightarrow 0$, which means in particular for $k \rightarrow 0$ one recovers the full quantum effective action as $\lim_{k \rightarrow 0} \Gamma_k \rightarrow \Gamma$.
3. It diverges as $k \rightarrow \infty$ or $k \rightarrow \Lambda_{UV}$ respectively. This means the saddle point approximation of the effective action becomes exact and correspondingly $\Gamma_k \rightarrow S_{cl}$.

Next we define the analogue of the generating functional for connected Green's functions

$$W_k[J] = \log Z_k[J], \quad (2.8)$$

2. The Functional Renormalization Group

and a corresponding classical field Φ_a analogous to Eq. (2.4) which now also depends on the scale k as it is related to the scale-dependent $W_k[J]$

$$\Phi_a \equiv \langle \phi_a \rangle_J = \frac{\overrightarrow{\delta}}{\delta J_a^T} W_k[J], \quad (2.9)$$

where we defined $\langle \mathcal{O} \rangle_J = \frac{1}{Z_k} \text{Tr} [\mathcal{O} Z_k]$. It is easy to derive a flow equation for W_k by just applying the scale derivative $\partial_t = k \frac{\partial}{\partial k}$ to the definition of W_k as the only scale dependence stems from the regulator:

$$\begin{aligned} \partial_t W_k &= -\langle \Delta S_k \rangle_J = \frac{1}{2} \langle \phi_a^T (\partial_t R_k)_{ab} \phi_b \rangle_J \\ &= \mp \frac{1}{2} \langle \text{Tr} \phi_b \phi_a^T (\partial_t R_k)_{ab} \rangle_J \\ &= \mp \frac{1}{2} \frac{1}{Z_k} \text{Tr} \left[\left(\frac{\overrightarrow{\delta}}{\delta J_a^T} \frac{\overrightarrow{\delta}}{\delta J_b} Z_k[J] \right) (\partial_t R_k)_{ab} \right], \end{aligned} \quad (2.10)$$

where here and in the following the lower sign applies to the purely fermionic subspace i.e. if both indices are fermionic. To derive the flow equation for W_k it remains to rewrite the last term in Eq. (2.10) in terms of W_k by using

$$\begin{aligned} (W_k^{(2)})_{ba} &\equiv \frac{\overrightarrow{\delta}}{\delta J_b^T} \frac{\overrightarrow{\delta}}{\delta J_a} W_k[J] = \frac{\overrightarrow{\delta}}{\delta J_b^T} \left(\frac{1}{Z_k} \frac{\overrightarrow{\delta}}{\delta J_a} Z_k[J] \right) \\ &= -\Phi_b \Phi_a^T + \frac{1}{Z_k} \frac{\overrightarrow{\delta}}{\delta J_b^T} \frac{\overrightarrow{\delta}}{\delta J_a} Z_k. \end{aligned} \quad (2.11)$$

This yields the flow equation for W_k ,

$$\begin{aligned} \partial_t W_k &= -\frac{1}{2} \text{Tr} \left[\left(\pm W_k^{(2)} \right)_{ba} \pm \Phi_b \Phi_a^T \right] (\partial_t R_k)_{ab} \\ &= -\frac{1}{2} \text{STr} [W_k^{(2)} \partial_t R_k] - \frac{1}{2} \Phi_a^T \cdot (\partial_t R_k)_{ab} \cdot \Phi_b, \end{aligned} \quad (2.12)$$

where the supertrace (STr) is a trace which includes an additional minus sign in the purely fermionic subspace. Our actual quantity of interest is the *effective average action*, the scale-dependent analogue of the effective action from Eq. (2.3), which is defined via a modified Legendre transformation of W_k as

$$\Gamma_k[\Phi] \equiv J_a^T \cdot \Phi_a - W_k[J[\Phi]] - \Delta S_k[\Phi]. \quad (2.13)$$

The fact that the regulator vanishes in the IR ensures the convexity of the effective action $\Gamma = \Gamma_{k=0}$, however, not at a finite scale k where the regulator is still present. The final step is now the derivation of the flow equation for the effective average action

$$\partial_t \Gamma_k = -\partial_t W_k + \partial_t \Delta S_k[\Phi] = \frac{1}{2} \text{STr} [W_k^{(2)} \partial_t R_k] \quad (2.14)$$

which we again rewrite using the identity

$$(\Gamma_k^{(2)} + R_k)_{ba} \equiv \frac{\overrightarrow{\delta}}{\delta \Phi_b^T} \Gamma_k \overleftarrow{\delta} \Phi_a + (R_k)_{ba} = \left(\frac{\overrightarrow{\delta}}{\delta J_b^T} \frac{\overrightarrow{\delta}}{\delta J_a} W_k \right)^{-1}, \quad (2.15)$$

2.1. Flow of the Effective Average Action

which is in turn a consequence of the analogue of the quantum equation of motion from Eq. (2.5)

$$(\Gamma_k + \Delta S_k) \overleftarrow{\frac{\delta}{\delta \Phi_b}} = J_b^T. \quad (2.16)$$

The flow equation for the effective average action, the *Wetterich equation*, now takes a simple 1-loop form, however, involving full propagators

$$\partial_t \Gamma_k = \frac{1}{2} \text{STr} \left[\left(\Gamma_k^{(2)} + R_k \right)^{-1} \partial_t R_k \right]. \quad (2.17)$$

More explicitly separating bosonic (B) and fermionic contributions (F, \bar{F}^T)¹ in a basis of the generic form $\Phi(p) = (B(p), F(p), \bar{F}^T(-p))$

$$\Gamma_k^{(2)}(q, p) = \begin{pmatrix} \Gamma_{k,BB}^{(2)} & \Gamma_{k,BF}^{(2)} & \Gamma_{k,B\bar{F}}^{(2)} \\ \Gamma_{k,FB}^{(2)} & \Gamma_{k,FF}^{(2)} & \Gamma_{k,F\bar{F}}^{(2)} \\ \Gamma_{k,\bar{F}B}^{(2)} & \Gamma_{k,\bar{F}F}^{(2)} & \Gamma_{k,\bar{F}\bar{F}}^{(2)} \end{pmatrix} \quad R_k(p) = \begin{pmatrix} R_{k,B}(p^2) & 0 & 0 \\ 0 & 0 & -R_{k,F}^T(-p) \\ 0 & R_{k,F}(p) & 0 \end{pmatrix}, \quad (2.18)$$

where e.g. $\Gamma_{k,\bar{F}\bar{F}}^{(2)}(p, q) = -\Gamma_{k,\bar{F}F}^{(2)}(-q, -p)^T$ etc. one can write Eq. (2.17) as

$$\partial_t \Gamma_k = \frac{1}{2} \text{Tr} \left[\left(\Gamma_k^{(2)} + R_k \right)_{BB}^{-1} \partial_t R_{k,B} \right] - \text{Tr} \left[\left(\Gamma_k^{(2)} + R_k \right)_{\bar{F}\bar{F}}^{-1} \partial_t R_{k,F} \right], \quad (2.19)$$

which is represented diagrammatically in Fig. 2.1.

$$\partial_t \Gamma_k = \quad + \frac{1}{2} \quad \begin{array}{c} \text{---} \bigcirc \text{---} \\ \text{---} \bigcirc \text{---} \end{array} - \begin{array}{c} \bigcirc \\ \bigcirc \end{array}$$

Figure 2.1.: Flow of the effective average action. Crossed circles represent regulator insertions $\partial_t R_k$. Solid (dashed) lines correspond to full scale- and field-dependent fermionic (bosonic) propagators.

Let us conclude this section with a few remarks. Although it may seem that we used the path integral to derive the flow equation, the flow equation from Eq. (2.17) together with the specification of the action in the UV can be used as an alternative definition of quantum field theory, which is completely independent of the path integral formalism and relies only on the existence of a finite renormalized Schwinger functional [44].

Note that the flow equation Eq. (2.17) is both IR and UV finite. In the infrared the regulator serves as an effective mass term whereas its scale derivative $\partial_t R_k$, which

¹As usual in Euclidean signature F and \bar{F} are considered as independent degrees of freedom but the corresponding transposed quantities are not.

2. The Functional Renormalization Group

appears in the flow equation, is peaked around k thereby rendering the equation also UV finite. One can easily recover standard perturbation theory [50] by solving the flow equation iteratively order by order starting with the classical action as zeroth order in the loop expansion.

By construction, the effective average action after integrating the flow coincides with the full quantum effective action and is thus independent of the regulator choice, which will only affect the path in theory space, i.e. the space of all coupling constants, from the bare action to the effective action. This is, however, only true as long as one considers the full theory. As soon as we are dealing with truncations also the endpoint of the flow will be regulator dependent which is intimately related to the topic of optimization [44, 51]. Here one tries to find an optimal regulator for a given truncation that minimizes the difference to the result obtained from the full theory. We will briefly touch upon the question of regulator choices and the related topic of optimization in Section 3.4.1.

2.1.3. Truncation schemes

The flow equation can rarely be solved exactly which requires the use of truncations. In this respect the large number of systematic expansion schemes is a particular strength of the FRG. At this point we stress the non-perturbative nature of these schemes which provide a systematic expansion of the effective average action and unlike perturbation theory do not require an explicit small expansion parameter. The two most popular truncation schemes are the vertex expansion [52] and the derivative expansion [42, 43].

The *vertex expansion* is an expansion in terms of vertex functions corresponding to an Ansatz for the effective average action of the form

$$\Gamma_k = \sum_{n=0}^{\infty} \frac{1}{n!} \int_{x_1, \dots, x_n} \Gamma_k^{(n)}(x_1, \dots, x_n) (\phi(x_1) - \bar{\phi}(x_1)) \cdots (\phi(x_n) - \bar{\phi}(x_n)), \quad (2.20)$$

here written schematically for a single scalar field expanded around a background $\bar{\phi}$. The flow equations for the 1-particle irreducible vertices $\Gamma_k^{(n)}$ can be obtained by functional differentiation of the flow equation. They constitute an infinite tower of coupled equations which are often referred to as differential analogues of Dyson-Schwinger equations. On the one hand this expansion gives in principle access to the full momentum dependent vertices but on the other hand unlike in the derivative expansion it is often hard to access the order parameter as it does not appear as an explicit variable in the expansion.

The *derivative expansion* is an expansion in momentum space corresponding to an Ansatz for the effective average action again written schematically as

$$\Gamma_k = \int_x U_k(\phi^2) + \frac{1}{2} Z_k(\partial_\mu \phi \partial^\mu \phi) + \mathcal{O}(\partial^4). \quad (2.21)$$

In the lowest order derivative expansion or local potential approximation (LPA) only a scale-dependent effective potential U_k is taken into account while the wavefunction

renormalization Z_k is set to one. The first step beyond the LPA often referred to as LPA' involves a scale-dependent but field independent wave function renormalization. Higher orders in the derivative expansion then include a field-dependent wave function renormalization and higher order derivative terms. The derivative expansion is particularly suited to describe critical phenomena since the order parameter typically appears explicitly as a variable. The application of the derivative expansion leads to very accurate results e.g. for critical exponents in $O(N)$ models at higher orders in the derivative expansion [42, 53, 54] but to a surprising degree already also in the LPA [55]. Note that the derivative expansion includes contributions from all orders in the vertex expansion, however, in a truncated form and corresponds to the resummation of an infinite number of perturbative diagrams.

Furthermore, there are truncation schemes which aim to compute full momentum dependent n -point functions. One popular example is the *BMW approximation* [56, 57], where one uses assumptions on the external momentum dependence of $(n + 1)$ - and $(n + 2)$ -point functions to set up a coupled system of flow equation for n -point functions retaining full external momentum dependence. We will propose an even simpler truncation to obtain momentum dependent 2-point functions and discuss its relation to the BMW approximation in Section 2.2. A different approach employed in [58] aims at truncating only at the level of the effective action and not at the level of the proper vertices, as it is done in the BMW approximation, which requires to introduce non-local contributions to the potential. Finally we would like to mention a different approach [59] generalizing the vertex expansion which aims at extending the flow equations for irreducible vertex functions into the broken phase by augmenting the system of flow equations by an equation for the order parameter.

2.1.4. Numerical solution methods

The flow equations for a physical system in a given truncation for the effective action constitute a set of differential equations for (coupling) constants, functions like the effective potential or even functionals describing their evolution with the RG scale k . For increasingly sophisticated truncations these equations can only rarely be solved analytically and remain to be solved numerically. This represents in general an additional systematic error in addition to the truncation error as for example functions have to be represented by a finite number of values during the numerical evolution from which the function has to be reconstructed in order to evaluate the right hand side of the flow equation. Such a prescription has to be specified in order to completely fix the used approximation scheme [60].

In the following we will discuss two such prescriptions in the form of numerical solution methods for the flow equation of the effective potential and address in particular their applicability to effective potentials parametrized by several invariants. The two most popular approaches are Taylor expansions about a scale-dependent expansion point and grid methods which solve for the effective potential on a discrete set of grid points in field space.

2. The Functional Renormalization Group

Taylor expansions

Due to its simplicity the probably most frequently used solution method is a Taylor expansion with a scale-dependent expansion point. This corresponds to an expansion of the effective potential of the form

$$U_k(\phi^2, \sigma) = \sum_{n=0}^K \frac{a_{n,k}}{n!} (\phi^2 - \phi_k^2)^n - c\sigma, \quad (2.22)$$

which is truncated at some fixed expansion order K . Here we discuss the case with explicit symmetry breaking, here represented by the term $c\sigma$. In its absence one usually employs different sets of equations for regimes with broken/unbroken symmetry. The requirement of expanding about the physical minimum, $\partial_\sigma U_k(\sigma^2, \sigma)|_{\sigma=\sqrt{\phi_k^2}} = 0$, yields $a_{1,k} = \frac{c}{2\sqrt{\phi_k^2}}$ which in turn implies $\dot{a}_{1,k} \equiv \partial_t a_{1,k} = -\frac{c}{4} \dot{\phi}_k^2 (\phi_k^2)^{-\frac{3}{2}}$. This allows to eliminate $a_{1,k}$ from the set of flow equations in favor of $\dot{\phi}_k^2$. If we now expand the flow equation for the effective potential as

$$\partial_t U_k(\phi^2) = \sum_{n=0}^{\infty} \frac{\dot{U}_k^{(n)}}{n!} (\phi^2 - \phi_k^2)^n, \quad (2.23)$$

where $\dot{U}_k^{(n)} = \frac{\partial^n \partial_t U_k}{(\partial \phi^2)^n} |_{\phi^2=\phi_k^2}$ and insert the Ansatz from Eq. (2.22) we are just left with a system of ordinary differential equations

$$\begin{aligned} \dot{a}_{0,k} &= \dot{U}_k^{(0)} + a_{1,k} \dot{\phi}_k^2 \\ \dot{a}_{1,k} &= \dot{U}_k^{(1)} + a_{2,k} \dot{\phi}_k^2 = -\frac{c}{4} \dot{\phi}_k^2 (\phi_k^2)^{-\frac{3}{2}} \\ &\dots \\ \dot{a}_{K-1,k} &= \dot{U}_k^{(K-1)} + a_{K,k} \dot{\phi}_k^2 \\ \dot{a}_{K,k} &= \dot{U}_k^{(K)}. \end{aligned} \quad (2.24)$$

Considering just the pure number of equations to be solved the method seems to be numerically rather cheap. However, in particular for higher orders in the expansion one should keep in mind that the right hand sides of the flow equations for the expansion coefficients gets increasingly complicated as they involve multiple derivatives of original right hand side of the flow equation.

The method can be generalized to effective potentials parametrized by several invariants in an obvious manner. Furthermore, the Taylor method is perfectly suited to determine critical exponents. One can either determine the critical exponents β and δ from the order parameter, which typically appears as an explicit variable in the system of differential equations, or even more directly calculate the correlation length critical exponent ν via the largest eigenvalues of the stability matrix expanded about a RG fixed point along with the anomalous dimension η as solution of the corresponding flow equation.

Grid methods

The methods subsumed as grid methods in this section share the property that they use an expansion of the effective potential on a discrete set of grid points ϕ_i in field space. This allows in principle to capture the full field-dependence of the effective potential and thus includes arbitrarily high interaction terms in the fields whereas the previously discussed Taylor method remains by construction restricted to a finite expansion order. As the grid method takes into account the full field-dependence of the effective potential and not just information about a local minimum, it is particularly suited to describe also first order phase transitions. From the technical point of view the effective potential has to be reconstructed from a finite set of values in order to evaluate derivatives of the effective potential appearing on the right side of the flow equation. The essential difference between the methods presented in this section lies only in the level of sophistication used to obtain these derivatives. The applicability for effective potentials parametrized by several invariants of all methods discussed in detail below remains restricted to cases where the field variables remain restricted to a domain which is diffeomorphic to a hypercube. The general case can then be mapped to the hypercubical/rectangular case by an appropriate diffeomorphism as employed in [61]. In all cases the flow of the effective potential is calculated without explicit symmetry breaking, which is only added to the full potential after the integration of the flow.

1. The original grid method [62, 63] entails setting up a Taylor expansion to fixed expansion order M at each grid point. As described in the previous section one then obtains flow equations for the coefficients $a_{i,n}$ at grid point i to expansion order n . The two highest order coefficients at each grid point $a_{i,M-1}$ and $a_{i,M}$ are then expressed via lower order coefficients by imposing continuity conditions for the effective potential and lower derivatives at midpoints between the grid points. The original grid method is a rather sophisticated method with high numerical stability as higher order derivatives are eliminated algebraically rather than numerically but is unfortunately numerically expensive compared to the methods described below due to the large number of variables. Furthermore, there is no obvious generalization to higher dimensional problems where one has to specify a sufficient number of independent continuity conditions to eliminate the higher order derivatives.
2. As the flow equation for the effective potential is just a partial differential equation the most straightforward solution method is via a finite difference approach. Here one keeps the RG time variable continuous and just estimates the required derivatives of the effective potential at the grid points via finite differences. One should keep a consistent discretization order which involves employing function values of more grid points for the evaluation of the derivatives near the edges of the grid. This leads to a system of coupled differential equations just for the value of the effective potential at each grid point which can be solved using standard methods. The method is numerically considerably cheaper than the

2. The Functional Renormalization Group

original grid method, straightforward to implement and generalizes in an obvious way to higher-dimensional problems.

3. The third class of solution methods is similar to the finite difference techniques except that the values of the scale-dependent effective potential are interpolated and derivatives are extracted from the interpolating function. The choice mainly used in this thesis are cubic splines with fixed first derivatives at the boundaries which are estimated via finite differences. From a given one-dimensional spline interpolation one directly obtains first and second derivatives, which is perfectly suited for the evaluation of the flow equation for the effective potential. Again, there is a straightforward extension to higher dimensional problems since interpolations of higher dimensional functions can simply be realized as consecutive one-dimensional spline interpolations.

But more generally, one can use any set of complete basis functions to expand the effective potential. A particularly convenient choice, which has been applied to related problems [64, 65], is the expansion in terms of Chebychev polynomials, which then turns the partial differential equation into a system of ordinary differential equations for the expansion coefficients.

2.2 Flow of 2-Point Functions: Pole Masses and Spectral Functions

There is a tremendous qualitative improvement in functional approaches for the description of the phase structure of strongly interacting theories in increasingly refined truncation schemes not only in QCD but also in statistical mechanics, solid-state physics or atomic physics which now reach the accuracy of state-of-the-art lattice simulations. But along with these improvements in the static case also dynamical quantities, such as transport coefficients or spectral functions in near-equilibrium situations or even questions of non-equilibrium, come more and more into the focus of interest and should be a logical next step in the development.

One particular example is the calculation of transport coefficients such as the shear viscosity, which can be extracted from retarded real-time 2-point correlation functions of components of the stress-energy tensor using Kubo formulas. Here we will be mainly concerned with the seemingly simpler question of the definition of particle masses, which is particularly relevant for effective model calculations where typically some of the model parameters are fixed to reproduce particle masses. It turns out to be a crucial but non-trivial task to find a mass definition which is consistent with the underlying truncation for the effective action. We will discuss this in more detail for the particular case of 2-color QCD in Section 3.4.3, where we will argue that a consistent mass definition should be based on the location of the poles in the corresponding propagators or equivalently on the zeros in the corresponding 2-point functions, which in turn requires the calculation of 2-point functions within the FRG framework. This problem can be subdivided into finding an appropriate truncation

2.2. Flow of 2-Point Functions: Pole Masses and Spectral Functions

for the (momentum-dependent) 2-point function and the analytical continuation from Euclidean to Minkowskian external momentum.

Flow of the 2-point function

The flow equation for the 2-point functions can be obtained from the flow equation for the effective action by repeated functional differentiation as represented diagrammatically for an $O(N)$ example in Fig. 2.2. But note that these flow equations depend in turn on up to 4-point functions giving rise to an infinite tower of coupled equations. One thus requires an appropriate truncation scheme to render this system of equations finite. One approach is to employ the BMW approximation [56, 57]. The idea is to expand 3- and 4-point functions in their external momenta which is justified by the fact that their dependence on external momenta is weaker than the dependence on loop momenta due to the insertion of the regulator function. Finally, at zero external momentum 3- and 4-point vertices can be related to derivatives of 2-point functions. At first order in the BMW approximation one obtains the vertices

$$\Gamma_{ijl}^{(3)}(q, -q) = \frac{\partial \Gamma_{ij}^{(2)}(q; \phi)}{\partial \phi_l}, \quad \Gamma_{ijlm}^{(4)}(q, -q, 0) = \frac{\partial^2 \Gamma_{ij}^{(2)}(q; \phi)}{\partial \phi_l \partial \phi_m}, \quad (2.25)$$

which, inserted into the flow equations for the 2-point functions, leads to a closed system of coupled partial differential equations for the pion and the sigma meson 2-point functions $\Gamma_{k,\pi\pi}^{(2)}$ and $\Gamma_{k,\sigma\sigma}^{(2)}$ in the particular case of an $O(N)$ model, which can then be solved numerically for fixed Euclidean external momentum.

We take an even simpler approach and completely neglect the momentum dependence of the 3- and 4-point vertices and replace them by the constant vertices obtained from the LPA Ansatz for the effective action. The external momentum then only enters the calculation via the propagators. This way of truncating the flow equation for the 2-point function is completely analogous to the calculation of the flow of the wave function renormalization where one, however, only aims at computing the prefactor of the kinetic term via an appropriate projection at the end of the calculation. This implies for example for momentum-independent vertices that only the first diagram in Fig. 2.2 has to be considered as the second diagram remains independent of the external momentum and hence does not give a contribution to the flow of the wavefunction renormalization. Note that for zero external momentum all information about n -point functions is encoded in the effective potential. For example the 2-point functions can simply be calculated from derivatives of the effective potential. It is a particular advantage of our truncation using LPA vertices that this limit is satisfied by construction whereas it has to be put in by hand in the BMW approximation.

Analytical continuation

Given a suitable truncation which allows the calculation of 2-point functions for a given Euclidean external momentum, the question is how to obtain real-time 2-point

2. The Functional Renormalization Group

functions from it. In principle one can imagine two approaches here. Firstly, one can solve the flow equation for Euclidean external momentum and then try to extract the real time correlation function from the Euclidean correlation function using for example the maximum entropy method or Padé approximants [66, 67, 68]. This is possible but a numerically rather involved procedure in particular with regard to an extension to the finite temperature case where the two point function is only given at a discrete set of Matsubara frequencies. Alternatively, one can analytically continue already at the level of the flow equation and integrate down the analytically continued flow equation which gives then direct access to the real-time 2-point function at $k = 0$ but in a sense less control over the analytical continuation.

A similar approach was employed in [69] where the author proposed a more refined truncation in Minkowski space which includes the effects of the backcoupling of the propagator into the effective potential and the wavefunction renormalization which is not taken into account here. The actual solution required, however, an Ansatz for the form of the propagator near its poles which is not required here.

2.2.1. $O(N)$ model: Flow of the 2-point function

As an illustrative example we will concentrate in the following on the flow of 2-point functions in an $O(N)$ model, where our starting point is the Ansatz for the effective action in the local potential approximation

$$\Gamma_k = \int_x \frac{1}{2} \partial_\mu \phi_i \partial^\mu \phi_i + U_k(\phi^2) - c\sigma, \quad (2.26)$$

where the only scale dependence comes from the effective potential U_k . We will not restrict ourselves to a particular regulator at this point, but employ a sharp 3-momentum regulator for the numerical evaluation later in this section. The flow equation for the effective potential is obtained straightforwardly by evaluating the flow equation Eq. (2.17) for a constant field configuration $\phi_i = \phi \delta_{i1}$ and is given by

$$\partial_t U_k = \frac{1}{2} I_\sigma^{(1)} + (N-1) \frac{1}{2} I_\pi^{(1)}, \quad (2.27)$$

where $I_X^{(n)} \equiv I_k^{(n)}(\phi^2)_{m_X}$ for $m_\pi^2 = 2U'_k$, $m_\sigma^2 = 2U'_k + 4U''_k \phi^2$, $G_m(q) = (q_0^2 + \vec{q}^2 + R_k(q) + m^2)^{-1}$ and

$$I_k^{(n)}(\phi^2)_m \equiv \sum_q \partial_t R_k(q) G_m(q)^n. \quad (2.28)$$

The flow equation for the 2-point function is represented graphically in Fig. 2.2. The required 3- and 4-point vertices are obtained from the Ansatz (2.26) and are for

2.2. Flow of 2-Point Functions: Pole Masses and Spectral Functions

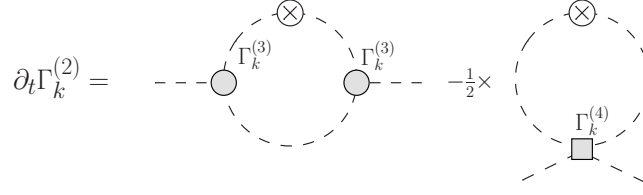


Figure 2.2.: Flow of the 2-point function in an $O(N)$ model. Crossed circles represent regulator insertions $\partial_t R_k$.

the constant field configuration from above just given by

$$\begin{aligned}\Gamma_{ijk}^{(3)} &= 4U_k'' \phi (\delta_{ij} \delta_{k1} + \delta_{jk} \delta_{i1} + \delta_{ik} \delta_{j1}) + 8U_k''' \delta_{i1} \delta_{j1} \delta_{k1} \\ \Gamma_{ijkl}^{(4)} &= 4U_k'' (\delta_{ij} \delta_{kl} + \delta_{il} \delta_{jk} + \delta_{jl} \delta_{ik}) + 8U_k''' \phi^2 (\delta_{ij} \delta_{k1} \delta_{l1} + \delta_{jk} \delta_{i1} \delta_{l1} + \delta_{kl} \delta_{i1} \delta_{j1}) \\ &\quad + \delta_{jl} \delta_{i1} \delta_{k1} + \delta_{il} \delta_{j1} \delta_{k1} + \delta_{ik} \delta_{j1} \delta_{l1}) + 16U_k'''' \phi^4 \delta_{i1} \delta_{j1} \delta_{k1} \delta_{l1}.\end{aligned}\quad (2.29)$$

The corresponding flow equations for the pion and sigma 2-point functions then read

$$\partial_t \Gamma_{k,\pi\pi}^{(2)} = (4U_k'' \phi)^2 (J_{\sigma\pi} + J_{\pi\sigma}) - \frac{1}{2} 4U_k'' (N+1) I_\pi^{(2)} - \frac{1}{2} (4U_k'' + 8U_k''' \phi^2) I_\sigma^{(2)}, \quad (2.30)$$

$$\begin{aligned}\partial_k \Gamma_{k,\sigma\sigma}^{(2)} &= (12U_k'' \phi + 8U_k''' \phi^3)^2 J_{\sigma\sigma} + (N-1) (4U_k'' \phi)^2 J_{\pi\pi} \\ &\quad - \frac{1}{2} (12U_k'' + 48U_k''' \phi^2 + 16U_k'''' \phi^4) I_\sigma^{(2)} - \frac{1}{2} (N-1) (4U_k'' + 8U_k''' \phi^2) I_\pi^{(2)},\end{aligned}\quad (2.31)$$

where we defined $J_{XY} \equiv J_k(p, \phi^2)_{m_X, m_Y}$ with

$$J_k(p, \phi^2)_{m_X, m_Y} \equiv \int_q \partial_t R_k(q) G_{m_X}(p+q) G_{m_Y}(q)^2. \quad (2.32)$$

The explicit expressions for the functions $I_k^{(n)}$ and J_k evaluated for the sharp 3-momentum regulator and purely timelike external momentum $p_\mu = (p_0, \vec{0})$ are listed in Appendix B. In this case the flow equations take a particularly simple form as the spatial momentum integration can be performed trivially. In the following all functions in Eq. (2.30) and Eq. (2.31) are understood as evaluated for purely timelike external momentum $p_0 = -i\omega$.

As we will demonstrate in Section 3.4.3, the extension of the method to include fermionic degrees is straightforward. The same is true at least from the conceptual point of view for the inclusion of finite chemical potential. The case of a finite spatial external momentum should also be studied as it is for example relevant for the investigation of the spectrum of soft modes near the critical endpoint [70] or the computation of transport coefficients.

Consistency with the effective potential

For vanishing external momentum the 2-point functions can be obtained from derivatives of the effective potential. The equality of the two expressions for the 2-point function calculated either directly or via the effective potential is a nontrivial statement, which does of course not hold for general unrelated truncations for the effective action and the 2-point function [71]. In such a case one can still choose to fix this by introducing an additional constant contribution to the flow equation of the 2-point function such that the consistency condition is satisfied as it is commonly done in the BMW approximation [56, 57]. However, we will see that the truncation for the 2-point function using LPA vertices is already consistent with the effective potential.

For simplicity let us discuss the pion case first. It is a nontrivial statement which holds at any temperature that the flow equation for the pion 2-point function obeys the consistency condition

$$\partial_t \Gamma_{k,\pi\pi}^{(2)}(0) = \frac{\partial^2}{\partial \pi_i \partial \pi_i} \partial_t U_k = 2 \frac{\partial}{\partial \phi^2} \partial_t U_k. \quad (2.33)$$

If we choose $\Gamma_{\Lambda,\pi\pi}^{(2)}(\omega_0^2) = -\omega_0^2 + 2U'(\phi^2)$ at the UV scale Λ , we can define a pion *pole mass* $m_{\pi,\text{pole}}$ via

$$\Gamma_{k=0,\pi\pi}^{(2)}(m_{\pi,\text{pole}}^2) = 0. \quad (2.34)$$

The consistency condition (2.33) now implies that if we calculate $\Gamma_{k=0,\pi\pi}^{(2)}$ by integrating the flow equation (2.30) for zero external momentum, $\omega_0 = 0$ and $\vec{\omega} = \vec{0}$, the pole mass defined via Eq. (2.34) reduces to the familiar *screening mass* obtained from the curvature of the effective potential.² Furthermore, this property guarantees the existence of a dynamical Nambu-Goldstone pion in the chiral limit.

Next we turn to the sigma meson 2-point function. At zero temperature one verifies that the consistency condition

$$\partial_t \Gamma_{k,\sigma\sigma}^{(2)}(0) = \frac{\partial^2}{\partial \sigma \partial \sigma} \partial_t U_k = 2 \frac{\partial}{\partial \phi^2} \partial_t U_k + 4\phi^2 \frac{\partial^2}{(\partial \phi^2)^2} \partial_t U_k \quad (2.35)$$

holds. Here the initial conditions in the UV are chosen as $\Gamma_{\Lambda,\sigma\sigma}^{(0,2)}(\omega_0^2) = -\omega_0^2 + 2U'(\phi^2) + 4\phi^2 U''(\phi^2)$. At finite temperature however, a subtlety arises. It is a well-known fact in finite temperature field theory [72, 73] that the self-energy may become non-analytic at zero external momentum. This means in particular that the limits $p_0 \rightarrow 0$ and $\vec{p} \rightarrow \vec{0}$ no longer commute as in the case of zero temperature. For the 2-point functions the two limits have a physical interpretation [72] in terms of screening masses ($p_0 = 0, \vec{p} \rightarrow 0$) and plasma oscillation frequencies ($\vec{p} = \vec{0}, p_0 \rightarrow 0$). The standard procedure for computing 2-point correlation functions involves exploiting the

²Here and in the following we refer to screening masses as the square-root of the eigenvalues of the Hessian of the effective potential at its minimum or equivalently as the square-root of the inverse propagator in the spacelike static limit ($p_0 = 0, \vec{p} \rightarrow 0$), cf. the discussion below, and hence the inverse of a corresponding susceptibility. This definition does in general not coincide with the usual definition of the screening mass via the pole of the static propagator.

2.2. Flow of 2-Point Functions: Pole Masses and Spectral Functions

periodicity of the thermal distribution functions in the external momentum $p_0 = 2\pi nT$ ($n \in \mathbb{Z}$) after evaluating the Matsubara sums but before the analytic continuation which completely eliminates the external momentum from the distribution functions. Note that the analytical continuation of a Green's function given on a discrete set of Matsubara modes is only unique after imposing additional analyticity conditions [74] and this standard procedure is consistent with these requirements. In this approach the screening mass can then be obtained from the spacelike static limit, i.e. by setting $p_0 = 0$ and taking the limit $\vec{p} \rightarrow \vec{0}$. There is, however, a different procedure which allows one to extract the corresponding contributions without considering finite spatial external momenta. Therefore one keeps the general expression without exploiting the periodicity in p_0 and analytically continues in p_0 , which obviously corresponds to a different analytical continuation where the external momentum appears still as argument of the occupation numbers but which is not consistent with the analyticity requirements from [74]. However, one can obtain the screening mass from this procedure by carefully taking the limit $p_0 \rightarrow 0$ at the end of the calculation, see also the appendix of [1] and Section 3.3.3. In this sense the consistency condition (2.35) holds even at finite temperature.

Numerical solution

We propose two possible solution methods for the flow equations (2.27) and (2.30) or (2.31). Firstly, one can use a Taylor expansion for both the effective potential and the 2-point function of the form

$$\begin{aligned}
 U_k &= \sum_{n=0}^K a_{n,k} (\phi^2 - \phi_k^2)^n \\
 \Gamma_{k,AA}^{(2)}(\omega) &= \sum_{n=0}^L b_{n,k}^{AA}(\omega) (\phi^2 - \phi_k^2)^n,
 \end{aligned}
 \tag{2.36}$$

where $A \in \{\sigma, \pi\}$. By choosing $L = K - 1$ one easily verifies by comparing the flow equations for the Taylor coefficients $a_{n,k}$ and $b_{n,k}^{AA}$, obtained as described in Section 2.1.4, that the consistency condition (2.33) for the pion 2-point function remains exactly satisfied even in the numerical implementation. As the flow equation for the sigma meson 2-point function involves up to fourth derivatives of the effective potential we chose $K = 4$ and $L = 3$ in the numerical implementation. The Taylor implementation has the advantage of allowing to integrate down to $k = 0$ which is required to accurately describe the spectral function around the 2-pion threshold but it is on the other hand not well-suited for the finite temperature case due to the complicated structure of the flow equation from which up to third derivatives are required to obtain flow equations for the Taylor coefficients.

Alternatively one employs a grid solution of the effective potential to extract the derivatives of the effective potential at its IR minimum value required for the evaluation of the flow equation of the 2-point functions. This is on the one hand computationally

2. The Functional Renormalization Group

less expensive and thus better suited for the finite temperature case but on the other hand numerically less stable compared to the implementation via a Taylor expansion. But both methods lead to consistent results for the zero temperature case and thus allow the computation of pion pole masses from a given UV potential or spectral functions as described in the next section.

2.2.2. $O(4)$ model: pole masses and spectral functions

Spectral functions have been calculated within FRG approaches in particular in several non-relativistic models within different truncation schemes including the BMW approximation, vertex expansions or derivative expansions [75, 76, 77]. However, in all cases the analytic continuation from Euclidean 2-point functions was carried out using Padé approximants.

The spectral function is defined via the imaginary part of the retarded propagator or more explicitly as

$$\rho_A(\omega) = -\frac{\text{Im}\Gamma_A^{(2)R}}{\left(\text{Im}\Gamma_A^{(2)R}\right)^2 + \left(\text{Re}\Gamma_A^{(2)R}\right)^2} \quad (2.37)$$

for $A = \pi, \sigma$, which is understood as evaluated in the limit of an infinitesimally small imaginary external momentum. Note that the continuation prescription $p_0 \rightarrow -i(\omega + i\epsilon)$ corresponds precisely to the definition of the retarded 2-point function required for the calculation of the spectral function disregarding the fact that the imaginary part is kept small but finite in the numerical evaluation. In the following we present results for the zero temperature case [78] in the $O(4)$ model.

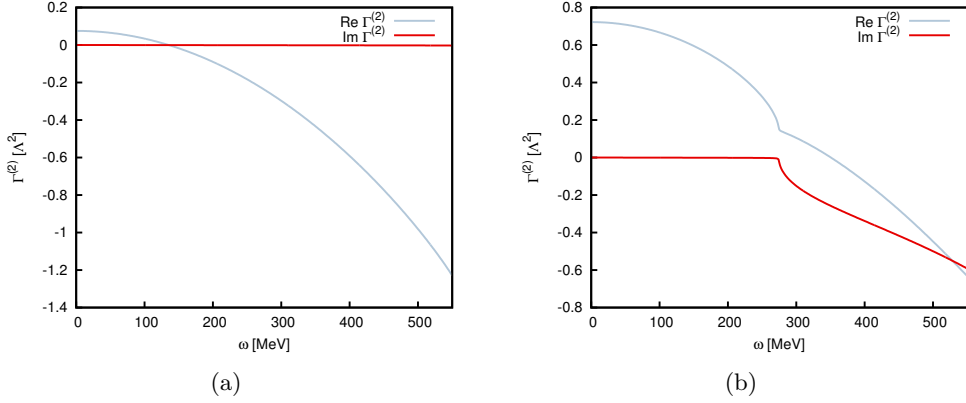


Figure 2.3.: Real and imaginary part of $\Gamma^{(2)}$ for pion (a) and sigma meson (b) in dependence of external momentum ω [78].

Fig. 2.3 shows the corresponding real and imaginary parts of the pion and sigma meson 2-point function. In the pion case the imaginary part remains negligible and the real part behaves as demonstrated in earlier investigations [1, 2]. The zero of the real part corresponds to the pion pole mass and is found at 135.1 MeV compared to a

2.2. Flow of 2-Point Functions: Pole Masses and Spectral Functions

screening mass of 137.2 MeV extracted from the curvature of the effective potential. The mismatch of screening mass and the onset of charged pion condensation in the corresponding quark-meson model coupled to isospin chemical potential was already observed in [79] and is discussed in detail in [2]. Here we just point out the non-equivalence of different mass definitions and postpone the detailed discussion to the sections 3.3.3 and 3.4.3, where we discuss the difference between pole and screening masses in the context of a model with both bosonic and fermionic degrees of freedom. In the sigma case shown in Fig. 2.3(b) the imaginary part of the 2-point function remains negligible only up to the 2-pion threshold, which also shows up as a kink in the real part, and tends to negative values afterwards.

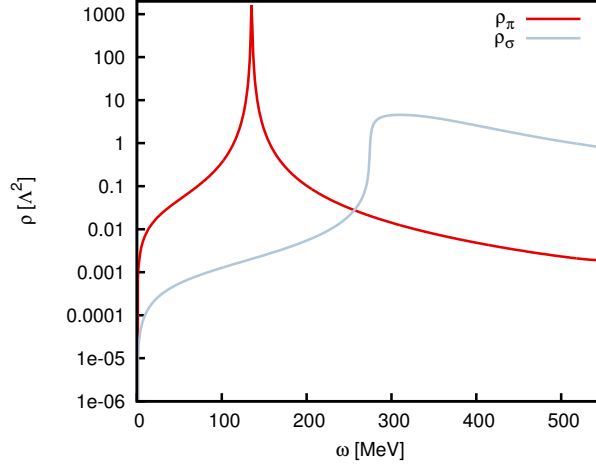


Figure 2.4.: $O(4)$ model pion and sigma meson spectral functions ρ_π and ρ_σ [78].

The sigma and pion spectral functions as calculated from Eq. (2.37) are shown in Fig. 2.4. The pion spectral function shows a sharp peak at 135 MeV to be identified with the pion mass. The sigma spectral function shows the 2-pion threshold as a characteristic rise in the spectrum and a broad maximum above this value at about 312 MeV. Considering the case of an imaginary part $\text{Im } \Gamma^{(2)}$ which is independent of real external momentum and only a momentum dependent real part $\text{Re } \Gamma^{(2)}$, it is obvious from the definition (2.37) that the maximum of the spectral function occurs at the zero of the real part with the broadness of the maximum determined by the imaginary part. This can be observed in the case of the pion 2-point function where the peak in the spectral function and zero of the 2-point function coincide as the imaginary part stays practically constant. The coincidence between the sigma mass defined via the maximum of the spectral function and the zero of the corresponding 2-point function is of course no longer valid considering a momentum dependent imaginary part, although the zero of the real part, here found at 350.6 MeV, might still provide an estimate for the sigma mass. This should be contrasted with the significantly larger estimate via the sigma meson screening mass from the curvature of the effective potential which yields a value of 425 MeV for the employed parameter set.

Part I.

**Effective Models for QCD-like
Theories**

3

Quark-Meson-Diquark Models for QCD-like Theories

3.1 Introduction

In this chapter we discuss chiral effective models for different QCD-like theories in particular for two representatives, 2-color QCD with quarks in the fundamental representation and any-color QCD with quarks in the adjoint representation, of the two classes of QCD-like theories for which the Dirac operator possesses an additional antiunitary symmetry. Their common feature is the absence of a fermion sign problem, in contrast to the usual case of 3-color QCD, which allows lattice simulations even at finite chemical potentials and thus ultimately a direct comparison of functional methods calculations to lattice simulations. Such studies can then help to gain an understanding of the reliability of these methods for the application to the 3-color phase diagram.

In this chapter we will outline the construction of chiral effective models for QCD-like theories in the form of *quark-meson-diquark (QMD) models*. A special emphasis in the chapter will lie on the case of 2-color QCD, which is interesting for another reason, because it is particularly suited to study the impact of baryonic degrees of freedom on its phase diagram, which are, however, bosons here rather than fermions. In particular, the lightest baryonic degrees of freedom are a pair of bosonic diquarks which are degenerate with the pions at zero chemical potential due to an enhanced flavor symmetry. Finally, as last piece of motivation, QCD-like theories in general turn out to be closely related to effective Lagrangians employed for the description of ultracold atomic gases. This manifests itself on the level of the Lagrangians but also in their phase diagrams where they share a BEC-BCS crossover as common feature.

In the remainder of this section we will explore these points in more detail and close with a short introduction to the *Silver Blaze property*.

3. Quark-Meson-Diquark Models for QCD-like Theories

QCD sign problem

The QCD sign problem designates the fact that the fermion determinant at finite chemical potential is a complex number, which prevents its interpretation as a probability measure required for a direct application of Monte Carlo methods. In order to calculate the QCD partition function, written symbolically for vanishing sources as

$$Z_{\text{QCD}} = \int \mathcal{D}A \mathcal{D}\psi \mathcal{D}\bar{\psi} e^{-S[A, \psi, \bar{\psi}]}, \quad (3.1)$$

we can formally integrate out the quarks as the action is bilinear in the quark fields, which yields a factor $\det(\not{D} + m - \mu\gamma^0)$ for each quark flavor. As discussed in the introduction, for three colors and quarks in the fundamental representation this determinant is complex at finite chemical potential. This represents a major technical complication for lattice approaches to finite density QCD, which triggered different proposals on how to circumvent the sign problem at least for small chemical potentials [21, 23, 80]. However, the particularly interesting regions of the phase diagram where $\mu/T \gg 1$ remain inaccessible in these approaches. This is why we will pursue a different approach here and study QCD-like theories with real fermion determinants, which obviously differ from QCD in this respect but are hopefully still similar enough to gain insights into finite density QCD. In such theories the real fermion determinant is enforced via additional symmetries of the corresponding Dirac operators which can be classified by the Dyson index β^1 from random matrix theory [81, 83].

Before we turn to these particular cases, let us briefly discuss the generic case without antiunitary symmetry ($\beta = 2$). Here the (Euclidean) \not{D} operator obeys the relation $\gamma^5 \not{D} \gamma^5 = \not{D}^\dagger$ known as γ^5 hermiticity, which implies

$$\gamma^5 (\not{D} + m - \mu\gamma^0) \gamma^5 = (\not{D} + m + \mu^* \gamma^0)^\dagger \quad (3.2)$$

and leads to

$$\det(\not{D} + m - \mu\gamma^0) = \det(\not{D} + m + \mu^* \gamma^0)^* \quad (3.3)$$

after taking determinants. This enforces a real fermion determinant for zero ($\mu = 0$) or imaginary chemical potential ($\mu = i\mu_i$). For an even number of degenerate flavors we get a nonnegative factor which can be interpreted as a probability measure again for which standard Monte Carlo techniques are applicable. In fact the same is true for QCD with pure isospin chemical potential μ_I and an even number of degenerate quark flavors, where Eq. (3.3) implies

$$\det(\not{D} + m - \mu_I \gamma^0) \cdot \det(\not{D} + m + \mu_I \gamma^0) = |\det(\not{D} + m - \mu_I \gamma^0)|^2. \quad (3.4)$$

The case of pure isospin chemical potential is the prototypical example for a theory with Dyson index $\beta = 2$ and a nonnegative fermion determinant.

¹For an antiunitary operator T which commutes with the Dirac operator one defines $\beta = 1$ if $T^2 = 1$, $\beta = 4$ if $T^2 = -1$ and in the absence of such a symmetry $\beta = 2$ [81] corresponding to fermions transforming in pseudoreal, real or complex representations of the gauge group, see Chapter 21 in [82] and footnote 2.

Let us now turn to QCD-like theories for which the Dirac operator possesses an additional antiunitary symmetry. Following [84] we consider the general situation of a Dirac operator \mathcal{D} which obeys a relation of the form

$$[T, \mathcal{D}] \equiv [UK, \mathcal{D}] = 0, \quad (3.5)$$

where K denotes the complex conjugation operator, U is a unitary operator and correspondingly $T = UK$ is an antiunitary operator. For an eigenvector ψ of the Dirac operator with eigenvalue λ , i.e. $\mathcal{D}\psi = \lambda\psi$, this relation implies $\mathcal{D}\tilde{\psi} = \lambda^*\tilde{\psi}$ for $\tilde{\psi} = UK\psi$. As all eigenvalues appear in conjugate pairs, the determinant $\det M$ is obviously real. This does of course not imply that the determinant is positive since for negative real eigenvalues λ the corresponding eigenvectors ψ and $\tilde{\psi}$ could be linearly dependent. But interestingly, if in addition $T^2 = (UK)^2 = -1$, we have $\langle\psi|\tilde{\psi}\rangle = \langle\psi|UK\psi\rangle = \langle KUK\psi|K\psi\rangle = \langle(UK)^2\psi|UK\psi\rangle = -\langle\psi|\tilde{\psi}\rangle = 0$, which thus implies that the determinant $\det \mathcal{D}$ remains nonnegative.

The latter scenario, $T^2 = -1$, corresponds to a Dyson index $\beta = 4$ with QCD with quarks in the adjoint representation or QCD with gauge group G_2 as most prominent examples. Hence, the fermion determinant in these theories is nonnegative for any number of quark flavors. The prototypical example of an antiunitary symmetry with $T^2 = 1$, corresponding to a Dyson index $\beta = 1$, is 2-color QCD with quarks in the fundamental representation. In this and the following chapter we will consider examples for all three cases, namely 2-color QCD with quarks in the fundamental representation ($\beta = 1$), QCD with quarks in the adjoint representation ($\beta = 4$) and finally 3-color QCD with isospin chemical potential ($\beta = 2$) in Chapter 4.

Baryonic degrees of freedom

As discussed in the introduction, baryonic degrees of freedom are expected to have a large impact on the QCD phase diagram, in particular at small temperatures and intermediate chemical potentials. This argument is strongly supported by large- N_c considerations where the baryon density becomes an actual order parameter. Whereas for 2-color QCD, as for 3-color QCD, this is only the case at zero temperature, there is another order parameter in 2-color QCD, the diquark condensate, whose onset coincides with that of the baryon number density at zero temperature. Although at finite temperature the baryon density is no longer strictly zero outside the diquark condensation phase, it rises abruptly at the onset of diquark condensation. This is why we can picture the diquark condensate as analogue of the strict order parameter baryon number in the large- N_c limit or also in the limit where the number of flavors N_f grows along with N_c , i.e. for N_f/N_c held fixed. Thus if one is willing to accept the relevance of large- N_c arguments for the QCD phase diagram, it might not be too far-fetched to believe the same for $N_c = N_f = 2$ always keeping in mind the crucial differences between $N_c = 2$ and $N_c = 3$.

The inclusion of the lightest baryonic degrees of freedom in effective model approaches to QCD-like theories such as 2-color QCD or adjoint QCD is extremely simplified

3. Quark-Meson-Diquark Models for QCD-like Theories

by enlarged flavor symmetries. The diquarks as lightest baryonic degrees of freedom appear as (pseudo-) Goldstone bosons of chiral symmetry breaking and transform in the same multiplet as the pions and the sigma meson. This technical simplification will allow us to demonstrate the effects of baryonic degrees of freedom on the phase diagram of 2-color QCD very transparently.

Finally, it is interesting to study theories with both bosonic and fermionic baryons such as 2-color QCD with adjoint quarks or QCD with gauge group G_2 . Based on these examples one can study projection mechanisms in order to remove the bosonic baryons from the theory which might ultimately lead to a QCD-like theory with just fermionic baryons which is amenable to lattice simulations at finite chemical potentials.

Ultracold atomic gases

A different class of strongly coupled systems which received a lot of attention in recent years are ultracold atomic gases, see [85, 86] for general introductions and [87, 88] for introductions from the FRG perspective. The particularly appealing feature of these systems compared to QCD is the fact that characteristics of the theory can be tuned directly in the lab, which allows in this way the experimental access to different regimes of a strongly coupled theory. Most importantly, the s-wave scattering length a_s and correspondingly the interaction strength can be tuned experimentally using an external magnetic field via a Feshbach resonance, allowing to invert the standard scale hierarchy [87]. One distinguishes three regimes characterized by the value of the scattering length: The BEC regime with $a_s > 0$ where fermions form tightly bound bosonic molecules, the strongly-interacting unitary limit corresponding to a diverging scattering length $a_s \rightarrow \infty$, and the BCS regime for $a_s < 0$ where fermions pair in the form of spatially delocalized Cooper pairs. There is a smooth crossover between these different regimes known as *BEC-BCS crossover*. A successful non-perturbative treatment of the whole range of the BEC-BCS crossover in cold atomic gases within the FRG framework [89] is based on the effective Lagrangian

$$\mathcal{L} = \psi^\dagger (\partial_\tau - \Delta - \mu) \psi + \varphi^* \left(\partial_\tau - \frac{1}{2}\Delta + \nu - 2\mu \right) \varphi - \frac{h_\varphi}{2} \left(\varphi^* \psi^T \epsilon \psi - \varphi \psi^\dagger \epsilon \psi^* \right) \quad (3.6)$$

for a complex two-component spinor ψ and a complex scalar field φ , where Δ is the Laplacian and ϵ the totally antisymmetric symbol. The interpretation of the complex scalar φ depends on the regime under consideration and can either be describing bound states of fermions in the BEC regime or Cooper-pair excitations in the BCS regime.

Although ultra-cold atomic gases are non-relativistic systems with a completely different physical background, there are close connections to relativistic QCD-like theories as will be discussed in the course of this and the following chapter. These manifest themselves on the one hand already on the level of the effective Lagrangians, where for example the effective 2-color quark-meson diquark Lagrangian can be identified as relativistic analogue of the Lagrangian given in Eq. (3.6), but on the other hand directly in the corresponding phase diagrams, where both share a BEC-BCS

crossover as common feature. Strengthening analogies between the two systems is certainly a worthwhile task, which will turn out beneficial for both sides in the future.

Silver Blaze property

We close this motivational overview with a brief introduction to the Silver Blaze property [90, 91] as a principle which puts strong constraints on the phase diagrams of relativistic theories at zero temperature and which will play an important role in our subsequent analysis. In a theory with a relativistic chemical potential coupled to degrees of freedom with a mass gap, the thermodynamic partition function and correspondingly all thermodynamic observables have to stay independent of the chemical potential as long as the latter stays smaller than the mass gap. In order to excite any states at zero temperature, the relativistic chemical potential needs to be increased beyond the mass gap in the correlations it couples to. In 2-color QCD the zero-temperature transition is continuous and the Silver Blaze property thus requires the zero-temperature thermodynamic partition function to stay independent of the (quark-)chemical potential as long as it remains smaller than half of the pion mass, which coincides with one half of the lightest baryon mass m_B in this particular case. To phrase it more generally, the Silver Blaze property will hold up to a baryon chemical potential of m_B or up to a possible first order transition below this value, where the difference is typically interpreted as binding energy per nucleon, see also the discussion of the liquid gas transition in Section 3.4.2. It is important to stress that the Silver Blaze property is a generic feature of the relativistic chemical potential and not a particular property of fermionic or QCD-like theories but has for example also been studied in purely bosonic theories [92, 93, 94].

3.2 Symmetries and Model Construction

The key to the understanding of both 2-color and adjoint QCD is their enlarged flavor symmetry, which is in turn a direct consequence of the (pseudo-)reality of the representations under consideration. In particular the $SU(2)$ fundamental representation is pseudoreal whereas the $SU(N_c)$ adjoint representation is a real representation.² In the following we will treat the cases of 2-color fundamental and adjoint fermions in parallel to illustrate similarities and differences. This section represents partly a summary of the pioneering works [95, 96], but is nevertheless required as the symmetries and their breaking patterns constitute the basis of the understanding of QCD-like theories.

²In general a representation and its complex conjugate representation form distinct representations, in which case the representation is called complex. However, if the two turn out to be isomorphic we talk of real or pseudoreal representations. In this case the representation matrix \mathcal{M} of a given representation and the representation matrix $\bar{\mathcal{M}}$ of the corresponding complex conjugate representation are related via a similarity transformation, $\mathcal{M} = S\bar{\mathcal{M}}S^{-1}$, with a matrix S , which can be either symmetric, the defining property of a real representation, or antisymmetric, corresponding to a pseudoreal representation.

3.2.1. Extended flavor symmetries and symmetry breaking patterns

Antiunitary symmetry of the Dirac operator

For the fundamental representation, the isomorphism relating the fundamental representation and its complex conjugate is given by $S = \sigma_2$, where obviously $S^T = -S$ as the $SU(2)$ fundamental representation is pseudoreal. Therefore, charge conjugation of the gauge fields in QC₂D can be undone by the constant $SU(2)$ gauge transformation $S = \sigma_2$. From now on we will use T^a for the color generators, for the fundamental representation just given by $T^a = \sigma^a/2$, with

$$T^{aT} = T^{a*} = -ST^aS^{-1}, \quad (3.7)$$

and reserve σ_i (τ_i) for the Pauli matrices in spinor (flavor) space. Denoting the charge conjugation matrix in spinor space by C , the 2-color Dirac operator $\mathcal{D}(\mu) = \not{D} + m - \mu\gamma^0$ at finite chemical potential μ obeys [95, 96]

$$D(\mu)SC\gamma^5 = SC\gamma^5D^*(\mu), \quad (3.8)$$

which is precisely an antiunitary symmetry of the form of Eq. (3.5) with $U = SC\gamma^5$. As $C^2 = -1$ and $KS = -SK$, we have $T^2 = (UK)^2 = -S^2C^2 = 1$ corresponding to a Dyson index $\beta = 1$ in the classification scheme of the previous section, which implies that the fermion determinant is nonnegative for an even number of degenerate quark flavors.

On the contrary, the $SU(N_c)$ adjoint representation is a real $N_c^2 - 1$ dimensional representation with color generators defined via the $SU(N_c)$ structure constants f_{abc} as $(T^a)_{bc} = f_{abc}$, which in turn implies

$$T^{aT} = T^{a*} = -T^a = -ST^aS^{-1}, \quad (3.9)$$

where $S = 1$ and hence $S^T = S$ for a real representation. Again the Dirac operator obeys the relation from Eq. (3.8), this time with $S = 1$, however. As $C^2 = -1$ but now $KS = SK$, we have $T^2 = (UK)^2 = S^2C^2 = -1$ corresponding to a Dyson index $\beta = 4$.³

³Interestingly, for the staggered Dirac operator the roles of fundamental and adjoint representation get exchanged compared to the corresponding Dyson indices of the continuum theory, i.e. the Dyson index for fundamental staggered fermions is $\beta = 4$ and for adjoint staggered fermions $\beta = 1$ [84]. The reason is that the Dirac structure gets absorbed in staggered fermion operator which manifests itself in a missing charge conjugation matrix in the corresponding relations for the Dirac operator which, as $C^2 = -1$, exchanges the cases $\beta = 1$ and $\beta = 4$. The same twist is observed on the level of the chiral symmetry breaking patterns where one finds $U(2N_f) \rightarrow SO(2N_f)$ for fundamental and $U(2N_f) \rightarrow Sp(N_f)$ for adjoint quarks [84], cf. the continuum discussion below. From the viewpoint of chiral symmetry simulations of adjoint staggered fermions are thus closer to continuum fundamental fermions than staggered fundamental fermions. On the other hand, adjoint fermions do not break the global Z_{N_c} center symmetry and chiral symmetry restoration and deconfinement are no longer related [97].

Kinetic term

We start the discussion of the symmetries by considering the standard kinetic part of the Euclidean QC₂D Lagrangian, which reads in the chiral basis⁴

$$\mathcal{L}_{\text{kin}} = \bar{\psi} \not{D} \psi = \psi_L^\dagger i \sigma_\mu D_\mu \psi_L - \psi_R^\dagger i \sigma_\mu^\dagger D_\mu \psi_R, \quad (3.10)$$

where the covariant derivative is given by $D_\mu = \partial_\mu + iA_\mu$ with gauge coupling absorbed in the gauge fields $A_\mu = A_\mu^a T^a$. So far the extended flavor symmetry of the kinetic term is not manifest. This can be easily achieved by changing variables to $\tilde{\psi}_R = \sigma_2 S \psi_R^*$ and $\tilde{\psi}_R^* = \sigma_2 S \psi_R$, thereby reexpressing Eq. (3.10) as

$$\mathcal{L}_{\text{kin}} = \Psi^\dagger i \sigma^\mu D_\mu \Psi \quad (3.11)$$

in terms of the $4N_c N_f$ -dimensional spinors $\Psi = \begin{pmatrix} \psi_L \\ \tilde{\psi}_R \end{pmatrix}$ and $\Psi^\dagger = (\psi_L^\dagger, \tilde{\psi}_R^\dagger)$. With the Lagrangian in a block diagonal form, the $SU(2N_f)$ symmetry in the space of combined flavor and transformed chiral components, often referred to as *Pauli-Gürsey symmetry*, is now manifest. For both 2-color fundamental and adjoint quarks, the extended flavor symmetry is $SU(2N_f)$ instead of $U(2N_f)$ as the axial $U(1)_A$ symmetry is broken anomalously. The only difference between the cases of fundamental and adjoint matter is at this point the insertion of the appropriate matrix S in the definition of the spinor variable Ψ .

Dirac-mass term

We proceed by considering an (explicit or spontaneously generated) Dirac-mass term, which for fundamental quarks can be written as

$$m \bar{\psi} \psi = -\frac{m}{2} \left(\Psi^T \sigma_2 S \Sigma_0 \Psi - \Psi^{*T} \sigma_2 S \Sigma_0 \Psi^* \right), \quad (3.12)$$

where the symplectic matrix

$$\Sigma_0 = \begin{pmatrix} 0 & \mathbb{1}_{N_f} \\ -\mathbb{1}_{N_f} & 0 \end{pmatrix} \quad (\beta = 1) \quad (3.13)$$

acts in the $2N_f$ -dimensional extended flavor space. An explicit (dynamical) Dirac mass therefore explicitly (spontaneously) breaks the original $SU(2N_f)$ down to the compact symplectic group $Sp(N_f)$ ⁵ as subgroup of $SU(2N_f)$ transformation leaving Eq. (3.12) invariant. This gives rise to a Goldstone manifold $SU(2N_f)/Sp(N_f)$, which

⁴As usual in Euclidean signature, $\psi_{R/L}$ and $\psi_{R/L}^*$ are considered as independent Grassmann variables with $\psi_{R/L}^\dagger \equiv \psi_{R/L}^{*T}$. Furthermore, see Appendix A for our conventions on Euclidean Gamma matrices.

⁵The symplectic group $Sp(N)$ is defined as the intersection of the unitary group $U(2N)$ and the symplectic group $Sp(2N, \mathbb{C})$, which is the invariance group of Σ_0 as bilinear form on complex $2N$ -component vectors. $Sp(N)$ is a real Lie group of dimension $N(2N + 1)$.

3. Quark-Meson-Diquark Models for QCD-like Theories

is $N_f(2N_f - 1) - 1$ dimensional corresponding to $N_f(2N_f - 1) - 1$ (pseudo-) Goldstone bosons.

The Dirac mass term for adjoint quarks can also be written in the form of Eq. (3.12) but in this case with $S = 1$ and a symmetric matrix

$$\Sigma_0 = \begin{pmatrix} 0 & \mathbb{1}_{N_f} \\ \mathbb{1}_{N_f} & 0 \end{pmatrix} \quad (\beta = 4). \quad (3.14)$$

The subgroup of $SU(2N_f)$ which leaves the corresponding Eq. (3.12) invariant turns out to be locally $SO(2N_f)$ as can be most conveniently observed on the level of Lie algebra generators, see Appendix C.1. In this case the Goldstone manifold is obviously given by $SU(2N_f)/SO(2N_f)$, which is $N_f(2N_f + 1) - 1$ dimensional.

These results are in perfect agreement with the Pauli principle. Considering only the flavor structure, the quark bilinears correspond to the tensor product $2N_f \otimes 2N_f$, which decomposes as

$$2N_f \otimes 2N_f = (N_f(2N_f - 1))_{\text{a}} \oplus (N_f(2N_f + 1))_{\text{s}} \quad (3.15)$$

into a $N_f(2N_f - 1)$ dimensional antisymmetric and a $N_f(2N_f + 1)$ dimensional symmetric representation. For $\beta = 1$ the condensate is antisymmetric in spin and color space, so the Pauli principle requires the $N_f(2N_f - 1)$ dimensional antisymmetric flavor structure. As the condensation occurs in one particular direction and this leaves us with $N_f(2N_f - 1) - 1$ Goldstone bosons again. In the case of $\beta = 4$ the spin structure is antisymmetric, but unlike before the color structure is now a (symmetric) singlet as product of two adjoint representations, which requires the symmetric $N_f(2N_f + 1)$ dimensional flavor structure and the counting leads to $N_f(2N_f + 1) - 1$ Goldstone bosons again.

Chemical potential

Let us also consider the case of a nonvanishing chemical potential $\mu \neq 0$ but $m = 0$. We can write the chemical potential term as

$$\mu \bar{\psi} \gamma^0 \psi = \mu \Psi^\dagger B_0 \Psi, \quad (3.16)$$

where

$$B_0 = \begin{pmatrix} \mathbb{1}_{N_f} & 0 \\ 0 & -\mathbb{1}_{N_f} \end{pmatrix} \quad (\beta = 1, 4). \quad (3.17)$$

Thus for $m = 0$ a finite chemical potential $\mu \neq 0$ breaks $SU(2N_f)$ explicitly down to $SU(N_f)_L \times SU(N_f)_R \times U(1)_B$. For 2-color fundamental (adjoint) matter where both $m \neq 0$ and $\mu \neq 0$ the remaining symmetry group is given by the common subgroup of $Sp(N_f)$ ($SO(2N_f)$) and $SU(N_f)_L \times SU(N_f)_R \times U(1)_B$, which is just given by $SU(N_f)_V \times U(1)_B$. Whether this looks as an approximate symmetry more like $Sp(N_f)$ ($SO(2N_f)$) corresponding to the limiting case $\mu \rightarrow 0$ or like $SU(N_f) \times SU(N_f) \times U(1)$ as the limiting case $m \rightarrow 0$ depends just on the relative sizes of m and μ . This

is illustrated transparently by the vacuum alignment in chiral perturbation theory [95, 96]: For $\mu_B = 2\mu < m_\pi$ the vacuum alignment stays $\langle \bar{q}q \rangle$ -like with an approximate $Sp(N_f)$ ($SO(2N_f)$) symmetry. For $\mu_B = 2\mu > m_\pi$ diquark condensation sets in and the vacuum alignment starts to rotate from $\langle \bar{q}q \rangle$ -like to $\langle qq \rangle$ -like with increasing chemical potential μ . In the following paragraph we discuss the residual symmetry in the diquark condensation phase and in particular the symmetry for asymptotically large chemical potentials.

Diquark condensation

As we will see in the next section after rewriting the interaction terms in original variables again, a nonvanishing diquark condensate is for 2-color fundamental quarks (restricting ourselves for simplicity to the most relevant case of an even number of flavors) represented by

$$\Sigma_d = \begin{pmatrix} iJ_{N_f} & 0 \\ 0 & iJ_{N_f} \end{pmatrix} \quad (\beta = 1), \quad \text{where} \quad J_{2N} = \begin{pmatrix} 0 & \mathbb{1}_N \\ -\mathbb{1}_N & 0 \end{pmatrix}, \quad (3.18)$$

whereas for adjoint quarks

$$\Sigma_d = \begin{pmatrix} i\mathbb{1}_{N_f} & 0 \\ 0 & i\mathbb{1}_{N_f} \end{pmatrix} \quad (\beta = 4). \quad (3.19)$$

The residual symmetry in the diquark condensation phase is defined via the condition

$$U^T \Sigma_d U = \Sigma_d, \quad \text{where} \quad U \in SU_V(N_f) \times U(1)_B, \quad (3.20)$$

which translates into $T^T \Sigma_d + \Sigma_d T = 0$ on the level of the corresponding Lie algebra generators T . Now the residual symmetry is easily identified as $Sp(N_f/2)_V$ or $SO(N_f)_V$ for $\beta = 1$ and $\beta = 4$ respectively. Obviously the $U(1)_B$ baryon number symmetry is always broken in the diquark condensation phase, but in general the Goldstone manifold is higher dimensional. For $\beta = 1$ it is the $N_f(N_f - 1)/2$ dimensional coset $(SU_V(N_f) \times U(1)_B)/Sp(N_f/2)$ and for $\beta = 4$ the $N_f(N_f + 1)/2$ dimensional coset $(SU_V(N_f) \times U(1)_B)/SO(N_f)$.

In the chiral limit diquark condensation sets in at $\mu = 0$. As only the relative size of m and μ will turn out to be relevant, the residual symmetry in the diquark condensation phase in the chiral limit coincides with the asymptotic symmetry in the limit $\mu \rightarrow \infty$ even in a theory with finite m . Starting from $SU(N_f)_L \times SU(N_f)_R \times U(1)_B$ instead of $SU(N_f)_V \times U(1)_B$ the asymptotic symmetry in the diquark condensation phase is found to be $Sp(N_f/2)_L \times Sp(N_f/2)_R$ or $SO(N_f)_L \times SO(N_f)_R$ for $\beta = 1$ and $\beta = 4$ respectively.

Patterns of symmetry breaking for 2-color fundamental and adjoint matter

The different symmetry breaking patterns are summarized in Fig. 3.1 and Fig. 3.2. We conclude this section with a few remarks on the case of two flavors, $N_f = 2$,

3. Quark-Meson-Diquark Models for QCD-like Theories

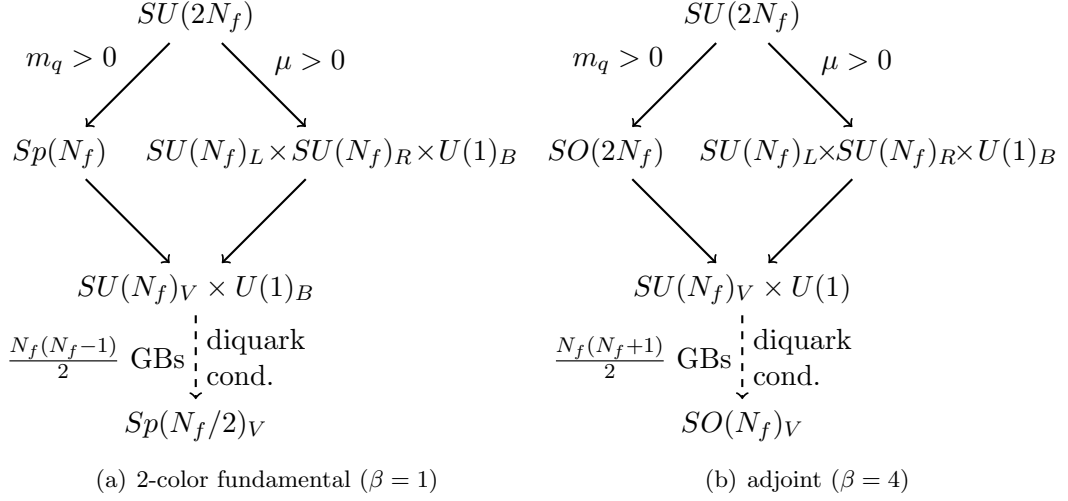


Figure 3.1.: Patterns of symmetry breaking in 2-color QCD with fundamental quarks ($\beta = 1$) and any-color QCD with adjoint quarks ($\beta = 4$).

which is most relevant for the following sections. Here one can make use of the Lie algebra isomorphisms $su(4) \simeq so(6)$, $sp(2) \simeq so(4)$ and $sp(1) \simeq su(2)$ to rephrase the symmetry breaking patterns, at least locally, in terms of more familiar symmetry groups.

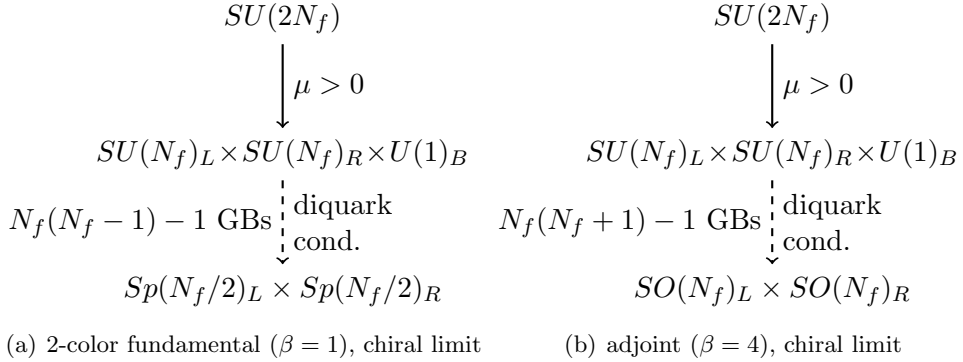


Figure 3.2.: Patterns of symmetry breaking in 2-color QCD with fundamental quarks ($\beta = 1$) and any-color QCD with adjoint quarks ($\beta = 4$) in the chiral limit.

For $\beta = 1$ and $N_f = 2$ we can formulate the breaking of $SU(4)$ down to $Sp(2)$ by an explicit or dynamically generated Dirac mass term isomorphically as breaking of $SO(6) \rightarrow SO(5)$ which is just the symmetry breaking pattern familiar from vector models. The coset is in this case given by $SO(6)/SO(5) \simeq S^5$, the unit sphere in five dimensions, and a spontaneously generated Dirac mass thus breaks five of the $SO(6)$ generators, leading to five (pseudo-) Goldstone bosons, which will be identified with the

usual three pions and a pair of bosonic scalar diquarks. The baryon number symmetry $U(1)_B$ induces rotations in the diquark space and gets spontaneously broken inside the diquark condensation phase, where the diquark condensate singles out a particular direction and correspondingly one massless Goldstone bosons appears. The residual $SO(3)$ symmetry inside the diquark condensation phase allows rotations in the pion subspace and gets enhanced to an asymptotic $SO(4)$ symmetry thus restoring chiral symmetry in the limit $\mu \rightarrow \infty$ again. This complete restoration of chiral symmetry is a particular feature of the two flavor case, where only one Goldstone boson appears in the diquark condensation phase.

For $\beta = 4$ and $N_f = 2$ a Dirac mass breaks the enlarged flavor symmetry according to $SO(6) \rightarrow SO(4)$ and correspondingly nine (pseudo-) Goldstone bosons appear, which we will identify as three pions and an isotriplet of bosonic scalar diquark pairs. In this case a diquark condensate not only breaks the baryon number $U(1)_B$, but rather $SO(3) \times U(1)_B \rightarrow SO(2)$ and three Goldstone bosons appear. The residual $SO(2)_V$ symmetry in the diquark condensation phase can be pictured as rotations around a fixed axis in the diquark and pion space and gets enhanced to an asymptotic $SO(2)_L \times SO(2)_R$ symmetry in the limit $\mu \rightarrow \infty$ again. The case of $\beta = 4$ and a single quark flavor, $N_f = 1$, is even simpler. Here the enlarged flavor symmetry $SU(2)$ is broken by either a finite Dirac mass term or a finite chemical potential down to $U(1)_B$, which corresponds locally to the simple vector model breaking pattern $SO(3) \rightarrow SO(2)$. Correspondingly only two (pseudo-) Goldstone bosons appear which will be identified as a scalar diquark pair below. The $U(1)_B$ symmetry is broken spontaneously in the diquark condensation phase and only one Goldstone mode appears.

3.2.2. Quark-meson-diquark model Lagrangians

Now we turn to the construction of chiral effective models which incorporate the symmetry breaking patterns discussed in the previous section. Here the starting point is the flavor structure of the standard chiral condensate and the quark mass term which is of the form $\Psi^T \Sigma_0 \Psi$. The chiral condensate is just one component of a flavor multiplet which transforms in the $N_f(2N_f - 1)$ dimensional antisymmetric or the $N_f(2N_f + 1)$ dimensional symmetric representation from Eq. (3.15) for $\beta = 1$ or $\beta = 4$ respectively. The other components of the same multiplet are obtained from transformations

$$\Psi \rightarrow U\Psi, \quad U = \exp(i\theta^a X^a) \in \begin{cases} SU(2N_f)/Sp(N_f) & (\beta = 1) \\ SU(2N_f)/SO(2N_f) & (\beta = 4) \end{cases}, \quad (3.21)$$

where we can restrict ourselves to coset elements as other group elements by definition leave Σ_0 invariant. Then, $\Psi^T \Sigma_0 \Psi \rightarrow \Psi^T \Sigma \Psi$, where, from Cartan's immersion theorem, the whole coset is obtained in this way via $\Sigma \equiv U^T \Sigma_0 U$. In order to proceed one now requires explicit parametrizations of the coset generators, which are listed in Appendix C.1 for the most relevant cases ($\beta = 1, N_f = 2$ and $\beta = 4, N_f = 1, 2$).

Considering infinitesimal transformations of $U = \exp(i\theta X^a/2)$, one finds $\Psi^T \Sigma_0 \Psi \rightarrow$

3. Quark-Meson-Diquark Models for QCD-like Theories

$\Psi^T \Sigma_0 \Psi + \theta \Psi^T \Sigma_a \Psi$, defining $\Sigma_a = i \Sigma_0 X^a$ for the respective coset generators X_a . We can now define an effective quark-meson diquark model Lagrangian as a linear sigma model with Yukawa couplings of meson and diquark fields to quarks of the schematic form $\Psi^T \phi_i \Sigma_i \Psi$.

2-color fundamental matter

This procedure is especially transparent for the 2-color 2-flavor case, $\beta = 1$ and $N_f = 2$, where the coset elements Σ connected to Σ_0 can be parametrized by six-dimensional unit vectors \vec{n} as $\Sigma = \vec{n} \vec{\Sigma}$, with $\Sigma_i^\dagger \Sigma_j + \Sigma_j^\dagger \Sigma_i = 2\delta_{ij}$ and $\vec{\Sigma} = (\Sigma_0, i \Sigma_0 X^a)$ for a basis of $SU(4)/Sp(2)$ coset generators X^a , $a = 1 \dots 5$, see Appendices C.1 and C.2. Now one can verify explicitly using the infinitesimal transformation properties of Σ that the vector $\Psi^T \vec{\Sigma} \Psi$ transforms as a (complex) six-dimensional vector under $SO(6)$, see Appendix C.3.

A locally $SU(2)_c$ invariant linear sigma model Lagrangian can therefore be defined by coupling the real $SO(6)$ vector of quark bilinears ($\Psi^T \vec{\Sigma} \Psi + \text{h.c.}$) to the vector $\vec{\phi} = (\sigma, \vec{\pi}, \text{Re } \Delta, \text{Im } \Delta)^T$ formed by the scalar σ meson, the pseudoscalar pions $\vec{\pi}$ and the scalar diquark-antidiquark pair Δ, Δ^* . This yields the Lagrangian

$$\mathcal{L}_{\sigma,2cf} = \Psi^\dagger i \sigma^\mu D_\mu \Psi - \frac{h}{2} (\Psi^T \sigma_2 S \vec{\Sigma} \Psi - \Psi^{*T} \sigma_2 S \vec{\Sigma} \Psi^*) \vec{\phi} + \frac{1}{2} (\partial_\mu \vec{\phi})^2 + V(\vec{\phi}), \quad (3.22)$$

where $V(\vec{\phi})$ is the meson and diquark potential which will be specified later. The Lagrangian rewritten in original variables is now given by

$$\begin{aligned} \mathcal{L}_{\sigma,2cf} = & \bar{\psi} (\not{D} + h(\sigma + i\gamma^5 \vec{\pi} \vec{\tau})) \psi + \frac{h}{2} \left(\Delta^* (\psi^T C \gamma^5 \tau_2 i S \psi) + \Delta (\psi^\dagger C \gamma^5 \tau_2 i S \psi^*) \right) \\ & + \frac{1}{2} (\partial_\mu \sigma)^2 + \frac{1}{2} (\partial_\mu \vec{\pi})^2 + \frac{1}{2} \partial_\mu \Delta \partial^\mu \Delta^* + V(\vec{\phi}), \end{aligned} \quad (3.23)$$

with $C = \gamma^2 \gamma^0$ and a Yukawa coupling h . It remains to introduce a nonvanishing chemical potential into the Lagrangian. This is done by means of standard methods [73] and is only reproduced here for completeness. Therefore note that the Lagrangian (3.23) is invariant under $U(1)$ phase rotations associated to quark number conservation

$$\psi \rightarrow e^{i\alpha} \psi, \quad \psi^\dagger \rightarrow e^{-i\alpha} \psi^\dagger, \quad \Delta \rightarrow e^{2i\alpha} \Delta, \quad \Delta^* \rightarrow e^{-2i\alpha} \Delta^*, \quad (3.24)$$

provided that the potential V only depends on diquarks via the invariant $d^2 \equiv \Delta^* \Delta$. The associated conserved Noether current is given by

$$J^\mu = -\bar{\psi} \gamma^\mu \psi + \Delta^* \partial^\mu \Delta - \Delta \partial^\mu \Delta^*. \quad (3.25)$$

On the level of the Hamiltonian \mathcal{H} chemical potential is introduced by replacing $\mathcal{H} \rightarrow \mathcal{H} - \mu J^0$, where μ appears as Lagrange multiplier enforcing quark number conservation. The corresponding Lagrangian then defines the quark-meson-diquark

3.2. Symmetries and Model Construction

(QMD) model for 2-color fundamental matter

$$\begin{aligned} \mathcal{L}_{\text{QMD,2cf}} = & \bar{\psi} (\not{D} + h(\sigma + i\gamma^5 \vec{\pi} \vec{\tau}) - \mu\gamma^0) \psi + \frac{h}{2} \left(\Delta^* (\psi^T C \gamma^5 \tau_2 i S \psi) + \Delta (\psi^\dagger C \gamma^5 \tau_2 i S \psi^*) \right) \\ & + \frac{1}{2} (\partial_\mu \sigma)^2 + \frac{1}{2} (\partial_\mu \vec{\pi})^2 + \frac{1}{2} ((\partial_\mu - 2\mu \delta_\mu^0) \Delta) (\partial_\mu + 2\mu \delta_\mu^0) \Delta^* + V(\vec{\phi}) . \end{aligned} \quad (3.26)$$

Neglecting the mesonic sector for a moment, the Lagrangian (3.26) can be seen as relativistic analogue of the non-relativistic Lagrangian from Eq. (3.6) as both describe spinors coupled to a pair of complex scalars via a Yukawa interaction in presence of a finite chemical potential.

Considering now a potential which is $O(6)$ symmetric up to an explicit symmetry breaking term $c\sigma$,

$$V(\vec{\phi}) = \frac{\lambda}{4} (\vec{\phi}^2 - v^2)^2 - c\sigma , \quad (3.27)$$

for which one obtains the corresponding $O(6)$ linear sigma model. In the limit $\lambda \rightarrow \infty$, the bosonic part of the Lagrangian from Eq. (3.26) is equivalent to the leading-order χ PT Lagrangian from [96]. This can be checked explicitly by starting from the χ PT Lagrangian [96] and using the explicit parametrization of coset elements in terms of a 6-dimensional unit vector, see Appendix C.2, and identifying $v = f_\pi = 2F$ and $c = f_\pi m_\pi^2 = 2Fm_\pi^2$. Interestingly, the coefficient of the leading term in μ of the χ PT Lagrangian, $\mu^2 \text{tr}(\Sigma B^T \Sigma^\dagger B)$ with $B = UB_0U^\dagger$, which was fixed from gauging the flavor $SU(4)$ in χ PT [95], here simply follows from $-2\mu^2 |\Delta|^2$ as remnant of the covariant derivative in the kinetic term of the diquark field Δ . Although the meson and diquark potential $V(\vec{\phi})$, up to the explicit breaking by $-c\sigma$, is in general only required to be $SO(4) \times SO(2)$ symmetric at finite chemical potential, the argument from above shows that it has to remain $SO(6)$ invariant at leading order, $\mathcal{O}(\mu^2)$, in chemical potential.

In the following it will be more convenient to rewrite the Lagrangian in terms of Nambu-Gorkov-like spinors $\Psi = \begin{pmatrix} \psi_r \\ \tau_2 \psi_g^C \end{pmatrix}$, where ψ_r (ψ_g) denote the red (green) color components of ψ and $\psi^C \equiv C\bar{\psi}^T$ as in [98]. This yields the compact representation

$$\mathcal{L}_{\text{QMD,2cf}} = \bar{\Psi} S_0^{-1} \Psi + \frac{1}{2} (\partial_\mu \sigma)^2 + \frac{1}{2} (\partial_\mu \vec{\pi})^2 + \frac{1}{2} ((\partial_\mu - 2\mu \delta_\mu^0) \Delta) (\partial_\mu + 2\mu \delta_\mu^0) \Delta^* + V(\vec{\phi}) , \quad (3.28)$$

where

$$S_0^{-1} = \begin{pmatrix} \not{\partial} + h(\sigma + i\gamma^5 \vec{\pi} \vec{\tau}) - \gamma^0 \mu & g\gamma^5 \Delta \\ -g\gamma^5 \Delta^* & \not{\partial} + h(\sigma - i\gamma^5 \vec{\pi} \vec{\tau}) + \gamma^0 \mu \end{pmatrix} . \quad (3.29)$$

3. Quark-Meson-Diquark Models for QCD-like Theories

Adjoint matter

For adjoint matter, focusing here in particular on the case of two quark flavors, we define an effective Lagrangian via

$$\mathcal{L}_{\sigma,adj} = \Psi^\dagger i\sigma^\mu D_\mu \Psi - \frac{g}{2}(\Psi^T \sigma_2 S \Sigma_i \phi_i \Psi - \Psi^{*T} \sigma_2 S \Sigma_i \phi_i \Psi^*) + \frac{1}{2}(\partial_\mu \phi_i)^2 + V(\phi_i), \quad (3.30)$$

where $i = 0, \dots, 9$ and $S = 1$. As before we set $\Sigma_i = i\Sigma_0 X_i$ ($i = 1 \dots 9$) and insert the coset generators X_i from Appendix C.1. Using the parametrization⁶ $(\phi_i) = (\sigma, \pi_1, -\pi_2, \pi_3, -\text{Im}\Delta_2, \text{Re}\Delta_3, -\text{Re}\Delta_1, \text{Re}\Delta_2, \text{Im}\Delta_3, -\text{Im}\Delta_1)$ the Lagrangian can be rewritten in original variables as

$$\begin{aligned} \mathcal{L}_{\sigma,adj(N_f=2)} = & \bar{\psi} (\not{D} + h(\sigma + i\gamma^5 \vec{\pi} \vec{\tau})) \psi + \frac{h}{2} \left(\vec{\Delta}^* (\psi^T C \gamma^5 \tau_2 \vec{\tau} \psi) + \vec{\Delta} (\psi^\dagger C \gamma^5 \tau_2 \vec{\tau} \psi^*) \right) \\ & + \frac{1}{2}(\partial_\mu \sigma)^2 + \frac{1}{2}(\partial_\mu \vec{\pi})^2 + \frac{1}{2} \partial_\mu \vec{\Delta} \partial^\mu \vec{\Delta}^* + V(\phi_i), \end{aligned} \quad (3.31)$$

where we identify sigma meson (σ), three pions ($\vec{\pi}$) and an isotriplet pair of diquarks ($\vec{\Delta}, \vec{\Delta}^*$). The coupling to the chemical potential for quarks and diquarks is realized analogously to the 2-color case. Again it proves useful to rewrite the Lagrangian in terms of Nambu-Gorkov spinors $\Psi = \frac{1}{\sqrt{2}} \begin{pmatrix} \psi \\ \tau_2 \psi^C \end{pmatrix}$, which yields

$$\begin{aligned} \mathcal{L}_{\text{QMD},adj(N_f=2)} = & \bar{\Psi} S_0^{-1} \Psi + \frac{1}{2}(\partial_\mu \sigma)^2 + \frac{1}{2}(\partial_\mu \vec{\pi})^2 + V(\vec{\phi}) \\ & + \frac{1}{2}((\partial_\mu - 2\mu\delta_\mu^0) \vec{\Delta})(\partial_\mu + 2\mu\delta_\mu^0) \vec{\Delta}^*, \end{aligned} \quad (3.32)$$

where

$$S_0^{-1} = \begin{pmatrix} \not{\partial} + h(\sigma + i\gamma^5 \vec{\pi} \vec{\tau}) - \gamma^0 \mu & ih\gamma^5 \vec{\tau} \vec{\Delta} \\ ih\gamma^5 \vec{\tau} \vec{\Delta}^* & \not{\partial} + h(\sigma - i\gamma^5 \vec{\pi} \vec{\tau}) + \gamma^0 \mu \end{pmatrix}. \quad (3.33)$$

Even simpler is the situation in the case of a single adjoint quark flavor, $N_f = 1$, which can be derived analogously from Eq. (3.30) using the coset generators X_1 and X_2 from Appendix C.1. Here the analogue of the Lagrangian (3.31) reads

$$\begin{aligned} \mathcal{L}_{\sigma,adj(N_f=1)} = & \bar{\psi} (\not{D} + h\sigma) \psi + \frac{h}{2} \left(\Delta^* (\psi^T C \gamma^5 \psi) + \Delta (\psi^\dagger C \gamma^5 \psi^*) \right) \\ & + \frac{1}{2}(\partial_\mu \sigma)^2 + \frac{1}{2} \partial_\mu \Delta \partial^\mu \Delta^* + V(\phi_i), \end{aligned} \quad (3.34)$$

defining the vector $(\phi_i) = (\sigma, -\text{Im} \Delta, \text{Re} \Delta)^T$. Again note the correspondence of the 1-flavor Lagrangian to the 2-flavor 2-color Lagrangian and thus also to the non-relativistic effective Lagrangian for the description of the BEC-BCS crossover in ultracold atomic gases.

⁶Despite the suggestive notation, (ϕ_i) should be understood just as a 10-tupel as it, unlike in the case of $\beta = 1$ and $N_f = 2$ from above, does not transform as a vector, see Appendix C.3.

The effective Lagrangians for adjoint QCD so far contain just quarks, mesonic and bosonic baryonic degrees of freedom. But unlike for 2-color fundamental matter, where one only has bosonic baryons,⁷ adjoint matter can form color neutral bound states out of any number quarks, i.e. in particular also fermionic baryons like in 3-color QCD, since the tensor product of any number of adjoint representations contains a color singlet.⁸ The effective Lagrangian following from (3.30) with no explicit fermionic baryonic degrees of freedom is certainly the leading contribution as the pseudo-Goldstone bosons taken into account here are expected to be lighter than the additional fermionic baryons. These can, however, be included as explicit degrees of freedom into the effective Lagrangian by constructing interaction terms consistent with the underlying symmetries.

Including gauge dynamics

Gauge field dynamics and confinement effects can be modeled in QC₂D by including a constant Polyakov-loop variable as a background field as in the NJL model [98], and analogous to what is commonly done in Polyakov-loop-extended quark-meson [99] or Polyakov-loop-extended NJL models [30] for three-color QCD. To this end one introduces a constant temporal background gauge field $A_\mu = A_0\delta_{\mu 0}$, which is furthermore assumed to be in the Cartan subalgebra as in Polyakov gauge, i.e. for $SU(2)_c$ simply given by $A_0 = T^3 a_0$.⁹ As outlined in the first chapter, this leads to the Polyakov loop variable

$$\Phi \equiv \frac{1}{2} \text{Tr}_c e^{i\beta A_0} = \cos\left(\frac{\beta a_0}{2}\right) \quad (3.35)$$

to model a thermal expectation value of the color-traced Polyakov loop at an inverse temperature $\beta = 1/T$, as an order parameter for the deconfinement transition at vanishing chemical potential. The covariant derivative $D_\mu = \partial_\mu - i\delta_{\mu 0}A_0$ leads to an additional contribution to the QMD model Lagrangian of the form $-i\bar{\psi}\gamma^0 T^3 a_0 \psi$ which can be rewritten as $-i\bar{\Psi}\gamma^0 \frac{a_0}{2}\Psi$ in terms of the spinor field Ψ defined after Eq. (3.28). Finally, we arrive at the Polyakov-loop-extended quark-meson-diquark (PQMD) model Lagrangian, again written in the basis of Nambu-Gorkov-like spinors,

$$\mathcal{L}_{\text{PQMD},2\text{cf}} = \mathcal{L}_{\text{QMD},2\text{cf}} - i\bar{\Psi} \begin{pmatrix} \gamma^0 \frac{a_0}{2} & 0 \\ 0 & \gamma^0 \frac{a_0}{2} \end{pmatrix} \Psi + \mathcal{U}_{\text{Pol}}, \quad (3.36)$$

with \mathcal{L}_{QMD} defined in Eq. (3.28) and \mathcal{U}_{Pol} being the Polyakov-loop potential. Such potentials are commonly fitted to reproduce lattice pure gauge thermodynamics [100]

⁷This property is common to all $SU(N_c)$ QCD-like theories with fundamental fermions and an even number of colors. The reason is that the tensor product of an odd number of fundamental representations is constructed from an odd number of boxes in the language of Young tableaux, whereas a color singlet in $SU(N_c)$ requires an even number of boxes for even N_c .

⁸This can easily be seen from the decomposition $(N_c^2 - 1) \otimes (N_c^2 - 1) \rightarrow 1 \oplus (N_c^2 - 1) \oplus \dots$. The fact that the decomposition on the right hand side contains a singlet and at least one adjoint representation ensures iteratively that the same is true for a tensor product of an arbitrary number of adjoint representations.

⁹Note again that $T^3 = \frac{1}{2}\sigma_3$ and the gauge coupling has been absorbed into the gauge fields.

3. Quark-Meson-Diquark Models for QCD-like Theories

but can in particular also be computed using functional methods [64, 101]. It is, however, important to remark that although we refer to them as Polyakov-loop potentials the effective gauge potential input should in principle use an effective potential as a function of a_0 rather than Φ . There is so far no lattice data available but such a_0 -dependent effective potentials are typical outcomes of functional methods calculations from Yang-Mills flows. Unlike in the 3-color case the Polyakov-loop potential is a function of a single real variable Φ or a_0 respectively here, even at finite chemical potential.

For the case of adjoint matter a coupling to a background gauge field can be achieved by similar means but for N_c colors the potential in Polyakov gauge will then depend on all $N_c - 1$ components of A_0 in the Cartan subalgebra, i.e. $A_0 = \sum_{c=1}^{N_c-1} A_0^c T_{\text{adj}}^c$, where T_{adj}^c are the generators of the Cartan subalgebra in the adjoint representation. On the level of the Lagrangian this then amounts to defining

$$\mathcal{L}_{\text{PQMD,adj}} = \mathcal{L}_{\text{QMD,adj}} - i\bar{\Psi} \begin{pmatrix} \gamma^0 A_0 & 0 \\ 0 & \gamma^0 A_0^T \end{pmatrix} \Psi + \mathcal{U}_{\text{Pol}}, \quad (3.37)$$

where Ψ denotes the Nambu-Gorkov spinor defined after Eq. (3.31).

3.3 QMD Model for QC₂D: Mean-Field Analysis

We include a mean-field¹⁰ analysis of the QMD model at this point not only for later comparison to the RG results, but also just because of its simplicity as it will allow us to make analytical statements about the pole mass spectrum and in particular its relation to the Silver Blaze property such as the coincidence of the onset of diquark condensation and the pion mass. This property verified explicitly in the mean-field framework is expected to hold also in more refined truncations provided the pole mass is calculated consistently and is in this sense a statement very similar to the existence of a massless Goldstone mode in the chiral limit [103].

3.3.1. Mean-Field Grand Potential

The first task consists in computing the grand potential in mean-field approximation from which condensates and all thermodynamic quantities can be obtained. This involves replacing mesonic and diquark fields by their constant expectation values $\sigma \equiv \langle \sigma \rangle$, $\Delta \equiv \langle \Delta \rangle$, $\Delta^* \equiv \langle \Delta^* \rangle$ and $\vec{\pi} \equiv \langle \vec{\pi} \rangle = \vec{0}$, thereby completely neglecting bosonic fluctuations. In momentum space the Lagrangian from (3.36) then reads

$$\mathcal{L}_{\text{PQMD}}^{\text{MF}} = \bar{\Psi} \left(S_{0,\text{MF}}^{-1} - i\gamma^0 \frac{a_0}{2} \right) \Psi + V_{\text{MF}}(\sigma, d^2) + \mathcal{U}_{\text{Pol}}, \quad (3.38)$$

¹⁰What we refer to as mean-field approximation here should be understood as leading order in a large- N_c expansion, i.e taking only into account fermionic loops for the calculation of the partition function, despite the fact that mesons and diquarks are also explicit degrees of freedom in the QMD Lagrangian. We abstain from including these degrees of freedom along the lines of [102] at this point as they will be consistently included within the framework of the FRG.

where

$$S_{0,\text{MF}}^{-1} = \begin{pmatrix} i\cancel{p} - \gamma^0 \mu + h\sigma & h\gamma^5 \Delta \\ -h\gamma^5 \Delta^* & i\cancel{p} + \gamma^0 \mu + h\sigma \end{pmatrix}, \quad (3.39)$$

and the mean-field potential is defined by $V_{\text{MF}}(\sigma, d^2) = (\lambda/4) (\sigma^2 + d^2 - v^2)^2 - c\sigma - 2\mu^2 d^2$ with $d^2 \equiv |\Delta|^2$. The last term is the contribution from the diquark kinetic part of Eq. (3.28) and breaks the $SU(4)$ symmetry of the potential in addition to the explicit chiral symmetry breaking by $c\sigma$. The details of the parameter fixing¹¹ and the values used in the numerical calculations are given in [1]. Performing the fermion-loop integration now yields the grand potential

$$\Omega(T, \mu) = -T \sum_{n \in Z} \int \frac{d^3 p}{(2\pi)^3} \text{Tr} \log (S_{0,\text{MF}}^{-1} - i\gamma^0 \frac{a_0}{2}) + V_{\text{MF}}(\sigma, d^2) + \mathcal{U}_{\text{Pol}}, \quad (3.40)$$

where the trace runs over internal indices (Dirac-, flavor- and Nambu-Gorkov space) and we sum over antiperiodic Matsubara modes $\nu_n = (2n+1)\pi T$. We can rewrite Eq. (3.40) by noting that the four distinct eigenvalues of $\gamma^0 S_{0,\text{MF}}^{-1}$ are given by $\pm E_p^+ + i\nu_n$ and $\pm E_p^- + i\nu_n$ with

$$E_p^\pm = \sqrt{\epsilon_p^{\pm 2} + h^2 d^2}, \quad \epsilon_p^\pm = \epsilon_p \pm \mu \quad \text{and} \quad \epsilon_p = \sqrt{\vec{p}^2 + h^2 \sigma^2}. \quad (3.41)$$

The Matsubara sum can be performed analytically leading to the final result

$$\begin{aligned} \Omega(\sigma, d^2, \Phi) = & -4 \sum_{\pm} \int \frac{d^3 p}{(2\pi)^3} \left\{ E_p^\pm + T \log \left(1 + 2\Phi e^{-\beta E_p^\pm} + e^{-2\beta E_p^\pm} \right) \right\} \\ & + V_{\text{MF}}(\sigma, d^2) + \mathcal{U}_{\text{Pol}}. \end{aligned} \quad (3.42)$$

Retaining only the quadratic parts of the potential, this expression coincides with the Hubbard-Stratonovich transformed PNJL model result [98] apart from the model independent $-2\mu^2 d^2$ from the diquarks' kinetic term, which does not show up explicitly in the grand potential of the (P)NJL model. As usual, one obtains temperature and chemical potential dependent condensates σ , d and Φ from solving the gap equations,

$$\frac{\partial \Omega}{\partial \sigma} = \frac{\partial \Omega}{\partial d} = \frac{\partial \Omega}{\partial \Phi} = 0, \quad (3.43)$$

and determining the solution which minimizes Ω .

Role of vacuum contributions

At this point a few words are in order concerning the role of vacuum contributions as they were subject of longer debates in the community [104]. Therefore, note that the fermion-loop contribution in Eq. (3.42) contains an ultraviolet divergent part. In

¹¹As 2-color QCD is an unphysical theory there is no canonical choice of physical parameters. We employ a simple N_c -scaling of 3-color parameter values, where $f_\pi \sim \sqrt{N_c}$ and $h \sim 1/N_c$ but meson masses remain independent of N_c .

3. Quark-Meson-Diquark Models for QCD-like Theories

quark-meson model mean-field studies it has been a common procedure to employ the *no-sea approximation* where these divergent contributions are completely neglected with reference to the renormalizability of the model. This is, however, a rather crude approximation, which leads to inconsistencies in particular at finite chemical potentials.

To see how this comes about we start by considering the conventional expression for the mean-field grand potential

$$\Omega_q = \Omega_q^{\text{vac}} - 4N_c T \int \frac{d^3p}{(2\pi)^3} \sum_{\pm} \log \left(1 + e^{-\beta(\epsilon_p \pm \mu)} \right). \quad (3.44)$$

Here we demonstrate the effect of vacuum contributions by regulating the vacuum term with a sharp 3-momentum cutoff Λ and study its impact on the phase diagram in comparison to the dimensionally regularized result [104]. Rather than fixing the sigma meson mass to a fixed value, we adjust the sigma mass in each case to yield a common value of $T_c \approx 183$ MeV at $\mu = 0$. The corresponding phase diagrams are shown in Fig. 3.3 illustrating a considerable dependence of the position of the CEP on the 3-momentum cutoff Λ . With increasing Λ , its location gets shifted to larger chemical potentials approaching the dimensionally regularized result.

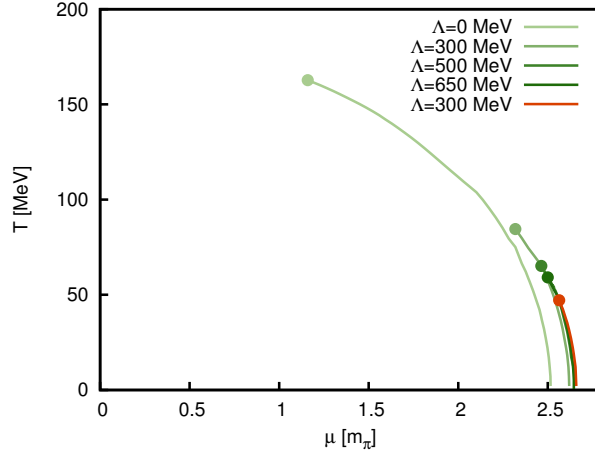


Figure 3.3.: Standard $N_c = 2$ QM model phase diagram from minimizing Eq. (3.44): dependence of the location of the CEP on the vacuum-term cutoff Λ in comparison to dimensionally regularized result.

More carefully, however, one observes that the fermion-loop contribution in the no-sea approximation ($\Omega_q^{\text{vac}} = 0$ for $\Lambda = 0$) in Eq. (3.44) does not tend to zero for $T \rightarrow 0$ when $\mu > g\sigma$, but still contains temperature independent contributions from momenta with $\vec{p}^2 < \mu^2 - h^2\sigma^2$. In the light of these considerations, the use of the no-sea approximation can at best be motivated as a way of modelling the restoration of chiral symmetry for large chemical potentials. A related observation is the fact that the $d \rightarrow 0$ limit of Eq. (3.42) with $E_p^- \rightarrow |\epsilon_p - \mu|$ does not coincide with the

conventional expression from Eq. (3.44) for $N_c = 2$ but rather yields

$$\begin{aligned} \Omega(\sigma) = & -4 \int \frac{d^3p}{(2\pi)^3} \left\{ \epsilon_p + \mu + |\epsilon_p - \mu| + 2T \log \left(1 + e^{-\beta(\epsilon_p + \mu)} \right) \right. \\ & \left. + 2T \log \left(1 + e^{-\beta|\epsilon_p - \mu|} \right) \right\} + V_{\text{MF}}(\sigma, 0), \end{aligned} \quad (3.45)$$

which differs by the appearance of the modulus of the quasi-particle energies $|\epsilon_p - \mu|$. Unlike before, the decomposition in Eq. (3.45) represents a proper separation of thermal and vacuum contributions from the fermion determinant. Note in particular that one can recover the conventional expression from Eq. (3.44) by exploiting the evenness of $\cosh(x)$,

$$|x| + 2 \log(1 + \exp(-|x|)) = 2 \log \cosh(x/2) + 2 \log 2, \quad (3.46)$$

under the assumption that thermal and vacuum parts are regularized in the same way as for example commonly done in the NJL model. If the thermal part is fully retained in order to comply with the Stefan-Boltzmann limit as it is done here, one can consider the difference between the two expressions Eq. (3.44) and Eq. (3.45) as a measure for the reliability of the calculation. In this way one is lead to the natural conclusion that the cutoff scale Λ should be chosen at least as large as the largest value of chemical potential μ under consideration. Although in principle a treatment of the vacuum contributions in dimensional regularization might be desirable also in 2-color QCD, we will continue to regulate vacuum terms with a sharp 3-momentum regulator as the dimensional regularization procedure becomes impracticable in the 2-color case in presence of a non-vanishing diquark condensate.

As a final remark on this subject we point out that this approach of regularizing the vacuum term with a sharp momentum cutoff arises naturally in the context of a particular approximation of the flow equation of the effective potential where only the fermionic contributions are retained. For a sharp 3-momentum regulator as the one used in Eq. (3.66) this corresponds to a vacuum term regulated with a sharp momentum cutoff given by the UV scale in the FRG. Although the result will of course also depend on the regulator choice in the FRG, defining the mean-field approximation as a particular approximation of the flow equation represents on the one hand a more consistent framework than an arbitrary choice of regularization scheme as employed in standard mean-field approaches and is on the other hand already the appropriate framework for a treatment beyond the mean-field approximation.

3.3.2. Diquark condensation

Zero-temperature condensates

Already at the level of the mean-field approximation it is obvious that the phase diagrams represented in Fig. 3.3, which neglect the possibility of the diquarks to condense, do not represent a complete picture of the phase diagram of 2-color QCD. Furthermore, it is a well-known exact result from chiral perturbation theory that at $T = 0$ diquark condensation has to set in at $2\mu_c(T = 0) = m_\pi$, which is perfectly

3. Quark-Meson-Diquark Models for QCD-like Theories

consistent with the requirements of the Silver Blaze property for a continuous zero-temperature phase transition. The line of critical chemical potential $\mu_c(T)$ then extends into the finite temperature and chemical potential plane bounding the superfluid diquark phase. We start, however, with the discussion of zero-temperature results by means of Fig. 3.4 where we show the zero-temperature chiral condensate and diquark condensate in dependence of chemical potential. Fig. 3.4 illustrates that the QMD model results compare very well to other approaches to 2-color QCD such as chiral perturbation theory, the $O(6)$ linear sigma model, the NJL model and even lattice data.

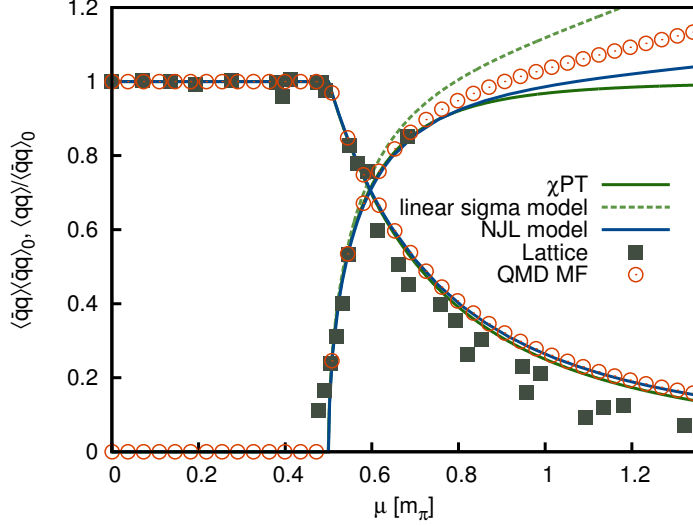


Figure 3.4.: Condensates at $T = 0$ [1](NJL parameter values from [105]; lattice data from [84]; linear sigma model with $m_\pi = 138$ MeV and $m_\sigma = 680$ MeV).

The zero-temperature linear sigma model expressions for the condensates normalized by the vacuum value σ_0 of the chiral condensate are derived straightforwardly by minimizing the bosonic potential [106],

$$\begin{aligned} \frac{\sigma}{\sigma_0} &= \begin{cases} 1 & \text{for } \mu < \mu_c \\ \frac{1}{x^2} & \text{for } \mu > \mu_c \end{cases}, \\ \frac{|\Delta|}{\sigma_0} &= \begin{cases} 0 & \text{for } \mu < \mu_c \\ \sqrt{1 - \frac{1}{x^4} + 2\frac{x^2-1}{y^2-1}} & \text{for } \mu > \mu_c \end{cases}, \end{aligned} \quad (3.47)$$

and depend just on the dimensionless ratios $x = 2\mu/m_\pi$ and $y = m_\sigma/m_\pi$. In the limit of an infinitely heavy sigma meson, i.e. for $y \rightarrow \infty$, one recovers the leading order chiral perturbation theory result [96]. Note that the chiral condensate in the linear sigma model remains independent of the sigma mass, whereas the asymptotic slope of the diquark condensate is sigma-mass dependent. The different behavior of the diquark condensates in Fig. 3.4 for large chemical potentials can be understood simply in terms of different sigma masses.

Mean-field phase diagram

Having discussed the chemical potential dependence of the condensates at zero temperature, we now turn to the phase diagrams as obtained from mean-field calculations. These are shown in Fig. 3.5, where we compare mean-field QMD model results to the corresponding NJL model. In the light of the discussion from above, we only present results QMD results for a cutoff $\Lambda = 600$ MeV, which should be reasonably large for the chemical potentials under consideration. In the QMD calculation we compare two different definitions for the chiral crossover. The definition via the point where the chiral condensate reaches half of its value at $T = \mu = 0$ illustrates transparently the decay of the chiral condensate and the asymptotic restoration of chiral symmetry in the diquark condensation phase. On the other hand the definition of the chiral crossover via the peak in the corresponding temperature derivative is a better quantitative criterion in particular with respect to later a comparison to the deconfinement crossover but it does not reflect the asymptotic restoration of chiral symmetry with increasing chemical potential.

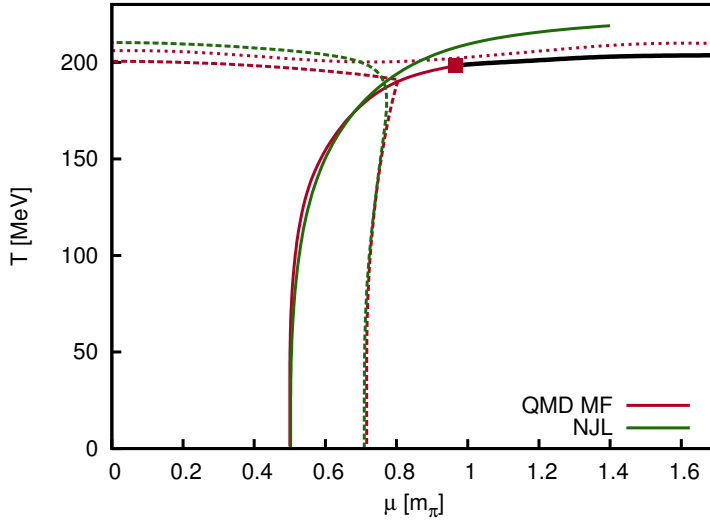


Figure 3.5.: Mean-field phase diagrams: QMD model with $\Lambda = 600$ MeV versus NJL model (with parameters from [105]); dashed: chiral crossover (half-value of the condensate); dotted: chiral crossover (inflection point); solid: second order transition; thick solid: first order transition; square: tricritical point.

In addition to the usual chirally broken phase with vanishing diquark condensate at small temperatures and chemical potentials and a phase at large temperatures where chiral symmetry is asymptotically restored, one finds a diquark condensation phase for $\mu > \mu_c(T)$, which is characterized by a nonvanishing diquark condensate and correspondingly by a rapid rise in baryonic density. Comparing Fig. 3.5 to the phase diagram from Fig. 3.3, where diquarks as baryonic degrees of freedom are neglected, it

3. Quark-Meson-Diquark Models for QCD-like Theories

is already clear at mean-field level that the critical point disappears in the diquark condensation phase and is no longer observed in the full QC₂D calculation. We will discuss the consequences of this observation in more detail in the RG section.

There is, however, an apparent disagreement between the mean-field treatment of the QMD model and the NJL model, which caused confusion in the literature and which we hope to clarify at this point. It concerns the appearance of a tricritical point on the phase boundary of the diquark condensation phase where the transition turns from second order to first order. We claim that the occurrence of the tricritical point is closely related to the effects of thermal UV contributions, in the sense that only calculations where the full thermal contributions were retained show a tricritical point. This applies to the mean-field QMD model calculation from above, where, as usual in quark-meson model calculations, the thermal part was kept unregulated, but also to next-to-leading order χ PT [107], where dimensional regularization was applied and which predicts a tricritical point at $\mu \approx 0.57m_\pi$ and $T \approx 220$ MeV. The tricritical point from the QMD model calculation, see Fig. 3.5, lies in a comparable temperature range but shows a considerable dependence on the vacuum term cutoff Λ . On the other hand, in the NJL model calculation both the thermal and the medium part were regulated with a sharp cutoff and the phase boundary remained second order throughout the whole investigated parameter range as verified in a Ginzburg Landau analysis [98].

3.3.3. RPA mass spectrum and the Silver Blaze property

Exact statements about pole and screening masses

The purpose of this section is to illustrate a number of exact statements about the pole masses, their relation to the commonly used screening masses, and to the Silver Blaze property which can be made in the mean-field approximation. The determination of meson-/diquark masses and in particular of the pion mass is crucial to check the consistency of the results with the Silver Blaze property. As pointed out before there is an important distinction between screening masses, which are commonly considered in quark meson-model studies and simply determined by the curvature of the effective potential at its minimum, and pole-masses defined by the poles of propagator or equivalently by the zeros of the corresponding 2-point functions. More explicitly, the latter are defined via the zeros of the determinant of the inverse propagator

$$\Gamma_{ij}^{(2)}(p) = \Gamma_{\text{tl}}^{(2)}(p)_{ij} + \Pi_{ij}(p) \quad (3.48)$$

with a tree-level contribution in a real basis $(\phi_i) = (\sigma, \text{Re } \Delta, \text{Im } \Delta, \vec{\pi})^T$ given by

$$\Gamma_{\text{tl}}^{(2)}(p) = \begin{pmatrix} p^2 - m^2 + \lambda\phi^2 + 2\lambda\sigma^2 & 2\lambda\sigma d & 0 & 0 \\ 2\lambda\sigma d & p^2 - m^2 + \lambda\phi^2 + 2\lambda d^2 - 4\mu^2 & -4\mu p_0 & 0 \\ 0 & 4\mu p_0 & p^2 - m^2 + \lambda\phi^2 - 4\mu^2 & 0 \\ 0 & 0 & 0 & \mathbb{1}_{3 \times 3}(p^2 + m^2 + \lambda\phi^2) \end{pmatrix}, \quad (3.49)$$

3.3. QMD Model for QC_2D : Mean-Field Analysis

with $\phi^2 = \sigma^2 + d^2$ and $m^2 = \lambda v^2$ and a RPA contribution from evaluating a fermion-loop integral with external momentum p

$$\Pi_{ij}(p) = \text{Tr}_q \left[\left. \frac{\partial \Gamma_F^{(2)}}{\partial \phi_i} \right|_{\phi_{\text{MF}}} G_{\text{MF}}(p+q) \left. \frac{\partial \Gamma_F^{(2)}}{\partial \phi_j} \right|_{\phi_{\text{MF}}} G_{\text{MF}}(q) \right], \quad (3.50)$$

where $G_{\text{MF}} = \left(\Gamma_F^{(2)}|_{\phi_{\text{MF}}} \right)^{-1}$ and $(\phi_{\text{MF}}) = (\sigma, d, 0, \vec{0})^T$. These polarization integrals have been calculated in the literature [98, 108] for the related problem of isospin chemical potential in a 2-flavor 3-color NJL model and have been recalculated and tabulated explicitly in [1]. In accordance with our treatment of the grand potential, the vacuum contributions are understood as evaluated for a sharp momentum cutoff rendering them UV finite while the thermal contributions remain unregulated, see [1] for details.

To extract pole masses it is sufficient to consider the case of a vanishing spatial external momentum.¹² Therefore, we define the short-hand notations $\Gamma^{(2)}(\omega) \equiv \Gamma^{(2)}(p = (-i\omega, \vec{0}))$ and correspondingly $\Pi(\omega) \equiv \Pi(p = (-i\omega, \vec{0}))$. Meson and diquark masses are then defined as solutions of the equation

$$\det \Gamma^{(2)}(\omega) = 0. \quad (3.51)$$

It is insightful to discuss the explicit expressions for the meson and diquark masses in the normal phase where no diquark condensation occurs. In a complex basis with $\Delta = \phi_5 + i\phi_6$ and $\Delta^* = \phi_5 - i\phi_6$ both tree level contributions and polarization integrals are diagonal. Thus the determinant factorizes and the meson and diquark masses are simply determined as solutions of the four equations

$$\begin{aligned} m_\sigma : \quad \omega^2 &= -m^2 + 3\lambda\sigma^2 + \Pi_\sigma(\omega, T) \\ m_\pi : \quad \omega^2 &= -m^2 + \lambda\sigma^2 + \Pi_\pi(\omega, T) \\ m_\pm : \quad (\omega \pm 2\mu)^2 &= -m^2 + \lambda\sigma^2 + \Pi_\pm(\omega, T). \end{aligned} \quad (3.52)$$

¹²Note again the subtlety associated to the limit $\omega \rightarrow 0$ and $\vec{p} \rightarrow \vec{0}$ at finite temperature, which was discussed in detail in Section 2.2.1. Only the additional contribution, cf. Π_σ in Eq. (3.53), arising for $\omega = 0$ from the screening mass prescription $\vec{p} \rightarrow \vec{0}$ after $\omega \rightarrow 0$ ensures the consistency of the sigma pole mass at zero external momentum with the screening mass.

3. Quark-Meson-Diquark Models for QCD-like Theories

The polarization integrals are in this case given by

$$\begin{aligned}
\Pi_\sigma(\omega, T) &= 16N_c h^2 \int \frac{d^3q}{(2\pi)^3} \frac{q^2}{\epsilon_q} \frac{1 - N_q(\epsilon_q^-) - N_q(\epsilon_q^+)}{\omega^2 - 4\epsilon_q^2} \\
&\quad + 4N_c h^2 \delta_{\omega,0} \int \frac{d^3q}{(2\pi)^3} \frac{h^2 \sigma^2}{\epsilon_q^2} (N'_q(\epsilon_q^+) + N'_q(\epsilon_q^-)) \\
\Pi_\pi(\omega, T) &= 16N_c h^2 \int \frac{d^3q}{(2\pi)^3} \frac{\epsilon_q (1 - N_q(\epsilon_q^-) - N_q(\epsilon_q^+))}{\omega^2 - 4\epsilon_q^2} \\
\Pi_\pm(\omega, T) &= 4N_c h^2 \int \frac{d^3q}{(2\pi)^3} \left(\frac{1 - 2N_q(\epsilon_q^\mp)}{\omega - 2\epsilon_q^\mp} - \frac{1 - 2N_q(\epsilon_q^\pm)}{\omega + 2\epsilon_q^\pm} \right)
\end{aligned} \tag{3.53}$$

with $\epsilon_q^\pm = \sqrt{q^2 + h^2 \sigma^2} \pm \mu$ and Polyakov loop enhanced quark/antiquark occupation numbers

$$N_q(E) \equiv N_q(E; T, \Phi) = \frac{1 + \Phi e^{\frac{E}{T}}}{1 + 2\Phi e^{\frac{E}{T}} + e^{\frac{2E}{T}}}, \tag{3.54}$$

which simplify to the Fermi-Dirac distribution $n_q(E) = (\exp(E/T) + 1)^{-1}$ for $\Phi = 1$. Using the explicit expression for the grand potential, Eq. (3.42), it is straightforward to verify [1] that the polarization functions at zero external momentum $\omega = 0$ reduce to combinations of derivatives of the grand potential, which allows one to write the screening masses defined via the eigenvalues of the Hessian evaluated at its minimum as

$$\begin{aligned}
m_\sigma^{\text{sc}2} &= -m^2 + 3\lambda\sigma^2 + \Pi_\sigma(0, T), \\
m_\pi^{\text{sc}2} &= -m^2 + \lambda\sigma^2 + \Pi_\pi(0, T), \\
m_\pm^{\text{sc}2} &= -4\mu^2 - m^2 + \lambda\sigma^2 + \Pi_\pm(0, T).
\end{aligned} \tag{3.55}$$

The comparison to Eqs. (3.52) shows that the square of the screening masses for sigma meson and pion coincide with corresponding inverse propagator evaluated at vanishing external momentum $\omega = 0$. Note that by construction the diquark screening masses do not show a splitting with the chemical potential but remain degenerate outside the diquark condensation phase as $\Pi_+(0, T) = \Pi_-(0, T)$. Another general observation is the fact that for $\mu = 0$ the polarization functions satisfy $\Pi_\pi(\omega, T) = \Pi_\pm(\omega, T)$, which entails for both pole and screening masses at $\mu = 0$ that pions and diquarks become degenerate as required by the enlarged $SO(6)$ flavor symmetry.

However, the most important observation is the following. Consider the gap equation for the diquark condensate,

$$\frac{\partial}{\partial d} \Omega = d \left(-m^2 + \lambda\sigma^2 - 4\mu^2 + 2 \frac{\partial}{\partial d^2} \Omega_q(T, \mu) \right) = 0 \tag{3.56}$$

and note that for $d = 0$ the zero of the term in brackets implicitly defines the critical chemical potential $\mu_c(T)$ associated to the onset of diquark condensation as it determines the value from where on a second non-trivial solution for the diquark condensate develops. But again using $\Pi_-(0, T) = 2 \frac{\partial}{\partial d^2} \Omega_q(T, \mu)|_{d=0}$ and Eq. (3.52) it

is easy to verify that this condition is equivalent to the requirement of one diquark becoming massless, i.e. $m_- = 0$. This just expresses the fact that at any temperature the onset of diquark condensation is marked by the chemical potential for which one of the diquarks becomes massless, which is intuitively clear as the diquark mass depends continuously on chemical potential and one expects one Goldstone boson in the diquark condensation phase.

Let us finally consider the special case of zero temperature. Here one has in addition the relation $\Pi_{\pm}(\omega, 0) = \Pi(\omega \pm 2\mu, 0)$ and thus finds in the normal phase the mass relation

$$m_{\pm} = m_{\pi} \pm 2\mu, \quad (3.57)$$

which implies that the diquark masses stay constant up to $\pm 2\mu$, reflecting their coupling to the baryon chemical potential $\mu_B = 2\mu$, whereas the pion mass stays strictly independent of the chemical potential in the normal phase as required by the Silver Blaze property. As the onset of diquark condensation is defined via $m_- = 0$ this implies the exact statement

$$2\mu_c(0) = m_{\pi} \quad (3.58)$$

linking the zero-temperature critical chemical potential $\mu_c(0)$ to the pion mass. In this sense the critical chemical potential associated to the onset of diquark condensation at zero temperature can be seen as definition of the physical pion mass. We will exploit this property to fix the pion mass in the FRG calculation, where a consistent calculation of the pion pole mass adopted to the truncation under consideration is more involved.

Zero-temperature RPA mass spectrum

Having discussed the zero-temperature mass spectrum in the normal phase in the last paragraph, we close the section on the mean-field analysis of the QMD model with a general discussion of the zero-temperature mass spectrum. The complication which arises in the diquark condensation phase compared to the normal phase is the fact that the sigma meson mixes with the two diquark modes which reflects itself in non-diagonal terms arising both in the tree level contribution and in the polarization functions, see Eq. (3.49) and Eq. (3.50). Whereas the pion pole mass is still determined by the single equation (3.52), sigma meson and diquark masses have to be calculated from the zeros of the determinant of the corresponding 3×3 matrix.

As observed in previous NJL studies [98], one can still make a number of exact statements about the mass spectrum. In the zero-temperature case the pion mass is required to be constant up to the onset and has to rise as $m_{\pi} = 2\mu$ above the onset. Furthermore, one verifies explicitly that also at finite temperature always one massless mode arises in the diquark condensation phase, which can obviously be identified with the Goldstone boson associated to the broken $U(1)_B$ symmetry in the diquark condensation phase. These general statements are nicely reflected in the numerical results shown in Fig. 3.6.

One also observes that one massive mode becomes degenerate with the pions at

3. Quark-Meson-Diquark Models for QCD-like Theories

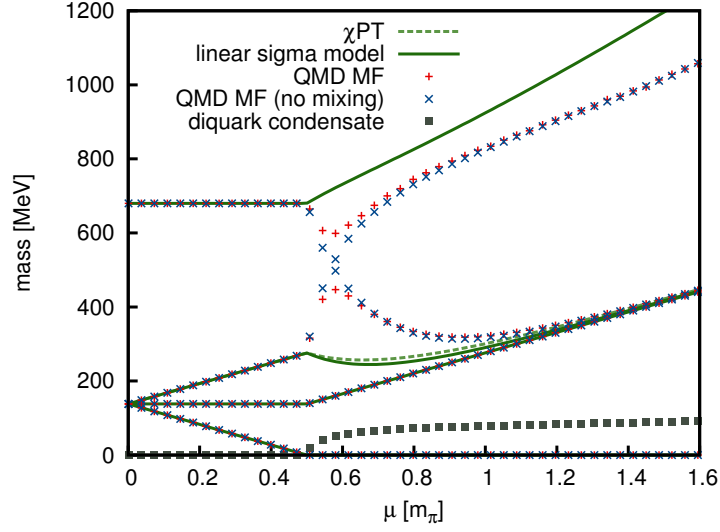


Figure 3.6.: Zero-temperature pole-mass spectrum [1]: mean-field/RPA QMD model results (with vacuum-term cutoff $\Lambda = 600$ MeV), for comparison also shown without the effect of diquark/sigma-meson mixing in the superfluid phase, vs. linear sigma model.

asymptotically large chemical potentials. It is only possible to assign it to a particle in this particular limit as the sigma meson and the diquarks mix in the diquark condensation phase at finite chemical potential. For an asymptotically large chemical potential this mode should be interpreted as sigma meson whose mass degeneracy with the pions signals the restoration of chiral symmetry as the chiral condensate vanishes for asymptotically large chemical potentials. As remarked above, the complete restoration of chiral symmetry is a particular feature of the two flavor model where only one Goldstone boson arises in the diquark condensation phase. In Fig. 3.6 we also show results from a mass calculation neglecting mixing terms both in the tree-level contribution and in the polarization functions. The mixing represents an important effect at a region of intermediate chemical potentials in the diquark condensation which we will identify as region of the BEC-BCS crossover in Section 3.4.4. Furthermore, the calculation without mixing clearly illustrates the mass assignment of the mass mode which becomes degenerate with the pions at asymptotically large chemical potential to the sigma meson.

The effect of vacuum fluctuations can be inferred by comparing to the linear sigma model mass spectrum, corresponding to the no-sea approximation of the QMD model, which is obtained straightforwardly from the eigenvalues of the Hessian of the potential

and reads in the diquark condensation phase

$$\begin{aligned}
 m_\pi &= 2\mu, & m_{\Delta_1} &= 0, \\
 m_{\sigma/\Delta_2} &= \frac{m_{\pi,0}}{\sqrt{2}} \left(-3 + y^2 + 7x^2 \pm (12(1 - y^2)/x^2 + (-3 + 5x^2 + y^2)^2)^{\frac{1}{2}} \right)^{\frac{1}{2}}, \quad (3.59)
 \end{aligned}$$

where $x = 2\mu/m_\pi$ and $y = m_\sigma/m_\pi$ as above. As for the diquark condensate before, one can easily convince oneself of the consistency with leading order χ PT [96]. In the limit of an infinitely heavy sigma mass, $y \rightarrow \infty$, the expression for the second diquark mass reduces to the χ PT result $m_{\Delta_2} = 2\mu\sqrt{1 + 3x^{-4}}$.

3.4 QMD Model for QC₂D: FRG Analysis

3.4.1. Symmetries, truncations and flow equations

Symmetries of the microscopic action

Before we turn to the discussion of the truncation used in our analysis it is worthwhile to investigate the symmetries of the microscopic QMD model action as defined via Eq. (3.26). This is particularly important since the Ansatz for the effective average action and ideally also the regulator should be consistent with all symmetries of the microscopic action. Here we will be mainly concerned with the continuous symmetries of the Lagrangian. The discussion can be lead very analogous to the non-relativistic case [89] with similar consequences. The symmetries are most naturally discussed in Minkowskian signature, where the microscopic action corresponding to the Euclidean Lagrangian from Eq. (3.26) after continuation to $t = i\tau$ reads

$$\begin{aligned}
 S_{\text{QMD},2\text{cf}}^{\text{Mink.}} &= \int dt \int d^3x \bar{\psi} (i\not{D} - h(\sigma - i\gamma^5 \vec{\pi} \vec{\tau}) + \mu\gamma^0) \psi \\
 &+ \frac{\hbar}{2} \left(\Delta^* (\psi^T C \gamma^5 \tau_2 i S \psi) + \Delta (\psi^\dagger C \gamma^5 \tau_2 i S \psi^*) \right) \\
 &+ \frac{1}{2} \partial_\mu \sigma \partial^\mu \sigma + \frac{1}{2} \partial_\mu \vec{\pi} \partial^\mu \vec{\pi} + \frac{1}{2} ((\partial_\mu - 2i\mu \delta_\mu^0) \Delta) (\partial^\mu + 2i\mu \delta_0^\mu) \Delta^* + V(\vec{\phi}) . \quad (3.60)
 \end{aligned}$$

As already observed in Eq. (3.24), the action is invariant under $U(1)_B$ phase rotations

$$\psi \rightarrow e^{i\alpha} \psi, \quad \bar{\psi} \rightarrow e^{-i\alpha} \bar{\psi}, \quad \Delta \rightarrow e^{2i\alpha} \Delta, \quad \Delta^* \rightarrow e^{-2i\alpha} \Delta^*, \quad (3.61)$$

associated to quark number conservation. This reiterates the fact that (anti-)diquarks carry quark number ± 2 . These transformations are of course just special cases of the enlarged $SU(4)$ flavor transformations discussed above, which are most conveniently formulated on the level of the spinors Ψ transforming via a $SU(4)$ matrix, see Eq. (3.21), and $(\phi_i) = (\sigma, \vec{\pi}, \text{Re } \Delta, \text{Im } \Delta)^T$ transforming as a complex $SO(6)$ vector. At finite chemical potential this requirement is weakened to an invariance under $SU(2)_V \times U(1)_B$

3. Quark-Meson-Diquark Models for QCD-like Theories

transformations, which is of course not only valid for the effective potential but also for interaction terms such as Yukawa interactions and allows for example different Yukawa couplings for mesons and diquarks at nonvanishing chemical potential. This additional possibility of breaking the $SO(6)$ symmetry via the interaction terms should be taken into account in improved truncations, see the discussion in Section 3.5.3.

At zero temperature the action is Lorentz invariant,

$$\psi(x) \rightarrow \Lambda_{\frac{1}{2}} \psi(\Lambda^{-1}x), \quad \phi_i(x) \rightarrow \phi_i(\Lambda^{-1}x), \quad (3.62)$$

which can be verified explicitly using $\Lambda_{\frac{1}{2}}^T C \gamma^5 = C \gamma^5 \Lambda_{\frac{1}{2}}^{-1}$, see Appendix A. Even at zero temperature Lorentz invariance gets broken spontaneously by the formation of a diquark condensate $\langle \Delta^* \Delta \rangle$, which goes in hand with a spontaneous breaking of the $U(1)_B$ baryon number symmetry. At finite temperature Lorentz invariance is broken explicitly as the heat bath singles out a preferred Lorentz frame.

Finally, there is an additional continuous symmetry which involves not only a transformation of the fields but also of the chemical potential as external field and is thus not a symmetry in the strict sense

$$\begin{aligned} \psi(t, x) &\rightarrow e^{i\alpha(t)} \psi(t, x), & \bar{\psi}(t, x) &\rightarrow e^{-i\alpha(t)} \bar{\psi}(t, x), & \Delta(t, x) &\rightarrow e^{2i\alpha(t)} \Delta(t, x), \\ \Delta^*(t, x) &\rightarrow e^{-2i\alpha(t)} \Delta^*(t, x), & \mu &\rightarrow \mu + \partial_t \alpha. \end{aligned} \quad (3.63)$$

From the viewpoint of the transformation laws the chemical potential acts here like the zero component of a $U(1)$ gauge field coupled to charged fermions and scalars, which is why this symmetry is referred to as semilocal symmetry in the literature [89].

At zero temperature Lorentz invariance and semilocal symmetry now enforce derivative terms in the Ansatz for the Euclidean effective average action to be constructed out of covariant derivatives

$$(D_\Delta)_\mu = \partial_\mu - 2\mu\delta_\mu^0, \quad (D_{\Delta^*})_\mu = \partial_\mu + 2\mu\delta_\mu^0, \quad (D_\psi)_\mu = \partial_\mu - \mu\delta_\mu^0 \quad (3.64)$$

for (anti-)diquarks and quarks respectively. This, together with the requirement of the consistency with the enlarged flavor symmetry discussed above, can then be used as guiding principle for the construction of higher order interaction terms consistent with the symmetries of the microscopic action.¹³

Regulator choices

While the result of the flow of the full theory at $k = 0$ is independent of the employed regulator function, this is no longer the case as soon as one considers truncations. In this case not only the path in theory space, but also the result of the flow at $k = 0$ will depend on the chosen regulator. Investigating the sensitivity of the results on

¹³These are obviously only constraints for the effective average action at zero temperature. At finite temperature there is no semilocal symmetry and Lorentz invariance is broken, which allows in principle more general structures which will, however, not be considered here.

the regulator is then one way of estimating systematic errors of a given truncation. The regulator choice is closely linked to the subject of optimization of RG-flows, i.e. trying to find a regulator which is optimal in the sense that it minimizes the difference to the full solution [44, 51]. Ideally the regulator should be chosen consistent with all symmetries of the theory as otherwise these symmetries will be broken by the regulator.

Throughout this thesis we will employ 3-momentum regulators, i.e. regulators of the generic form

$$R_{k,B} = \vec{p}^2 r_{k,B}(x), \quad R_{k,F} = i\vec{p}r_{k,F}(x) \quad \text{with} \quad x = \frac{\vec{p}^2}{k^2} \quad (3.65)$$

for bosonic or fermionic degrees of freedom respectively, and in particular the sharp regulators

$$r_{k,B}(x) = \left(\frac{1}{x} - 1\right) \theta(1-x) \quad \text{and} \quad r_{k,F}(x) = \left(\frac{1}{\sqrt{x}} - 1\right) \theta(1-x), \quad (3.66)$$

which are the 3-momentum analogues of the LPA optimized sharp regulators [51] which are frequently employed in finite-temperature investigations [109, 110]. Obviously these regulators break Lorentz invariance at $T = 0$. This is less of a problem in simple truncations like the ones considered in this thesis, but more in more refined truncations [110], where it has to be taken into account either via modified Ward identities or via an appropriate tuning of initial conditions. More problematic also for finite temperature applications is, however, the fact that 3-momentum regulators do not regulate the zero component of the momentum, which allows in principle infinitely large frequency transfers and correspondingly non-local contributions to the effective action, cf. the discussion in [64]. Ultimately, in more refined truncations in particular with momentum dependent vertices one should therefore consider 4-momentum regulators [111]. On the other hand such regulators represent a technical complication as in most cases they no longer allow an analytical evaluation of the Matsubara sums occurring in finite temperature calculations. The results in this thesis were particularly obtained with the sharp 3-momentum regulators from Eq. (3.66) for which even the spatial momentum integration becomes trivial which represents another technical simplification in particular considering the bosonic contributions to the flow of the effective potential, see Appendix D.2. Note in particular that the 3-momentum regulators are consistent with the semilocal symmetry from Eq. (3.63) as they do not involve the zero component of the momentum.

Flow equation for the effective potential

The Ansatz for the effective average action in leading-order derivative expansion, where only a scale-dependent effective potential is taken into account, reads

$$\Gamma_k = \int d^4x \mathcal{L}_{\text{PQMD}} \Big|_{V+c\sigma \rightarrow U_k} \quad (3.67)$$

3. Quark-Meson-Diquark Models for QCD-like Theories

with $\mathcal{L}_{\text{PQMD}}$ from Eq. (3.36), up to the substitution of $V(\vec{\phi})$ by $U_k - c\sigma$. The explicit symmetry breaking term $c\sigma$ does not affect the flow and is added to the effective potential after the integration of the flow equation. As remarked above it is crucial for the Ansatz to be consistent with the symmetries of the microscopic Lagrangian. Here this concerns only the effective potential, which has to be consistent with the enlarged $SO(6)$ flavor symmetry at $\mu = 0$ i.e. which can be parametrized by the modulus of the $SO(6)$ vector $\vec{\phi} = (\sigma, \vec{\pi}, \text{Re } \Delta, \text{Im } \Delta)^T$. However, at nonvanishing chemical potential the residual symmetry is only $SO(4) \times SO(2)$. In this case one has to allow the effective potential to depend on two invariants, i.e. $U_k \equiv U_k(\rho^2, d^2)$, where $\rho^2 = \sigma^2 + \vec{\pi}^2$ and $d^2 = |\Delta|^2$ as before. This allows in particular also to describe an $SO(6)$ symmetric potential again if the effective potential depends only on the combination $\phi^2 = \rho^2 + d^2$, as it will be the case for the flow equation for vanishing chemical potential.

The flow equation for the effective potential of the PQMD model is derived in Appendix D.2 and reads explicitly employing sharp 3-momentum regulators as given in Eq. (3.66)

$$\partial_t U_k = \frac{k^5}{12\pi^2} \left\{ \frac{3}{E_k^\pi} \coth\left(\frac{E_k^\pi}{2T}\right) + \sum_{i=1}^3 \frac{3z_i^4 - \alpha_1 z_i^2 + \alpha_0}{(z_{i+1}^2 - z_i^2)(z_{i+2}^2 - z_i^2)} \frac{1}{z_i} \coth\left(\frac{z_i}{2T}\right) - \sum_{\pm} \frac{8}{E_k^\pm} \left(1 \pm \frac{\mu}{\epsilon_k}\right) \left(1 - 2N_q(E_k^\pm; T, \Phi)\right) \right\}, \quad (3.68)$$

where $\epsilon_k = \sqrt{k^2 + h^2 \rho^2}$, $E_k^\pi = \sqrt{k^2 + 2U_{k,\rho}}$, $N_q(E; T, \Phi)$ are the Polyakov loop enhanced quark occupation numbers from Eq. (3.54), α_i coefficient functions depending on derivatives of the effective potential and the chemical potential and z_i the roots of a cubic equation, see Appendix D.2 for details.

3.4.2. $SO(6)$ symmetric effective potential

It is insightful to consider an $SO(6)$ symmetric variant of the flow equation (3.68) obtained by explicitly setting $\Delta = 0$ and assuming an $SO(6)$ symmetric effective potential i.e. $U_{k,\phi} \equiv U_{k,\rho} = U_{k,d}$ and $U_{k,\phi\phi} \equiv U_{k,\rho\rho} = U_{k,\rho d} = U_{k,dd}$. In this case the flow equation (3.68) reduces to the more familiar looking form,

$$\partial_t U_k = \frac{k^5}{12\pi^2} \left\{ \frac{1}{E_k^\sigma} \coth\left(\frac{E_k^\sigma}{2T}\right) + \frac{3}{E_k^\pi} \coth\left(\frac{E_k^\pi}{2T}\right) + \sum_{\pm} \frac{1}{E_k^\pi} \coth\left(\frac{E_k^\pi \pm 2\mu}{2T}\right) - \frac{16}{\epsilon_k} \left(1 - N_q(\epsilon_k - \mu; T, \Phi) - N_q(\epsilon_k + \mu; T, \Phi)\right) \right\}, \quad (3.69)$$

with single-particle energies for mesons/diquarks $E_k^\pi = \sqrt{k^2 + 2U_{k,\phi}}$ and sigma $E_k^\sigma = \sqrt{k^2 + 2U_{k,\phi} + 4\phi^2 U_{k,\phi\phi}}$. Eq. (3.69) should be compared to the corresponding flow equation for the PQM model in the 3-color case [112, 113, 114], which takes a completely

analogous form apart from the changed number of colors and the isospin chemical potential-like coupling of one pseudo-Goldstone boson pair to the chemical potential. The correspondence to the 3-color quark-meson model with isospin chemical potential will be made more explicit in Chapter 4.

At this point one might be tempted to assume that the effective potential remains $SO(6)$ symmetric outside the diquark condensation phase apart from the trivial breaking $-4\mu^2 d^2$ from the kinetic term of the diquarks. In this case, if $U_{k,\rho} = U_{k,d}$ in particular at the minimum of the effective potential, one would be immediately lead to conclude that the pion screening and pole masses coincide as in both cases the zero-temperature diquark mass would behave like $m_{\Delta}^{-,\text{scr/pole}} = m_{\pi,0}^{\text{scr/pole}} - 2\mu$ in the normal phase. and both have to reach a common zero at the onset of diquark condensation. The comparison of the full calculation based on the Ansatz of an effective potential with the reduced $SO(4) \times SO(2)$ symmetry to the $SO(6)$ symmetric calculation reveals, however, already deviations outside the diquark condensation phase, see Section 3.4.4 for a detailed discussion. This means that there are μ -induced effects beyond the breaking from the kinetic term, reiterating the fact that the effective potential at finite chemical potential is a genuine function of two invariants $U_k = U_k(\rho^2, d^2)$. Nevertheless, although the 1-dimensional flow from Eq. (3.69) only exactly coincides with the full flow from Eq. (3.68) at zero chemical potential it represents a good approximation to the full solution for small chemical potentials.

Critical exponents β and δ

Following the long tradition of universality and scaling studies within the context of $O(4)$ models relevant for the chiral symmetry breaking transition in 3-color 2-flavor QCD [62, 115, 116], we perform here the corresponding analysis for the 2-color 2-flavor case. As pointed out before, at zero chemical potential diquarks and pions become degenerate due to the enlarged $SO(6)$ flavor symmetry. Completely analogous to the 3-color case, apart from the number of five instead of the usual three pions, this $SO(6)$ symmetry is then broken to $SO(5)$ by the formation of a chiral condensate. Thus the expected critical exponents in our calculation are those corresponding to the universality class of the three-dimensional $O(6)$ -model.

The critical exponents β and δ are easily extracted from the temperature dependence of the chiral condensate in the chiral limit or the quark mass/ explicit symmetry breaking parameter c dependence of the chiral condensate at the critical temperature respectively, i.e.

$$\langle \bar{q}q \rangle_T \sim (-t)^\beta, \quad \langle \bar{q}q \rangle_{T_c} \sim c^{\frac{1}{\delta}}. \quad (3.70)$$

Fig. 3.7 shows the data used for the extraction of the critical exponents, demonstrating scaling over several orders of magnitude. The critical exponents obtained from the corresponding fits are given by $\beta = 0.4318(4)$ and $\delta = 5.08(8)$, where the errors indicate statistical errors from the fit. For comparison the literature values obtained from Monte-Carlo simulations are given by $\beta = 0.425(2)$ and $\delta = 4.77(2)$ [117].

3. Quark-Meson-Diquark Models for QCD-like Theories

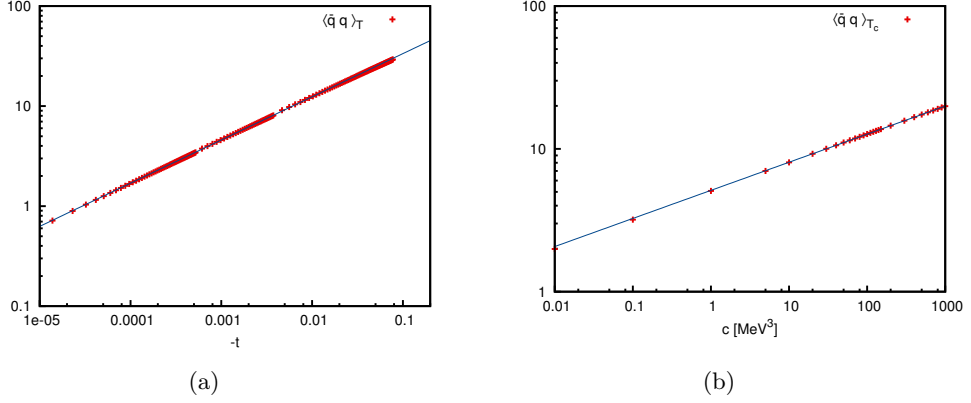


Figure 3.7.: Extraction of critical exponents β (a) and δ (b) [1].

Yet, considering the simplicity of our truncation the more appropriate benchmark are critical exponents obtained for the $O(6)$ model in the local potential approximation [55], where one finds $\nu = 0.863076$ and by definition a vanishing anomalous dimension $\eta = 0$ in the LPA. These critical exponents can be converted into β and δ using the well-known hyperscaling relations [37]

$$\delta = \frac{d+2-\eta}{d-2+\eta} \quad \text{and} \quad \beta = \frac{\nu}{2}(d-2+\eta), \quad (3.71)$$

which imply $\delta = 5$ and $\beta = \nu/2$ for $\eta = 0$ in $d = 3$ dimensions, leading to a literature value $\beta = 0.4315$. Thus the critical exponents obtained from our analysis agree within errors with literature values obtained in a comparable truncation, which demonstrates that the $O(6)$ symmetry breaking pattern at zero chemical potential is correctly realized in the QMD model.

Phase diagram without diquark fluctuations

One can now proceed to finite chemical potentials but still using the flow equation (3.69) with the $SO(6)$ symmetric effective potential parametrized by a single invariant $\phi^2 = \rho^2 + d^2$. This calculation represents the FRG analogue of the mean-field calculation corresponding to Fig. 3.3 with similar consequences. The corresponding phase diagrams are shown in Fig. 3.8 for comparison. Here the vacuum term in the mean-field calculation was regularized using a sharp 3-momentum cutoff $\Lambda = 600$ MeV and the sigma mass was adjusted to match the pseudocritical temperature of the RG calculation at vanishing chemical potential.

The phase diagrams show quantitative agreement between RG and mean-field calculations at least up to chemical potentials of the order of two pion masses. For larger chemical potentials there is at least a qualitative agreement as both show first order transitions and a critical endpoint at $\mu \approx 2.5m_\pi$ in the RG calculation

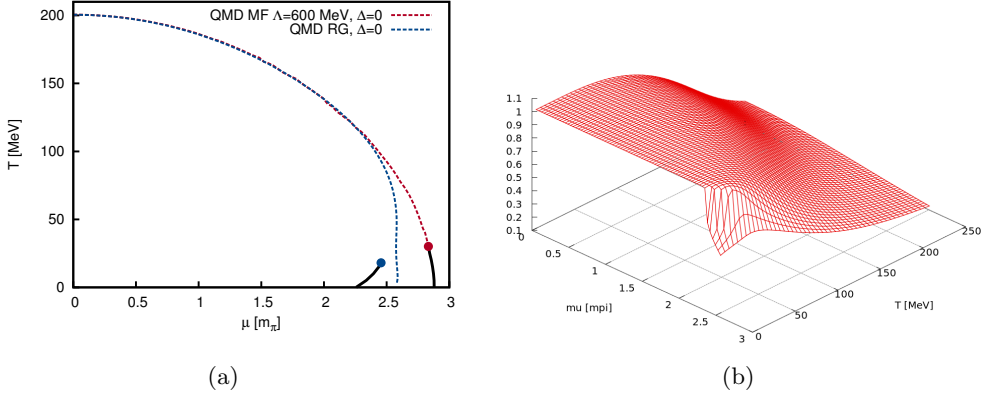


Figure 3.8.: QMD model phase diagram neglecting baryonic degrees of freedom:
 (a) Phase diagram from $SO(6)$ symmetric RG calculation versus the corresponding mean-field calculation; dashed: chiral crossover (half-value of the condensate); thick solid black: first order transition.
 (b) Normalized chiral condensate $\langle \bar{q}q \rangle / \langle \bar{q}q \rangle_0$ as function of temperature and chemical potential as obtained from RG calculation.

or $\mu \approx 2.8m_\pi$ in the mean-field calculation respectively. Again, there is a striking similarity to the corresponding phase diagrams obtained from (Polyakov-)quark-meson model calculations for $N_c = 3$ [112] but the conclusions from the mean-field section remain unchanged: Both calculations are equally inappropriate as effective descriptions for 2-color QCD at least for baryon chemical potentials of the order of the baryon mass or larger, where the dynamic of the bosonic diquarks plays an essential role.

Aside: Remarks on the first order transition

In the light of the comparative plot in Fig. 3.8(a) a few remarks on the nature of the first order transition in mean-field and FRG calculations are in order. In particular, we want to point the reader's attention to the different sign of the slopes of the first order lines, which indicates a qualitative change in the nature of the phase transition in the calculation including fluctuations compared to the mean-field calculation. This slope is described by a generalized Clausius-Clapeyron relation [118], as a consequence of the coinciding pressure in both phases along the phase boundary,

$$\frac{dT}{d\mu} = -\frac{\Delta n}{\Delta s}, \quad (3.72)$$

which relates it to the differences in baryon density Δn and entropy density Δs across the phase boundary. In the zero temperature limit, where $\Delta s \rightarrow 0$, this implies that the first order line has to become perpendicular to the chemical potential axis. This property is satisfied in both cases although it requires a careful analysis of the low temperature regime in the RG setting [119]. There are, however, more differences

3. Quark-Meson-Diquark Models for QCD-like Theories

concerning the nature of the phase transition, which are most clearly investigated in the chiral limit. Here the mean-field calculation shows a transition to Lee-Wick matter, where the chiral condensate drops to zero beyond the first order transition signaling a complete restoration of chiral symmetry. This chiral first order transition is an *order-disorder transition*; baryon density rises across the phase boundary ($\Delta n > 0$) and one expects the same for the entropy density ($\Delta s > 0$) and thus by Eq. (3.72) a negative slope of the first order line in accordance with Fig. 3.8(a). Note that there is no general principle which constrains the location of the first order transition. In particular, it may well occur at chemical potentials larger than the quark mass as can for example be observed in Fig. 3.8(a), where $m_q \approx 2.64m_\pi$.

The picture is changed by the inclusion of collective mesonic fluctuations. At very small temperatures the RG calculation shows an additional second order transition beyond the first order transition [120], which turns into a crossover for finite quark masses. The order parameter assumes a finite value between the two transitions and complete restoration of chiral symmetry occurs only beyond the second order transition. Hence from the investigations in the chiral limit one has to conclude that the first order line observed in the RG calculation in Fig. 3.8(a) does *not* correspond to the chiral transition. One possible interpretation of the first order line was put forward in [120] as a *liquid gas transition* to bound quark matter. The difference between the constituent quark mass m_q and the critical quark chemical potential could then be interpreted as binding energy of bound quark matter, which would thus require the first order transition to occur below the constituent quark mass. At a liquid gas transition the baryon density rises ($\Delta n > 0$) but in the conventional picture the entropy density rises¹⁴ as well ($\Delta s > 0$), which would again yield a negative slope. However, there is no general argument which contradicts the interpretation of the first order transition in Fig. 3.8(a) as a liquid gas transition. Regardless of its interpretation, the first order transition marks the transition to a phase characterized by a nonvanishing quark density and partially restored chiral symmetry (even in the chiral limit) and by a decrease in entropy density compared to the hadronic phase.

3.4.3. Pion pole mass

Before the discussion of the full phase diagram we come back to the issue of the pion pole mass again. Here we employ the formalism from Section 2.2, which can be extended straightforwardly to include fermionic degrees of freedom, but restrict ourselves for simplicity to the vacuum case $T = \mu = 0$. The flow equations for the mesonic 2-point functions are represented diagrammatically in Fig. 3.9. As additional

¹⁴Note that the entropy per particle decreases from the gaseous to the liquid phase whereas the number density increases. Thus, the sign of the change in entropy density Δs depends on the relative size of the ratio of entropies per particle and the ratio of the corresponding number densities and can thus take, in principle, both signs. The conventional case corresponds to the situation where the entropy density increases from the gaseous to the liquid phase.

input we employ the constant quark-meson 3-point vertices

$$\Gamma_0^{(2,1)} = h, \quad \Gamma_{j \neq 0}^{(2,1)} = ih\gamma^5 \tau_j, \quad \Gamma_{ij}^{(2,2)} = 0. \quad (3.73)$$

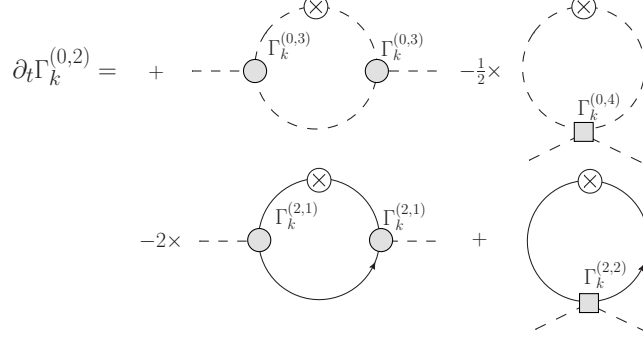


Figure 3.9.: Flow of the mesonic 2-point functions in a quark-meson model. Crossed circles represent regulator insertions $\partial_t R_k$. Solid (dashed) lines represent full fermionic (bosonic) propagators.

The flow equation for the pion 2-point function for an $O(N)$ model coupled to N_f quarks with N_c colors, where this is possible, is then obtained analogously to the purely bosonic case and reads for external (Minkowskian) frequency ω and vanishing spatial external momentum

$$\begin{aligned} \partial_t \Gamma_{k,\pi\pi}^{(0,2)}(\omega) = \frac{k^5}{6\pi^2} \left(-\frac{(N+1)U_k''}{E_k^{\pi^3}} + \frac{2U_k''(E_k^{\sigma^2} - E_k^{\pi^2})((E_k^{\sigma} + E_k^{\pi})^3(E_k^{\pi^2} + E_k^{\sigma}E_k^{\pi} + E_k^{\sigma^2}) - (E_k^{\sigma^3} + E_k^{\pi^3})\omega^2)}{E_k^{\pi^3}E_k^{\sigma^3}((E_k^{\pi} + E_k^{\sigma})^2 - \omega^2)^2} \right. \\ \left. - \frac{U_k'' + 2\phi^2 U_k^{(3)}}{E_k^{\sigma^3}} + \frac{8N_f N_c h^2 (4\epsilon_k^2 + \omega^2)}{\epsilon_k (4\epsilon_k^2 - \omega^2)^2} \right). \end{aligned} \quad (3.74)$$

Here one easily identifies the first three terms as the zero temperature limit of the expression obtained for the purely bosonic model in Eq. (2.30). As in the purely bosonic case one can easily convince oneself of the consistency of the flow equation in the limit of a vanishing external momentum, $\omega = 0$, with the flow equation for the effective potential at $T = \mu = 0$ in the sense that $\partial_t \Gamma_{k,\pi\pi}^{(0,2)}(\omega = 0) = 2 \frac{\partial}{\partial \phi^2} \partial_t U_k$.

Completely analogous to the purely bosonic case in Section 2.2, one solves the combined system of flow equations for the effective potential and the 2-point function in dependence of external frequency ω . The numerical results are compiled in Tab. 3.1, where we demonstrate the independence of the results of the employed solution method by comparing solutions from Grid and Taylor methods. The pion masses computed via this procedure then have to be compared to the built-in definition of the physical pion mass via the onset of diquark condensation. Here the UV parameters were chosen to fix the so-defined physical pion mass to a value of $2\mu_c \approx 138$ MeV.

In the light of the discussion of Section 2.2 the reader should be aware of the

3. Quark-Meson-Diquark Models for QCD-like Theories

Quantity	Grid method	Taylor method
f_π	76.0	75.0
$m_{\pi,\text{scr}}$	178.8	180.0
$m_{\sigma,\text{scr}}$	551.7	550.8
$2\mu_c$	137.8	-
$m_{\pi,\text{pole}}$	122.45	122.6
$m_{\pi,\text{pole, ferm. only}}$	124.9	125.0
$m_{\pi,\text{pole, bos. only}}$	171.6	172.6

Table 3.1.: Comparison of RG screening vs. pole masses obtained via grid and Taylor methods [1] ($N = 6, N_c = 2, N_f = 2$); ‘ferm. only’ (‘bos. only’) refers to maintaining only the constant $\omega = 0$ contributions in the bosonic (fermionic) contribution to the flow of the pion 2-point function, Eq. (3.74). All values are given in MeV.

conceptual differences between screening and pole masses, which of course do not have to coincide. While one might expect the difference to be a subleading effect, as it was in the purely bosonic case, it turns out that the difference between the standard pion screening mass and the physical pion mass defined via the onset are as large as 30% here. Whereas the screening mass severely overestimates the pion mass, the pion pole mass obtained from the flow of the 2-point function tends to underestimate the physical pion mass by about 11%, which represents at least a considerable improvement compared to the widely used screening mass. It is important to point out that the discrepancy of screening and onset mass is not an effect due to the simplicity of the truncation although its size will be truncation-dependent. For example, the inclusion of a (momentum-independent) wavefunction renormalization factor will most likely decrease the discrepancy but cannot fully resolve it as it only involves information about the 2-point function around zero external momentum. In general one should expect an improvement with increasingly refined momentum structures of the truncations. This could for example be realized in an iterative procedure where the result for the 2-point function is eventually fed back into the flow equation for the effective potential and vice versa. In this sense our result for the pion pole mass agrees surprisingly well with the physical pion mass defined via the onset since it only represents the first step in this procedure.

One can investigate the influence of bosonic (fermionic) degrees of freedom separately by setting the external momentum $\omega = 0$ for the corresponding fermionic (bosonic) contributions to the flow in Eq. (3.74). Tab. 3.1 illustrates that both contributions tend to decrease the pole mass compared to the screening mass. However, the dominant contribution comes from the fermionic degrees of freedom, which agrees with investigations in purely bosonic models where the difference between screening mass and the physical pion mass turned out to be just a few percent effect [2, 79]. To avoid the impression that the large discrepancy between physical pion mass and the pion screening mass is just a particular feature of 2-color QCD, we studied the

analogous effect for 3-color QCD, where the pion mass can be defined by the critical isospin chemical potential which marks the onset of charged pion condensation, see Chapter 4. For the parameter set from [2] one finds a screening mass $m_{\pi,\text{scr}} = 188.0$ MeV compared to a physical pion mass of $m_{\pi} = 136.6$ MeV representing a, compared to the 2-color case, even larger deviation of 38%. The pion pole mass in this calculation is $m_{\pi,\text{pole}} = 133.0$ MeV, which also underestimates the physical pion mass but by only 3%.

To summarize, the main conclusion of these investigations has to be that the commonly employed procedure of fixing particle masses in model calculations via screening masses, i.e. via the eigenvalues of the Hessian of the effective potential, entails a large systematic error in particular in simple truncations such as the LPA. But secondly, the results of this section demonstrate that the (pion) pole mass in the vacuum can be computed at least approximately using the simple procedure introduced in Section 2.2.

3.4.4. Full phase diagram

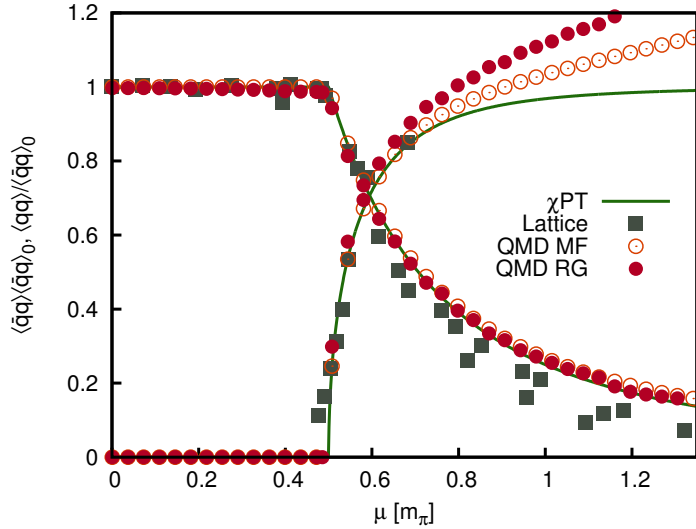


Figure 3.10.: Condensates at $T = 0$ [1] (lattice data from [84]).

As in the mean-field case we start our discussion of the full phase diagram as obtained from the RG calculation with the zero temperature condensates shown in Fig. 3.10, where one observes a nice agreement between QMD model results and other approaches to 2-color QCD. The phase diagram from the full RG calculation involving an effective potential parametrized by two invariants $U_k = U_k(\rho^2, d^2)$ compared to the one-dimensional $SO(6)$ symmetric flow as shown in Fig. 3.11 represents one of the most important results of this thesis. Again it clearly demonstrates the impact of the competing dynamics of mesonic and baryonic degrees of freedom. One observes that

3. Quark-Meson-Diquark Models for QCD-like Theories

the chiral crossover lines of the two calculations coincide at zero chemical potential, which is just a result of the enlarged $SO(6)$ symmetry. The fact that they only slightly deviate for small chemical potentials is then to be understood as an approximate $SO(6)$ symmetry of the effective potential. As remarked above the two only coincide exactly for $\mu = 0$ which means that there are μ -induced effects on the effective potential, requiring it to be a genuine function of two invariants despite the fact that the diquark condensate does not acquire an expectation value outside the condensation phase. If one increases the chemical potential beyond the critical value μ_c for diquark condensation the rapidly rising baryon density eventually suppresses the chiral condensate leading to an asymptotic restoration of chiral symmetry at asymptotically large chemical potentials. The main conclusion from the mean-field analysis remains valid here: The collective baryonic degrees of freedom lead to a complete disappearance of the critical endpoint observed in the $SO(6)$ symmetric calculation.

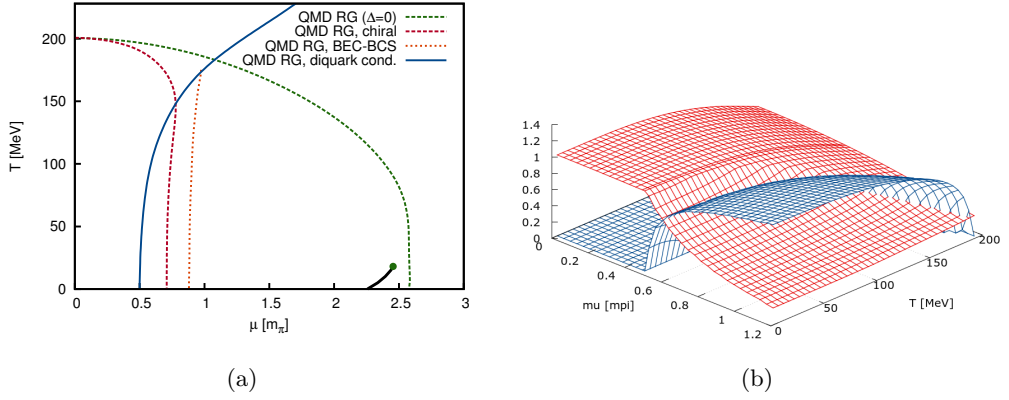


Figure 3.11.: Full QMD model phase diagram:

- (a) Phase diagram from RG calculation with (red/blue)/without (green) collective baryonic fluctuations; dashed red: chiral crossover (half-value of the condensate); solid blue: second order transition (diquark condensation); thick solid black: first order transition; dashed orange: BEC-BCS crossover.
- (b) Phase diagram from RG calculation: normalized chiral condensate $\langle \bar{q}q \rangle / \langle \bar{q}q \rangle_0$ (red) and diquark condensate $\langle qq \rangle / \langle \bar{q}q \rangle_0$ (blue) as function of temperature and chemical potential.

The phase diagram from the RG calculation agrees qualitatively with the corresponding QMD model mean-field calculation, see Fig. 3.5, but only up to one important exception. In the RG calculation the diquark condensation phase boundary stays second order throughout the whole investigated parameter range, which resembles in this respect closely the NJL calculation, whereas the QMD model mean-field calculation shows a tricritical point in the phase diagram. As argued above, there are strong indications that the occurrence of the tricritical point is closely related to thermal UV contributions, which require an improved treatment of the high temperature range in the RG calculation. This will be discussed as an outlook in Section 3.5.2.

BEC-BCS crossover

As already alluded to in the introduction, the phase diagram of 2-color QCD shows a BEC-BCS crossover as an additional feature in the diquark condensation phase. Such a BEC-BCS crossover can be understood in a field-theoretical context in terms of the rotation of the spontaneously generated Dirac mass into a Majorana mass [121]. For small chemical potentials the quark mass is given predominantly by a spontaneously generated Dirac mass and with the onset of superfluidity Bose-Einstein condensation of the bosonic baryons sets in forming a dilute gas of strongly bound diquark molecules. The quarks' Dirac mass $g\rho$ decreases with increasing chemical potential and rotates into a Dirac mass gd . For large chemical potentials there is BCS pairing, where the diquarks pair in the form of spatially delocalized Cooper pairs.

In ultracold atoms the BEC-BCS crossover is identified via the s-wave fermion-fermion scattering length which is positive in the BEC regime and negative in the BCS regime [85, 86]. Analogously one might try to characterize the BEC-BCS in the relativistic system via the s-wave quark-quark scattering length. Although this quantity is not experimentally accessible in the related problem of QCD with isospin chemical potential, it remains an important project for the future which would help to strengthen the analogies to the BEC-BCS crossover in ultracold atoms. In the following we employ a different approach where we identify the BEC-BCS crossover via the value of the chemical potential for which the minimum of the dispersion relation $E_p^-(\vec{p}^2)$ occurs at a nonvanishing spatial momentum. Employing Eq. (3.41) this amounts to identifying the BEC-BCS crossover via the line for which the quarks' Dirac-mass $m_q = g\rho$ becomes equal to the chemical potential, i.e. $\mu = m_q$, see [122] for a comprehensive discussion of the BEC-BCS crossover within the NJL model. Fig. 3.11 includes a crossover line as defined above to estimate the location of the BEC-BCS crossover inside the diquark condensation phase.

3.5 Outlook: Extensions of the QMD Model for QC_2D

In this section we discuss three possible extensions of the QMD model calculation presented in the previous section. The first concerns the impact of perturbative UV contributions. The second deals with the inclusion of gauge degrees of freedom into the calculation which are the essential missing degrees of freedom towards a proper effective description of 2-color QCD. And finally in the third outlook, we discuss an improved truncation for the QMD model as a first step of a calculation, which goes beyond the zeroth order in the derivative expansion.

3.5.1. Perturbative UV contributions

Note that given a temperature-independent microscopic action in the UV, one can only expect to obtain cutoff-independent results if the UV cutoff scale Λ_{UV} is much larger than the typical scale $2\pi T$ where the temperature-dependence of the flow starts to set in. This severely restricts the accessible temperature range for a given fixed UV scale.

3. Quark-Meson-Diquark Models for QCD-like Theories

One obvious solution to gain access to the high temperature regime would simply be to increase the UV scale, which is in an effective model approach, however, only possible up to a certain point. Alternatively, if one wants to extend the accessible temperature range for a given fixed UV scale, one can correct for the missing contributions from high momentum modes by combining the FRG with perturbative results. Here this is achieved by adding the quark flow in a given Polyakov loop background [123] integrated from $k = \infty$ to $k = \Lambda_{UV}$ for which the flow equation reads

$$\partial_t U_{q,k} = -\frac{k^5}{12\pi^2} \sum_{\pm} \frac{8}{E_k^{\pm}} \left(1 \pm \frac{\mu}{\epsilon_k}\right) (-2N_q(E_k^{\pm}; T, \Phi)), \quad (3.75)$$

where a temperature-independent UV divergent contribution was discarded. The approach employed in the literature is to add this perturbative UV contribution to the effective potential obtained by integrating the corresponding full flow equation from $k = \Lambda_{UV}$ to $k = 0$. If one decides to keep just the contribution for massless quarks, as it was done in [123, 113, 114], the procedure just represents a field-independent shift of the effective potential and thus in the pressure which then ensures thermodynamic consistency with the Stefan Boltzmann limit. However, if one decides to keep the field-dependent UV contribution from Eq. (3.75) in order to account for fluctuations in the UV contributions, these will not only influence the thermodynamics but can also impact the phase structure. The additional UV contributions should then be added to the initial UV potential before integrating the flow equation from $k = \Lambda_{UV}$ to $k = 0$, thereby giving rise to a temperature and chemical potential dependence of the initial conditions in the UV which properly accounts for the thermodynamics of the UV microscopic action. Fig. 3.12 illustrates the effect of perturbative UV

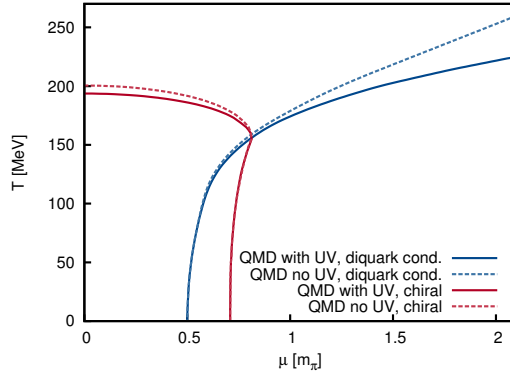


Figure 3.12.: Comparing the impact of perturbative UV contributions on the QMD model phase diagram.

contributions by comparing the QMD model phase diagram with and without UV contributions. Their inclusion shifts both the chiral crossover line and the diquark condensation phase boundary to smaller temperatures whereas the low temperature

3.5. Outlook: Extensions of the QMD Model for QC₂D

regime of the phase diagram remains unchanged. In distinction to the mean-field analysis where the inclusion of the full thermal contributions lead to the appearance of a tricritical point on the diquark condensation phase boundary the phase boundary in the RG calculation in Fig. 3.12 remains second order throughout the whole investigated parameter range. This question of the appearance of a tricritical point is a particularly interesting question since it was not only predicted by effective model approaches but also observed in 4-flavor lattice simulations [124].

3.5.2. PQMD model for QC₂D

In this section we present an outlook to the inclusion of gauge degrees of freedom into the quark-meson diquark model. As described in Section 3.2.2 these can be modeled via a constant background gauge field A_0 and a corresponding Polyakov loop potential $\mathcal{U}_{\text{Pol}}(A_0)$. While one should employ Polyakov loop potentials from the lattice or from functional methods calculation in future studies we present results for the potential [98]

$$\mathcal{U}_{\text{Pol}}(\Phi; T, T_0) = -bT[24\Phi^2 e^{-a/T} + \log(1 - \Phi^2)], \quad (3.76)$$

which is the 2-color variant of the commonly used 3-color logarithmic Polyakov loop potential [30, 125], which is in turn based on a lattice strong coupling expansion. This calculation can be expected to reach the same quantitative level as the corresponding calculations for the 3-color case [113, 114, 112]. Similar to these approaches the Polyakov loop will be treated as a background mean-field, i.e. the flow is evaluated for different choices of Φ and the resulting full effective potential $U_{\text{QC}_2\text{D}}(\rho^2, d^2, \Phi)$ after the integration of the flow is then minimized with respect to all three variables.

The deconfinement transition itself is fixed by the parameter a which is related to the critical temperature T_0 as $a = T_0 \log 24$, whereas a strong coupling expansion relates b to the string tension $\sqrt{\sigma}$ via $b = (\sigma/a)^3$. The parameter b determines the mixing between the chiral and the deconfinement phase transition and can be used to adjust the relative sizes of the (pseudo-)critical temperatures for the chiral and the deconfinement phase transition and is typically chosen such that the two crossovers coincide [30]. Here we will, however, simply choose $b = (\sigma/a)^3$ in order to be able to account for an adjusted T_0 as described below. As pointed out in [99], the backreaction of the matter sector on the glue sector can be taken into account via an adjusted critical temperature T_0 which enters the Polyakov loop potential. Therefore one defines

$$T_0(\mu; N_c, N_f) = T_\tau e^{-\frac{1}{\alpha_0 b(\mu)}}, \quad (3.77)$$

where the value of the strong coupling constant α_0 has been fixed to its value at a reference scale here chosen in analogy to the 3-color case as $T_\tau = 1776$ MeV and

$$b(\mu) = \frac{1}{6\pi} (11N_c - 2N_f) - b_\mu \frac{\mu^2}{T_\tau^2}. \quad (3.78)$$

The first term is identified as coefficient of the QCD 1-loop β -function with N_f

3. Quark-Meson-Diquark Models for QCD-like Theories

massless quarks. The form of the μ -dependent second term is motivated by the expression for the effective charge obtained from a perturbative hard thermal loop calculation [99, 73]. The coefficient b_μ is fixed such that the chiral and deconfinement transitions coincide at some nonvanishing chemical potential, which was found to be the case for $b_\mu \simeq \frac{16}{\pi} N_f$ [99]. For this choice it will then turn out that the two transitions coincide along the whole phase boundary. If we keep the reference scale T_τ , reproducing the pure-gauge lattice result for the critical temperature $T_c/\sqrt{\sigma} = 0.7091(36)$ [126] corresponding to $T_0(0; 2, 0) = 312.0$ MeV in physical units for $\sqrt{\sigma} = 440$ MeV fixes the strong coupling constant $\alpha_0 = 0.4927$ at the reference scale T_τ . Eq. (3.77) then yields $T_0(0; 2, 2) = 212.0$ MeV for $N_f = 2$ massless flavors at vanishing chemical potential.

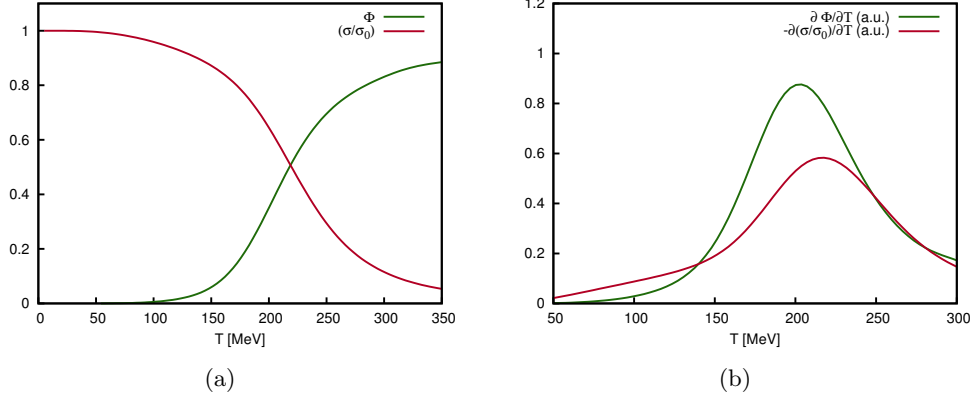


Figure 3.13.: PQMD model at $\mu = 0$. Polyakov loop and normalized chiral condensate (a) and the corresponding temperature derivatives (b) as function of temperature.

In the following we present first preliminary results on the phase structure of the PQMD model, which are mainly supposed to serve as a proof of concept at this point. Fig. 3.13 shows the temperature-dependent Polyakov loop and chiral condensate at vanishing chemical potential. Here perturbative UV contributions were taken into account as described in the previous section. In order to compare the relative occurrence of the chiral and deconfinement crossover one requires an appropriate crossover definition. One consistent choice would be to consider peaks in the corresponding susceptibilities which can be extracted from the curvature of the effective potential at its minimum. Here we employ a different criterion which can be directly extracted from the order parameter and which involves defining the crossover via the peak in the temperature derivative of the order parameter [99]. Employing this definition, Fig. 3.13(b) demonstrates that the two transitions occur in a common narrow temperature range at vanishing chemical potential. This yields crossover temperatures of 213 MeV and 198 MeV for the chiral and the deconfinement crossover respectively. These values should be taken with care as predictions due to their dependence on the sigma mass but they lie in a temperature range comparable to the recent lattice result

3.5. Outlook: Extensions of the QMD Model for QC_2D

of 217(23) MeV for the deconfinement crossover temperature [127] which was, however, obtained from simulations with considerably larger quark masses. As in the 3-color case there is also a systematic error due the simple 1-loop perturbative estimate of $T_0(N_f)$. Furthermore one should keep in mind that the crossover temperature depends significantly on the definition employed to define the crossover as exemplified by the half-value and the inflection point criteria in Fig. 3.14.

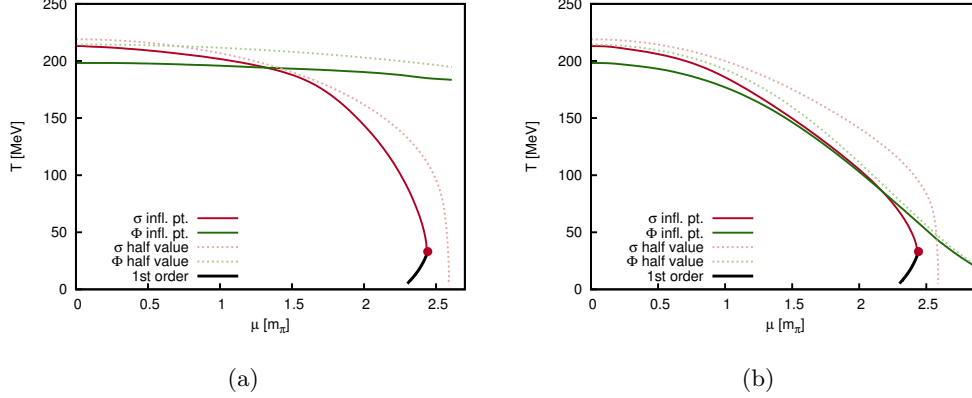


Figure 3.14.: PQMD model with $SO(6)$ symmetric potential without (a)/with (b) μ -dependent matter backcoupling; solid red: chiral crossover (inflection point); dashed red: chiral crossover (half-value); solid green: deconfinement crossover (inflection point); dashed green: deconfinement crossover (half-value); thick solid: first order transition.

Turning to finite chemical potential, we start analogous to Section 3.4.2 by considering the $SO(6)$ symmetric case for which the flow equation for the effective potential is given in Eq. (3.69). Here we investigate, in particular, the effect of the μ -dependent matter-backcoupling on the gauge sector, which is achieved by a nonvanishing coefficient b_μ as described above. Its effect can be inferred from the phase diagrams in Fig. 3.14 and is in many aspects similar to what is observed in the corresponding 3-color calculations [112, 128]. Including the term leads to nearly coinciding crossover lines down to temperatures of about 70 MeV. Unlike in the 3-color calculation, below this temperature the deconfinement transition does not follow the bending of the chiral transition line towards the critical endpoint. At the same time, with increasing chemical potential, the deconfinement crossover gets increasingly rapid but remains a continuous transition throughout the whole investigated parameter range. In the scenario with a constant T_0 , i.e. $b_\mu = 0$, the two transitions only coincide for small chemical potentials. The deconfinement crossover temperature decreases only slightly with increasing chemical potential and stays essentially uninfluenced by the chiral transition. Note that in distinction to the 3-color case the phase diagrams in both scenarios show quarkyonic phases of deconfined but chirally restored matter although their size and location differs considerably in the two scenarios.

As before, the results of the calculation involving the $SO(6)$ symmetric effective

3. Quark-Meson-Diquark Models for QCD-like Theories

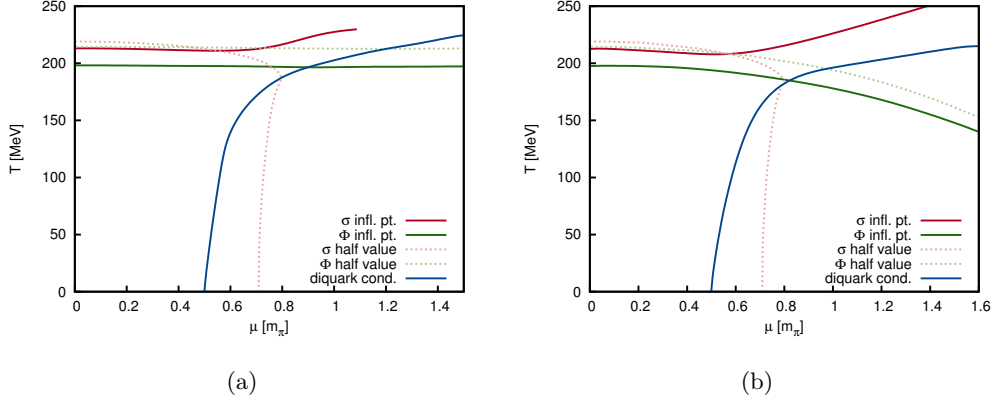


Figure 3.15.: PQMD model phase diagrams without (a)/with (b) μ -dependent matter backcoupling; solid red: chiral crossover (inflection point); dashed red: chiral crossover (half-value); solid blue: second order transition (diquark condensation); solid green: deconfinement crossover (inflection point); dashed green: deconfinement crossover (half-value).

potential are of course not relevant for the description of 2-color QCD because of the improper treatment of the diquark degrees of freedom but mimic again the corresponding 3-color PQM model calculations and serve as crosscheck in particular for the inclusion of the matter backcoupling. At this point we reiterate the importance of baryonic degrees of freedom for the phase diagram. These are properly taken into account in the calculation with the $SO(4) \times SO(2)$ symmetric effective potential for which the corresponding flow equation is given in Eq. (3.68). Again we compare two scenarios with and without μ -dependent matter backcoupling. The phase diagram of the calculation without μ -dependent backcoupling, as shown in Fig. 3.15(a), shows only a very slight μ -dependence at large chemical potentials which reflects itself in nearly constant deconfinement transition temperatures. This result is comparable to the phase diagram obtained from a PNJL calculation [98] without matter backcoupling on the gauge sector. This should be contrasted with the PQMD phase diagram including a μ -dependent matter backcoupling shown in Fig. 3.15(b), where the deconfinement transition line bends down inside the diquark condensation phase. The resulting phase diagram is in qualitative agreement with recent lattice investigations [127]. Here the phase structure at large chemical potentials is particularly interesting as lattice investigations indicate the existence of a quarkyonic phase [129]. Unfortunately, if the chiral condensate decreases $\sim \mu^{-2}$, as predicted by chiral perturbation theory, it is difficult to quantify deviations from the standard scenario at large chemical potentials which would be required in order to analyze the fate of chiral symmetry in this region of the phase diagram.

3.5.3. Improved truncation for the QMD model

Coming back to the QMD model without a coupling to a background gauge field, we present an outlook on an improved truncations for the effective average action which are required to check the reliability of the results of the previous sections which were obtained within the zeroth order derivative expansion from Eq. (3.67). Despite the simplicity of the truncation one should, however, keep in mind that the employed solution method via the grid method discussed in Section 2.1.4 captures in principle the full effective potential and thus arbitrary high interaction terms in the fields and goes in this sense beyond the widely used Taylor solution techniques which remain by construction restricted to a fixed expansion order. Nevertheless, in order to reach a higher quantitative level in the description and, in particular, also to investigate the effects of the breaking of the enlarged $SU(4)$ flavor symmetry on the level of the interaction terms, one should also consider improved truncations.

The next step in the derivative expansion involves the inclusion of running wavefunction renormalization factors and Yukawa couplings, which could in the simplest case just be chosen as scale-dependent. In the light of the discussion of Section 3.4.1 the most general Ansatz¹⁵ for the effective action of this kind without taking into account higher order terms from the derivative expansion should involve a fermionic wave function renormalization factor (Z_ψ) and bosonic wave function renormalization factors for both the mesons (Z_r) and the diquarks (Z_d) but also two Yukawa couplings for mesons (h_r) and diquarks (h_d) reflecting the possibility of breaking the $SO(6)$ symmetry at the level of the interaction terms. Note that the two bosonic wavefunction renormalization factors and the two Yukawa couplings are required to coincide at zero chemical potential by $SO(6)$ symmetry, which reduces to an $SO(4) \times SO(2)$ symmetry at nonvanishing chemical potential. The Ansatz for the effective average action reads in terms of unrenormalized fields $\tilde{\psi}$ and $\tilde{\phi}_i$:

$$\Gamma_k = \int_x \tilde{\psi} (Z_\psi (\not{\partial} - \mu\gamma^0) + \tilde{h}_r (\tilde{\sigma} - i\gamma^5 \vec{\pi} \vec{\tau})) \tilde{\psi} + \frac{\tilde{h}_d}{2} \left(\tilde{\Delta}^* (\tilde{\psi}^T C \gamma^5 \tau_2 i S \tilde{\psi}) + \tilde{\Delta} (\tilde{\psi}^\dagger C \gamma^5 \tau_2 i S \tilde{\psi}^*) \right) + \frac{1}{2} (\partial_\mu \tilde{\sigma})^2 + \frac{1}{2} (\partial_\mu \vec{\pi})^2 + \frac{1}{2} Z_d ((\partial_\mu - 2\mu \delta_\mu^0) \tilde{\Delta}) (\partial_\mu + 2\mu \delta_\mu^0) \tilde{\Delta}^* + U_k(\tilde{\rho}^2, \tilde{d}^2) \quad (3.79)$$

Defining $\tilde{\Delta} = \tilde{\Delta}_R + i\tilde{\Delta}_I$, it reads in momentum space in terms of the spinor variables

¹⁵We emphasize again that the effective action is less constrained at finite temperature where one should for example distinguish wavefunction renormalization factors parallel and perpendicular to the heatbath similar to [110].

3. Quark-Meson-Diquark Models for QCD-like Theories

from Eq. (3.28)

$$\begin{aligned}
\Gamma_k = & \int_{p,q} \bar{\tilde{\Psi}}(p) \left(\begin{array}{cc} Z_\psi(i\not{p}-\mu\gamma^0)\delta(p-q)+\tilde{h}_r(\tilde{\sigma}+i\gamma^5\tilde{\tau}\tilde{\pi})(p-q) & \tilde{h}_d\tilde{\gamma}^5(\tilde{\Delta}_R(p-q)+i\tilde{\Delta}_I(p-q)) \\ -\tilde{h}_d\tilde{\gamma}^5(\tilde{\Delta}_R(p-q)-i\tilde{\Delta}_I(p-q)) & Z_\psi(i\not{p}+\mu\gamma^0)\delta(p-q)+\tilde{h}_r(\tilde{\sigma}-i\gamma^5\tilde{\tau}\tilde{\pi})(p-q) \end{array} \right) \tilde{\Psi}(q) \\
& + \frac{1}{2}Z_r \int_p p^2 \tilde{\sigma}(-p)\tilde{\sigma}(p) + p^2 \tilde{\pi}_i(-p)\tilde{\pi}_i(p) + \int_x U_k(\tilde{\rho}^2, \tilde{d}^2) \\
& + \frac{1}{2}Z_d \int_p p^2 \left(\tilde{\Delta}_R(-p)\tilde{\Delta}_R(p) + \tilde{\Delta}_I(-p)\tilde{\Delta}_I(p) \right) - 4p_0\mu\tilde{\Delta}_R(-p)\tilde{\Delta}_I(p) - 2\mu^2|\tilde{\Delta}|^2.
\end{aligned} \tag{3.80}$$

The flow equation for the effective potential can be derived as before, see Appendix D.2 by evaluating the flow equation for a constant field configuration. The flow equations for the anomalous dimensions and the Yukawa couplings require appropriate projections of the flow equations for the 2-point and 3-point functions respectively. The corresponding flow equations and a sketch of their derivation are given in Appendix D.3 and remain to be solved numerically in the future.

4

QCD with Isospin Chemical Potential

This final chapter in the first part of the thesis is devoted to QCD with isospin chemical potential, which, from the viewpoint of chiral effective models, turns out to be closely related to previously discussed 2-color QCD. Isospin chemical potential induces an imbalance of up and down quarks via different chemical potentials. Although the Dirac operator does not possess an antiunitary symmetry in this case, corresponding to a Dyson index $\beta = 2$, the theory is nevertheless free of a fermion sign for vanishing quark chemical potential.

Apart from this rather academic interest, there is even a direct physical motivation for the study of QCD with isospin chemical potential. An isospin imbalance is for example realized in neutron stars or heavy-ion experiments although one has to bear in mind that the relevant regions of the phase diagram are not only characterized by an isospin imbalance but also by large baryon chemical potentials for which the reliability of predictions of the quark-meson models for the QCD phase diagram are questionable due to the lack of baryonic degrees of freedom in the models. Nevertheless we map out the phase diagram for the full range of baryon chemical potentials to gain an understanding of the possible structures, which can arise in such phase diagrams.

Finally, the consideration of both isospin and quark chemical potential allows to study the competing interplay of imbalances of up and down quarks, as induced by isospin chemical potential, and quarks and anti-quarks, as induced by quark chemical potential, at the same time. Its impact is particularly interesting to observe on BCS pairing patterns in regions of the phase diagrams where such phases exist. It turns out that the phase diagrams in the (μ, T) plane at fixed, sufficiently large isospin chemical potential beyond the BEC-BCS crossover are closely related to the phase diagrams of polarized Fermi gases. These are ultracold Fermi gases with a population imbalance, and their phase diagrams are studied as function of polarization and temperature. Here we will stress the relation to these non-relativistic cases and address the impact of fluctuations on the corresponding phase diagrams.

4.1 Symmetries and Model Construction

As in the previous chapter we start with a brief review of the symmetries and possible symmetry breaking patterns. These can be analyzed most conveniently analogous to the previous sections, this time employing the spinor variable $\Psi = \begin{pmatrix} \psi_R \\ \psi_L \end{pmatrix}$ separating left- and right-handed components. For definiteness let us consider QCD with $N_c > 2$ colors and N_f flavors in the presence of an isospin chemical potential. The starting point is the usual $SU(N_f)_L \times SU(N_f)_R \times U(1)_B$ chiral/baryon number symmetry at finite quark chemical potential but still zero isospin chemical potential. In the following we will concentrate on the chiral sector as the baryon number symmetry always remains unbroken. As usual, an explicit/dynamically generated quark mass m breaks $SU(N_f)_L \times SU(N_f)_R \rightarrow SU(N_f)_V$. On the other hand a finite isospin chemical potential μ_I explicitly breaks $SU(N_f)_L \times SU(N_f)_R \rightarrow U(1)_L^{(3)} \times U(1)_R^{(3)}$, where $U(1)_L^{(3)}$ ($U(1)_R^{(3)}$) correspond to rotations of left-(right-) handed quarks generated by T_3 . As before if both $\mu_I > 0$ and $m > 0$, the remaining symmetry is just given by the common subgroup $U(1)_V^{(3)}$. A nonvanishing charged pion condensate $\langle \pi^+ \pi^- \rangle$, defining $\pi^\pm = \pm i\pi_1 - \pi_2$, spontaneously breaks it down to its discrete subgroup Z_2 . Again the asymptotic symmetry in the pion condensation phase, $U(1)_A^{(3)}$ allowing rotations in the neutral pion and sigma meson subspace, can be identified by considering the chiral limit. The symmetry breaking patterns are summarized in Fig. 4.1.

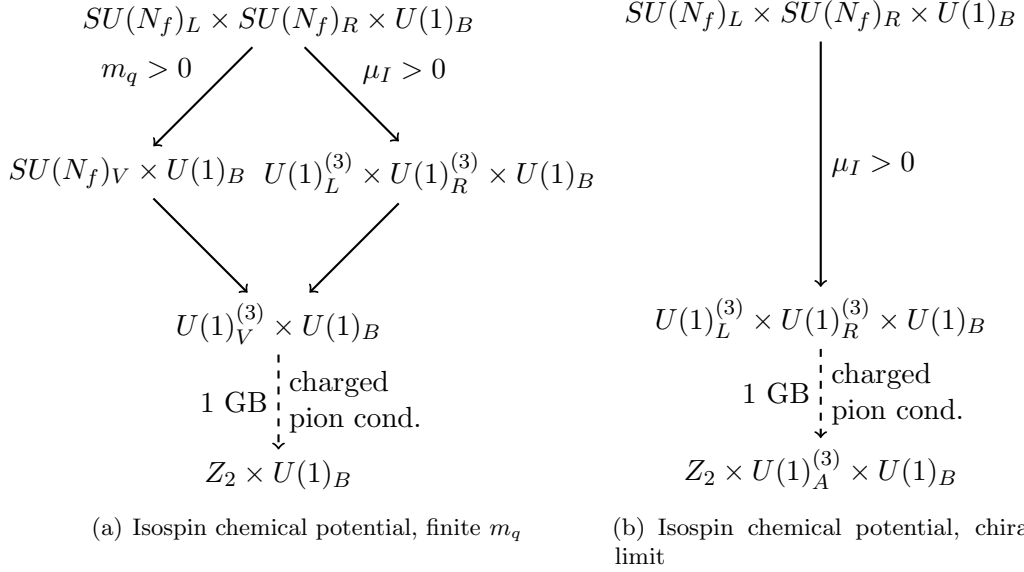


Figure 4.1.: Patterns of symmetry breaking in QCD with isospin chemical for finite quark masses and in the chiral limit.

This pattern of symmetry breaking can be realized within a quark-meson model as chiral effective model. Therefore, one starts from the usual quark-meson model

4.2. Phase Diagram of QCD with Isospin Chemical Potential

in presence of only quark chemical potential and introduces isospin analogous to Eq. (3.25) this time replacing the quark number current by the current associated to isospin rotations. The corresponding Lagrangian can be written in basis of up- and down-quarks, therefore defining $\Psi = \begin{pmatrix} \psi_u \\ \psi_d \end{pmatrix}$, as

$$\begin{aligned} \mathcal{L}_{QM+\mu_I} = & \Psi S_0^{-1} \bar{\Psi} + \frac{1}{2}(\partial_\mu \sigma)^2 + \frac{1}{2}(\partial_\mu \pi_0)^2 + U(\rho^2, d^2) - c\sigma \\ & + \frac{1}{2}((\partial_\mu - 2\mu_I \delta_\mu^0)\pi_+ + (\partial_\mu + 2\mu_I \delta_\mu^0)\pi_-), \end{aligned} \quad (4.1)$$

where $\rho^2 = \sigma^2 + \pi_0^2$, $d^2 = \pi_+ \pi_-$ and

$$S_0^{-1} = \begin{pmatrix} \not{\partial} + h(\sigma + i\gamma^5 \pi_3) - (\mu + \mu_I)\gamma_0 & g\gamma^5 \pi_+ \\ -g\gamma^5 \pi_- & \not{\partial} + h(\sigma - i\gamma^5 \pi_3) - (\mu - \mu_I)\gamma_0 \end{pmatrix}. \quad (4.2)$$

This expression should be compared to the corresponding expression for 2-color QCD given in Eq. (3.29), which was obtained by rewriting the QMD Lagrangian in terms of red and charge-conjugated green quarks using the spinor variable $\Psi = \begin{pmatrix} \psi_r \\ \tau_2 \psi_g^C \end{pmatrix}$ instead of $\Psi = \begin{pmatrix} \psi_u \\ \psi_d \end{pmatrix}$ as above. Comparing the two expressions, it is obvious that the quark-meson model for 3-color QCD with isospin chemical potential at $\mu = 0$ can be mapped to the corresponding quark-meson-diquark model for 2-color QCD with the following identifications: One identifies charged pions π_+/π_- with the diquark fields Δ/Δ^* and the neutral pion π_0 with the isovector of three neutral pions $\vec{\pi}$ in 2-color QCD. Isospin chemical potential μ_I maps to quark chemical potential μ in 2-color QCD. This identification is of course only valid for the matter sectors as the gauge sectors in both theories are fundamentally different.

4.2 Phase Diagram of QCD with Isospin Chemical Potential

In this section we present results on different aspects of the phase diagram of QCD with isospin chemical potential in dependence of both isospin and quark chemical potential as obtained from the quark-meson model introduced in the previous section in an FRG approach again truncating the effective average action at zeroth order in the derivative expansion. We start by discussing aspects of the zero temperature phase diagram before turning to the three-dimensional phase diagram as function of temperature, isospin chemical potential and quark chemical potential and finally discussing the relation to imbalanced Fermi gases.

4.2.1. Flow equation for the effective potential

The flow equation for the effective potential in a zeroth order derivative expansion with quark and isospin chemical potential but here without coupling to a background

4. QCD with Isospin Chemical Potential

gauge field A_0 is derived analogously to Eq. (3.68) and reads

$$\partial_t U_k = \frac{k^5}{12\pi^2} \left\{ \frac{1}{E_k^\pi} \coth\left(\frac{E_k^\pi}{2T}\right) + \sum_{i=1}^3 \frac{3z_i^4 - \alpha_1 z_i^2 + \alpha_0}{(z_{i+1}^2 - z_i^2)(z_{i+2}^2 - z_i^2)} \frac{1}{z_i} \coth\left(\frac{z_i}{2T}\right) - \sum_{\pm} \frac{2N_c}{E_k^\pm} \left(1 \pm \frac{\mu_I}{\epsilon_k}\right) \left(\tanh\left(\frac{E_k^\pm + \mu}{2T}\right) + \tanh\left(\frac{E_k^\pm - \mu}{2T}\right)\right) \right\}, \quad (4.3)$$

with E_k^π , α_i , z_i and E_k^\pm as defined below Eq. (3.68) up to the substitution $\mu \rightarrow \mu_I$. For vanishing quark chemical potential μ the equivalence of the isospin and the 2-color case reflects itself of course also on the level of the flow equation, which coincides with Eq. (3.68) up to numerical factors.

4.2.2. Zero-temperature results

Zero-temperature phase diagram and the Silver Blaze property

It is interesting to consider the zero-temperature phase diagram as it is strongly constrained by the Silver Blaze property. This is a consequence of the fact that different degrees of freedom couple to different combinations of quark and isospin chemical potential. Up- and down quarks couple to the combinations $\mu_u = \mu + \mu_I$ and $\mu_d = \mu - \mu_I$ respectively, whereas charged pions couple just to isospin chemical potential μ_I . The Silver Blaze property now implies that the partition function and hence all thermodynamic observables have to remain independent of μ and μ_I in a quadrilateral area of the zero-temperature phase diagram defined by $\mu + \mu_I < m_q$ and $\mu_I < m_\pi/2$, where m_q and m_π designate quark and pion masses in the vacuum. Crossing the top boundary of this area, which we will refer to as *first Silver Blaze region* in the following, enables the excitation of up-quarks whereas crossing its right border allows to excite charged pions thereby marking the onset of charged pion condensation. Further constraints from the Silver Blaze property arise inside the pion condensation phase. For $\mu_I > m_\pi/2$ the thermodynamic potential obviously becomes μ_I -dependent. For fixed μ_I , however, it has to remain independent of μ as long as the latter stays smaller than the smallest quark excitation energy. Let us therefore consider the quark dispersion relation

$$E_q^-(\vec{p}^2) = \sqrt{g^2 d^2 + (\sqrt{\vec{p}^2 + g^2 \rho^2} - \mu_I)^2}, \quad (4.4)$$

which is for $\mu_I < g\rho$ minimized by $\vec{p} = 0$ yielding a minimal energy $E_{\min}^- = m_q^-(\mu_I) = \sqrt{g^2 d^2 + (g\rho - \mu_I)^2}$. For $\mu_I > g\rho$, which corresponds to the BCS regime according to Section 3.4.4, it becomes energetically favorable to excite quarks with a finite spatial momentum $\vec{p}^2 = \mu_I^2 - g^2 \rho^2$ and a minimal energy $E_{\min}^- = gd$, which hints at the occurrence of inhomogeneous phases at large isospin chemical potentials such as FFLO phases discussed for example for 2-color QCD with isospin chemical potential [106, 130]. The impact of inhomogeneous phases on the phase diagram of QCD with

4.2. Phase Diagram of QCD with Isospin Chemical Potential

isospin chemical potential should be investigated in detail in the future. The conditions $\mu_I > m_\pi/2$ and $\mu < E_{\min}^-$ thus define the *second Silver Blaze region* where the grand potential is required to remain independent of the quark chemical potential μ by general principles.

Note, however, that these general arguments only hold up to possible first order transitions in these regions, which concerns in particular the possible first order transition at large μ and small μ_I . If such a first order line intersects the first Silver Blaze region, the thermodynamic potential is of course only required to stay independent of chemical potential up the first order line. In any case the first order line cannot end within the first Silver Blaze region as this would correspond to a thermodynamically inconsistent scenario where two phases separated by a first order phase transition are continuously connected within the first Silver Blaze region.

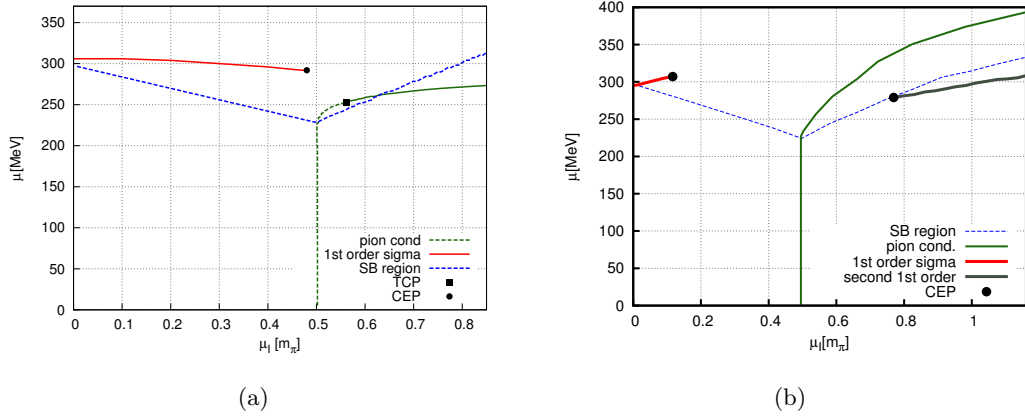


Figure 4.2.: Zero-temperature phase diagrams in the (μ_I, μ) plane [2]:

- (a) from an extended mean-field calculation (only fermionic contributions to the flow),
- (b) from the full FRG calculation.

These general principles are nicely reflected in the numerical results both in the extended mean-field calculation, where only fermionic contributions to the flow of the effective potential are considered, and in the full FRG calculation including both fermionic and bosonic fluctuations. The corresponding zero-temperature phase diagrams are shown in Fig. 4.2. In Fig. 4.2(b) the first order liquid-gas transition line slightly intersects the first Silver Blaze region but the critical endpoint lies outside of it as required by general arguments. The second order transition separating the charged pion condensation from the normal chiral symmetry breaking phase stays constant at $\mu_I = m_\pi/2$ until it hits the boundary line of the first Silver Blaze region at $m_q - m_\pi/2$ and bends towards larger isospin chemical potentials. Unlike the extended mean-field calculation, where the pion condensation phase transition turns first order for large isospin chemical potentials and which correspondingly shows a tricritical point in the phase diagram, see Fig. 4.2(a), the phase transition stays second order throughout the

4. QCD with Isospin Chemical Potential

whole investigated parameter range in the calculation including mesonic fluctuations. The phase diagram from Fig. 4.2(b) shows another interesting feature which was not present at mean-field level namely an additional first order transition inside the pion condensation phase, which ends in a critical endpoint at the boundary of the second Silver Blaze region. The significance of this transition will be discussed in Section 4.2.4.

Isospin density

Before we come to the discussion of the three dimensional phase diagram, we address the question of direct compatibility of our model results to lattice results, which constitutes one of the main motivations for the study of QCD-like theories. We therefore compare the isospin chemical potential dependence of the isospin density $\rho_I = -\frac{\partial \Omega_{GC}}{\partial \mu_I}$ at $T = \mu = 0$ to recent lattice results at finite isospin chemical potential from simulations in the canonical ensemble [131]. Fig. 4.3 shows results from extended mean-field calculations where only fermionic contributions to the flow of the effective potential are considered, the full FRG solution, lattice results as well as the prediction from chiral perturbation theory. Note again that the Silver Blaze property requires

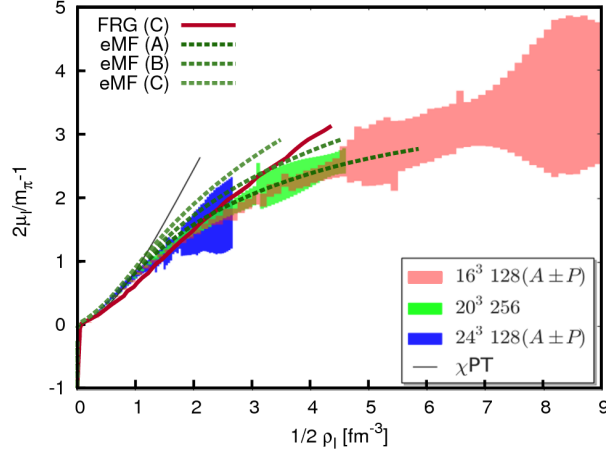


Figure 4.3.: Isospin chemical potential over isospin density at zero temperature and baryon chemical potential [2] in comparison to lattice data from [131]. The isospin densities obtained from our calculations have been rescaled by a constant factor to account for larger pion mass and pion decay constant in the lattice simulation.

the isospin density to remain zero below the onset of pion condensation at $\mu_I^c = m_\pi/2$. While this is exactly reproduced in the extended mean field calculations, the numerical solution of the full RG solution shows a slight μ -dependence even below the onset.

While chiral perturbation theory accurately describes the BEC phase, it does not reproduce the backbending of the curve near the BEC-BCS crossover, estimated around $2\mu_I/m_\pi - 1 \approx 2/3$, where mixing effects between the sigma meson and the charged

4.2. Phase Diagram of QCD with Isospin Chemical Potential

pions become important, cf. also the discussion of the mixing effects in the context of the RPA mass spectrum in Section 3.3.3. As chiral perturbation theory corresponds to the limit of an infinitely heavy sigma meson, its low-lying excitation spectrum is fundamentally different from models with a linearly realized chiral symmetry. The assertion that the backbending of the curve is related to the mixing of the meson eigenstates around the BEC-BCS crossover is supported by the fact that it is observed in the quark-meson model calculations but even in a linear sigma model where a simple calculation yields the following expression for the isospin density

$$\rho_I(x, y) = 2f_\pi^2 m_\pi x \left(\frac{y^2 - 3}{y^2 - 1} - \frac{1}{x^4} + \frac{2}{y^2 - 1} x^2 \right), \quad (4.5)$$

with $x \equiv 2\mu_I/m_\pi \geq 1$ and $y \equiv m_\sigma/m_\pi$ as before. In the $y \rightarrow \infty$ limit it reduces to the χ PT result $\rho_I(x) = 2f_\pi^2 m_\pi x (1 - x^{-4})$ from [132].

The expression for the isospin density in Eq. (4.5) illustrates that a direct comparison to the lattice requires adjusting a constant prefactor to account for different pion mass and pion decay constant on the lattice. Furthermore, already the linear sigma model result from Eq. (4.5) shows a sigma-mass dependence. To estimate its effect on the quark-meson model calculation we show three different curves for the extended mean-field calculation in Fig. 4.3 corresponding to different sigma masses. The RG results at large isospin chemical potentials should be taken with care since the assumption of isospin-independent initial conditions in the UV ceases to be valid once the characteristic scale where flow begins to deviate from the vacuum flow reaches the order of the UV cutoff scale. This was discussed in detail in Section 3.5.1 for the temperature dependence of the flow but applies of course equally to chemical potential.

4.2.3. Three-dimensional phase diagram

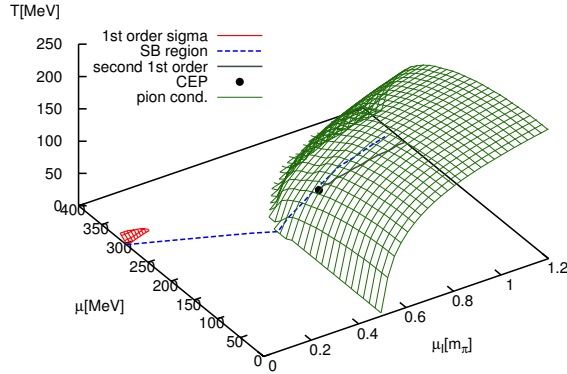


Figure 4.4.: Three dimensional phase diagram from full FRG calculation [2].

4. QCD with Isospin Chemical Potential

In Fig. 4.4 we show the three dimensional phase diagram as obtained from the full FRG calculation. The pion condensation phase boundary represented as green surface in Fig. 4.4 stays a second order phase transition throughout the whole phase diagram. The first order line in the zero isospin chemical potential plane at large quark chemical potentials, which is typical for quark meson model calculation, cf. also Fig. 3.8(a), extends into the finite isospin plane but decreases in extension with increasing isospin chemical potential and finally vanishes clearly outside the pion condensation phase. At large μ the imbalance between the Fermi surfaces of up and anti-down quarks builds up and leads to a rapid shrinkage of the pion condensation phase.

4.2.4. Chandrasekhar-Clogston transition and Sarma phases

To understand the physical significance of the additional first order transition inside the charged pion condensation phase, which was observed in the RG calculation, the analogy to the phase diagrams of imbalanced Fermi gases is helpful. These are non-relativistic fermion systems which are characterized by a population imbalance of the two fermion species and correspondingly by a chemical potential difference $\bar{\mu} = (\mu_{\uparrow} - \mu_{\downarrow})/2$ between spin-up and spin-down particles, see [133, 134, 135] for general reviews. The phase diagram is studied as a function of temperature and chemical potential difference $\bar{\mu}$. At zero temperature the Chandrasekhar-Clogston argument, which is a simple comparison of ground state energies in the BCS and the normal phase, implies the global stability of the (unpolarized) BCS ground state against spin polarization up to the Chandrasekhar-Clogston transition at $\bar{\mu} = \Delta/\sqrt{2}$, where Δ designates the BCS gap. This is a second order transition deep in the BCS phase but turns first order at or near the unitary limit [135] and marks the transition to normal matter. This first order transition extends into the finite temperature direction until it reaches a tricritical point from where on the transition turns second order with increasing temperature, see Fig. 4.5(b). Several exotic superfluidity mechanisms are under debate like inhomogeneous *Fulde-Ferrel-Larkin-Ovshnikov (FFLO) phases* and mixed *Sarma phases* corresponding to gapless polarized superfluid phases which are connected to the unpolarized BCS phase via continuous crossovers. Here we will be particularly concerned about Sarma phases, which are most conveniently understood in terms of quasiparticle dispersion relations, see [134] for a comprehensive discussion at mean-field level. The dispersion relations for spin-up and spin-down quasiparticles in the superfluid phase are shifted against each other by $\pm\bar{\mu}$ in a system with polarization. Once the spin-down branch crosses the zero-axis for $\bar{\mu} > \Delta$, modes between the two zero crossings are in a fully polarized normal state. This is often referred to as phase separation in momentum space as one has BCS pairing for quasiparticle modes with small momenta and large momenta but a fully polarized normal state for momenta centered around the minimum of the quasiparticle dispersion curve. Based on such a picture one defines the crossover to the Sarma phase by $\bar{\mu} = \Delta$, i.e. the chemical potential difference $\bar{\mu}$ for which the down-quasiparticle dispersion curve touches the zero axis. Note, however, from the Chandrasekhar-Clogston argument that the Sarma phase is not stable at $T = 0$ in the mean-field approximation, where superfluidity is

4.2. Phase Diagram of QCD with Isospin Chemical Potential

completely lost beyond the first order transition. There are, however, stable Sarma phases at larger temperatures, see Fig. 4.5(b).

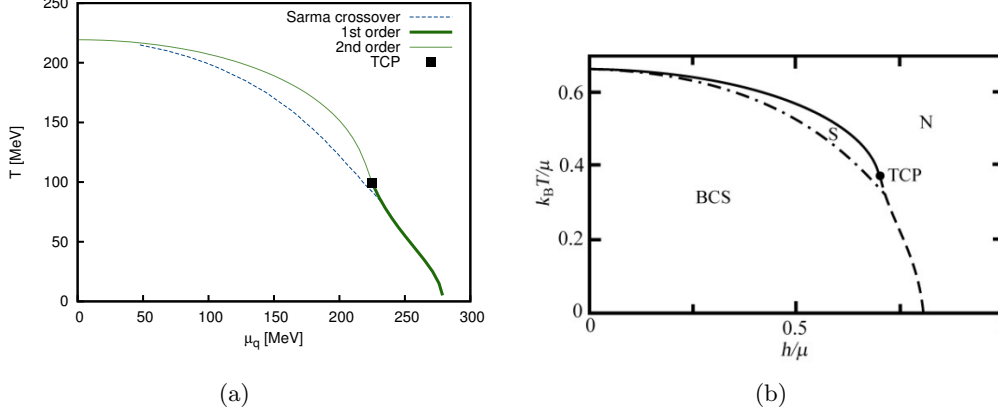


Figure 4.5.: Chandrasekhar-Clogston transitions and Sarma phases:

- (a) Phase diagram of QCD at fixed isospin chemical potential $\mu_I = m_\pi$ from extended mean-field calculation [136],
- (b) Phase diagram of an imbalanced Fermi gas at unitarity from mean-field calculation [134]

Coming back to the original question, we consider QCD with isospin chemical potential again and investigate, in particular, its phase structure at fixed isospin chemical potential $\mu_I = m_\pi$, a value near the BEC-BCS crossover in the BCS regime, as a function of quark chemical potential and temperature. Its mean-field phase diagram shows a strong similarity to the corresponding mean-field phase diagram for the polarized Fermi gas in Fig. 4.5, which might be interpreted as emergence of universal behavior near the unitary limit. The analogue of the Chandrasekhar-Clogston argument at zero temperature is the Silver Blaze property discussed in the context of the second Silver Blaze region in Section 4.2.2, which implies that the grand potential has to stay independent of μ as long as $\mu < E_{\min}^- = gd$ or, in distinction to the non-relativistic case where the Chandrasekhar-Clogston defines the location of the first order transition, up to a first order transition below this value. Here we define the crossover to the Sarma phase in analogy to the non-relativistic case via $\mu = hd$. In the isospin case the Sarma phase is characterized as a phase with a nonvanishing quark density and a nonvanishing charged pion condensate signaling a mixed but still superfluid phase.

These results should now be compared to the phase diagram in Fig. 4.6 including collective mesonic fluctuations. As remarked in the previous subsection the phase boundary of the charged pion condensation phase turns second order throughout the whole phase diagram. But more importantly in this calculation the Sarma phase gets stabilized by fluctuations and now extends down to zero temperature. The first order transition at zero temperature marks a quantum phase transition from the

4. QCD with Isospin Chemical Potential

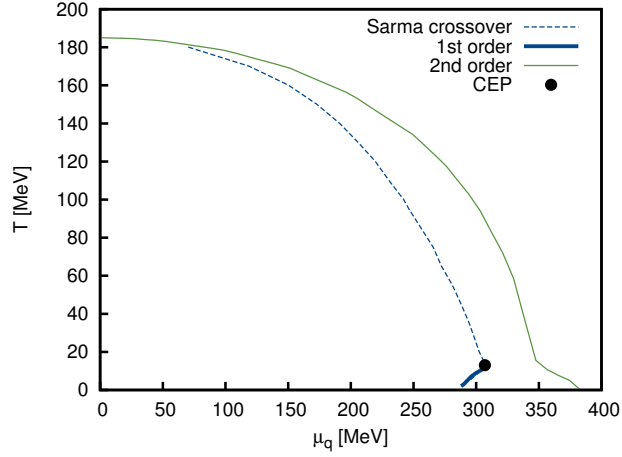


Figure 4.6.: Phase diagram of QCD at fixed isospin chemical potential $\mu_I = m_\pi$ from FRG calculation [136].

unpolarized BCS phase to the Sarma phase. Note the qualitative difference in the first order transitions in the mean-field calculation in comparison to the RG calculation as implied by the different signs of the slopes of the two transition lines in close analogy to the remarks on the chiral phase transition in Section 3.4.2, which could even be used to experimentally discriminate between a first order transition from the unpolarized BCS phase to normal matter or to a Sarma phase. It is an interesting result that fluctuations lead both in the case of the chiral transition and also in the case of the transition from superfluid matter to normal matter to a qualitative change in the nature of the phase transition. As a word of caution, one should add that the results presented in this chapter do not include perturbative UV contributions as discussed for the high-temperature regime in Section 3.5.1, which might also impact the phase structure at large baryon chemical potentials.

It is of course experimentally rather difficult to directly access the phase diagram of QCD with isospin chemical potential. It therefore remains an interesting question to investigate also the impact of fluctuations on the phase diagram of imbalanced Fermi gases with particular regard to the occurrence of mixed Sarma phases which can then ultimately even be investigated experimentally.

Part II.

**Universal Aspects of $SU(N)$ Gauge
Theories in 2+1 Dimensions**

5

$SU(N)$ Gauge Theories in 2+1 Dimensions—Universality and Self-Duality

5.1 Introduction

In this chapter we will explore in how far one can exploit the powerful tools of universality and scaling to gain a better understanding of the deconfinement transition in pure $SU(N_c)$ gauge theories. Therefore, we study the finite temperature deconfinement transition in pure lattice gauge theory i.e. in a theory with infinitely heavy quarks [137]. As pointed out in the introduction the deconfinement transition is linked to the spontaneous breaking of center symmetry Z_{N_c} in a $SU(N_c)$ gauge theory. This global Z_{N_c} center symmetry will turn out to be crucial in the case of a second order deconfinement transition as it determines the corresponding universality class. Although we focus on the 2+1 dimensional case in this chapter, the results should be understood in the broader context of a study of universal aspects of $SU(N_c)$ gauge theories. Whereas in the usual case of 3+1 dimensions only for $SU(2)$ the transition is of second order, in 2+1 dimensions both $SU(2)$ and $SU(3)$ show second order transitions. These have been analyzed in [138], [4, 139] and [3] respectively. Interestingly $SU(4)$ in 2+1 dimensions shows at least Potts scaling although the transition is probably weakly first order [3]. We will comment on the implications of our investigations for the case of $SU(4)$ later in this chapter.

The second order phase transition allows us to make use of universality arguments, namely of the *Svetitsky-Yaffe conjecture* [141] which relates the critical behaviour of a gauge theory in $d + 1$ dimensions at a second order phase transition to that of a simple d -dimensional spin model with the same (center) symmetry. In the case of $SU(N_c)$ gauge theories in 2+1 dimensions the corresponding spin systems are given by N_c -state Potts models in two dimensions, which is for $SU(2)$ nothing but the two-

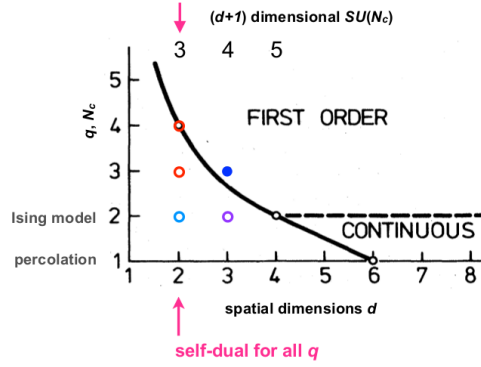


Figure 5.1.: Potts model separatrix separating first and second order transitions in 2d q -state Potts models and correspondingly in $SU(N_c)$ gauge theories in 2+1 dimensions [140].

dimensional Ising model. One can now exploit properties of these well-studied models from statistical physics such as ratios of partition functions with different boundary conditions to determine critical couplings in $SU(N)$ gauge theories. However, in 2+1 dimensions we can go even further as the q -state Potts models turn out to be self-dual. This means that they can be mapped to a theory defined on the dual lattice via a duality transformation and this dual theory turns out to be a q -state Potts model again. For two-dimensional Potts models in the infinite volume this is a well-known result [142] but has only been extended to a finite spatial volume recently [3, 4, 140]. Interestingly, the duality relation turns out to be of the form of a Z_N Fourier transform, which as we will see coincides with the relation between the spatial center vortex partition functions Z_k and the corresponding electric flux partition functions Z_e . This fact allows a direct observation of the self-duality in the gauge theories and can be exploited in a procedure to determine critical couplings to unprecedented precision. The convergence of this method is very fast compared to existing methods and the critical couplings extracted from small lattice sizes are already in very good agreement with the infinite volume extrapolation as the leading finite-size corrections cancel.

5.2 Twisted Boundary Conditions, Vortices, Universality and Self-Duality

't Hooft's twisted boundary conditions and center vortices

We start by reviewing the possible boundary conditions one can impose in a pure $SU(N_c)$ gauge theory in $d+1$ dimensions, corresponding to the different superselection sectors which can be prepared in a pure gauge theory. The reason why one can impose different boundary conditions is the fact that the gauge fields do not faithfully represent the center of the gauge group. Let us start from a $1/T \times L^d$ finite-temperature spacetime torus and consider the most general boundary conditions one can impose

5.2. Twisted Boundary Conditions, Vortices, Universality and Self-Duality

on the gauge fields which go under the name of 't Hooft's twisted boundary conditions [143]. In the most general case $A_\mu(x + L_\nu \vec{e}_\nu)$ is periodic (up to a gauge transformation depending on the direction transverse to the direction ν) with periodicity equal to the extension of the finite torus in that particular direction, i.e.

$$A_\mu(x + L_\nu \vec{e}_\nu) = \Omega_\nu(x_\perp) \left(A_\mu(x) - \frac{i}{g} \partial_\mu \right) \Omega_\nu^\dagger(x_\perp). \quad (5.1)$$

Consistency at the corners $A(x + L_\nu \vec{e}_\nu + L_\mu \vec{e}_\mu)$ leads to the cocycle condition

$$\Omega_\mu(x_\perp + L_\nu \vec{e}_\nu) \Omega_\nu(x_\perp) = Z_{\mu\nu} \Omega_\nu(x_\perp + L_\mu \vec{e}_\mu) \Omega_\mu(x_\perp), \quad (5.2)$$

where $Z_{\mu\nu}$ is a center element i.e. $Z_{\mu\nu} = \exp\left(\frac{2\pi i}{N_c} n_{\mu\nu}\right)$. The twist tensor $n_{\mu\nu} = -n_{\nu\mu}$ is gauge invariant and determines the flux sector in the (μ, ν) plane by fixing the number (modulo N_c) of center vortices in the (μ, ν) plane. These vortices can be further classified as spatial vortices linking to purely spatial planes and temporal ones linking to planes with one timelike direction. Correspondingly there are in total $N_c^{\frac{d(d+1)}{2}}$ flux sectors, i.e. gauge non-equivalent boundary conditions in $d+1$ dimensions, which subdivide into N_c^d temporal and $N_c^{\frac{d(d-1)}{2}}$ spatial sectors. More explicitly in $d=2$ and $d=3$ spatial dimensions, we classify temporal twists via a vector $\vec{k} \in Z_N^d$ with components $k_i = n_{0i}$ and spatial twist via \vec{m} with $n_{ij} = \epsilon_{ij} m$ for $d=2$ and $n_{ij} = \epsilon_{ijk} m_k$ for $d=3$ respectively.

Starting from periodic boundary conditions in the continuum twisted boundary conditions can obviously not be obtained from usual gauge transformations but require multivalued and hence singular gauge transformations [143]. On the lattice they can be implemented by multiplying a stack of plaquettes in a chosen (μ, ν) plane by a center element z . The lattice formulation represents also a particularly convenient way of understanding the appearance of vortices via twisted boundary conditions just by considering the lowest energy configurations. For $1 \neq z \in Z_{N_c}$ the lowest energy configuration of the periodic case, where all links are set to 1, is no longer consistent with the boundary conditions. In a row starting with 1 there will be some plaquette from which on the value is $z \cdot 1$ and a Wilson loop pierced by the vortex will pick up a factor of z here. This would be the configuration corresponding to a thin vortex which can still lower its free energy by spreading. In 2+1 dimensions this is a center vortex which is a line perpendicular to the original surface. In 3+1d the center vortex is a closed two-dimensional surface. More generally, in $d+1$ spacetime dimensions it will be a $d-1$ dimensional object which can link to a two-dimensional surface.

Center vortex picture of confinement

To understand the physical relevance of center vortices let us briefly introduce one particular confinement mechanism, the *center vortex picture of confinement*, see [137] for a pedagogical introduction. The overall picture is that the center vortices can link to Wilson loops and disorder them, thus leading to an area law falloff for timelike Wilson loops and thereby signaling confinement.

5. $SU(N)$ Gauge Theories in 2+1 Dimensions–Universality and Self-Duality

First we define center vortex free energies F_k which are related to ratios of partition functions of an ensemble with a certain twisted boundary condition (specified by \vec{k} and \vec{m}) compared to that from the periodic ensemble. Thus we define center vortex free energies F_k (per temperature T) via

$$R_k^{(\vec{k};\vec{m})} \equiv \frac{Z_k^{(\vec{k};\vec{m})}}{Z_k^{(\vec{0};\vec{0})}} = e^{-F_k^{(\vec{k};\vec{m})}} \quad (5.3)$$

and interpret them as free energy difference associated to adding one extra vortex.

For spatial twists the flux \vec{m} , which is perpendicular to the plane of the twist, has the interpretation of the magnetic flux of static center monopoles. At any temperature the corresponding free energies $F_k(\vec{0}, \vec{m})$ vanish for $L \rightarrow \infty$. This corresponds to an area law falloff for spatial Wilson loops at any temperature in accordance with a non-zero spatial string tension on both sides of the phase transition. The partition functions $Z_k^{(\vec{k};\vec{m})}$ tend to their zero magnetic flux analogues $Z_k^{(\vec{k};\vec{0})}$ in the thermodynamic limit $L \rightarrow \infty$ [144]. The same holds for the corresponding electric partition functions to be considered in the next section. Because of the irrelevance of the magnetic flux for the deconfinement transition we will neglect it in the following and drop \vec{m} from our notation.

The situation is different for temporal vortices. Whereas for small temperatures the situation is still analogous to the magnetic case where temporal vortices link to temporal Wilson loops and disorder them, which leads to an area-law falloff, for large temperatures with increasingly smaller extension $1/T$ of the Euclidean time direction, vortices can no longer spread arbitrarily to lower their free energy but get squeezed more and more until they are completely suppressed above the critical temperature T_c . This picture provides an intuitive understanding of the fact that the temporal center vortex free energies serve as an order parameter for the deconfinement transition [145].

Note that in $d = 2$ spatial dimensions for $N_c = 2$ and $N_c = 3$, there are only two independent twisted partition functions, namely $Z_k^{(1,0)}$ and $Z_k^{(1,1)}$ corresponding to one or two twists respectively. All other partition functions are equal to one of the former partition functions as the different configurations are just related by rotations of the whole lattice. The pattern changes in $SU(4)$ where one finds five independent partition functions with twisted boundary conditions, $Z_k^{(1,0)}$, $Z_k^{(2,0)}$, $Z_k^{(1,1)}$, $Z_k^{(2,1)}$ and $Z_k^{(2,2)}$, as the partition functions obey on isotropic cubic lattices in general $Z_k^{(m,n)} = Z_k^{(n,m)}$ and $Z_k^{(m,n)} = Z_k^{(N_c-n,m)}$.

Electric partition functions

It was shown by 't Hooft [143] that one can calculate electric partition functions Z_e from the temporal vortex partition functions Z_k via a Z_N Fourier transformation,

$$Z_e^{(\vec{e})} = \frac{1}{N^d} \sum_{\vec{k} \in \mathbb{Z}_N^d} e^{\frac{2\pi i}{N} \vec{e} \cdot \vec{k}} Z_k^{(\vec{k})}, \quad (5.4)$$

5.2. Twisted Boundary Conditions, Vortices, Universality and Self-Duality

where $\vec{e} \in Z_N^d$ is the conserved electric flux. These electric flux ensembles have an intuitive physical interpretation in terms of the electric flux between a fundamental charge and a mirror (anti-)charge in a neighboring volume in direction of \vec{e} . The ratio of a particular flux ensemble compared to the zero flux partition function is given by [140, 138]

$$\frac{Z_e^{(\vec{e})}}{Z_e^{(\vec{0})}} = \frac{1}{N} \left\langle \text{Tr} \left(\mathcal{P}(\vec{x}) \mathcal{P}^\dagger(\vec{x} + \vec{e}L) \right) \right\rangle_{\text{no-flux}}, \quad (5.5)$$

where for $\vec{m} = \vec{0}$ $\mathcal{P}(x)$ can be chosen as the (untraced) fundamental Polyakov line at \vec{x} and “no-flux” refers to the expectation value taken in the $Z_e^{(\vec{0})}$ ensemble. Analogously to the center vortex free energies we define electric free energies F_e (per temperature T) via

$$R_e^{(\vec{e})} \equiv \frac{Z_e^{(\vec{e})}}{Z_e^{(\vec{0})}} = e^{-F_e^{(\vec{e})}}. \quad (5.6)$$

Universality and the Svetitsky-Yaffe Conjecture

The missing link to the universal properties discussed in the introduction is provided by the Svetitsky-Yaffe conjecture [141]. It states that a $d+1$ dimensional gauge theory with a second order deconfinement transition has the same universal properties as a d dimension spin model. Near criticality the gauge theory can be described as an effective theory of Polyakov loops $\mathcal{P}(x)$, which faithfully represent the global Z_N center symmetry. Under a center transformation Polyakov loops transform like spins in a d -dimensional ($N_c = q$)-state Potts model with Hamiltonian [146]

$$\mathcal{H}_{\text{Potts}} = -J \sum_{\text{NN}(i,j)} \delta_{s_i, s_j} - H \sum_i \delta_{s_i, 0}, \quad (5.7)$$

for spin variables $s_i \in \{0 \dots q-1\}$ with nearest neighbor coupling J favoring parallel alignment of spins and an external field H favoring the alignment of spins in 0-direction. Such an external field is the analogue of a finite quark mass in the gauge theory.

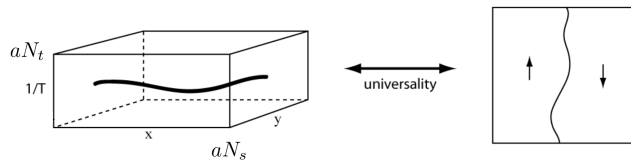


Figure 5.2.: Universality: Center vortices in the gauge theory (left side) show the same universal behavior as interfaces in the corresponding spin model (right side) [139].

The strength of this argument lies in the fact that one can now build a dictionary which links gauge theory quantities to corresponding quantities in the spin models. Polyakov loop correlators obviously map to spin correlators. Center vortices map to

interfaces in spin systems which are defects in the lattice where a cyclically shifted alignment of spins is favored rather than a parallel alignment. This is illustrated in Fig. 5.2. Ratios of partition functions $R_k^{(\vec{k})}$ as defined above map to ratios of partition functions $R_q^{(\vec{c})}$ with different cyclically shifted boundary conditions in the spin system. The vector $\vec{c} \in Z_N^2$ specifies a cyclically shifted boundary conditions by c_1 (c_2) in the x - (y -) direction.

Note also that the roles of high and low temperature phases get interchanged i.e. temporal center vortices in the high temperature (deconfined) phase behave like spin interfaces in the low temperature (ordered) phase and vice versa. In the thermodynamic limit $L \rightarrow \infty$ the ratios $R_k^{(\vec{k})}$ ($R_q^{(\vec{c})}$) for $\vec{k} \neq \vec{0}$ tend to zero in the high (low) temperature phase, where center vortices (interfaces) are suppressed. On the other hand again in the thermodynamic limit $R_k^{(\vec{k})}$ ($R_q^{(\vec{c})}$) for $\vec{k} \neq \vec{0}$ tend to 1 in the low (high) temperature phase. Only at T_c they assume a non-trivial universal value. For Potts models on a torus with different boundary conditions the partition functions at criticality have been calculated in terms of Jacobi elliptic theta functions [147] and are tabulated for the relevant cases in [140]. The intersection of the ratios R_k with the universal value at T_c can then be used to determine critical couplings.

For $SU(2)$ and $SU(3)$ we are in the fortunate situation that the universally related spin model is entirely fixed by the global Z_N symmetry. For $SU(4)$ this is no longer the case as the Z_4 symmetry is not only consistent with the standard 4-state Potts model but also with the more general 4-state Ashkin-Teller model. The Ashkin-Teller model allows three different energy levels for parallel, perpendicular and antiparallel spin alignment. By varying the ratio of the two coupling constants of the model one can interpolate between the standard 4-state Potts and a vector Potts model where the interaction energy is proportional to the dot product of the spin vectors which is then just equivalent to two non-interacting Ising models. Correspondingly the Ashkin-Teller model is characterized by continuously varying critical exponents depending on the ratio of coupling constants interpolating between the critical exponents from the limiting cases from above. The complication in the case of $SU(4)$ can be understood group theoretically following [148] where it boils down to the fact that there are three fundamental representations $4, \bar{4}$ and 6 in $SU(4)$. In an effective Polyakov loop model one then obtains two distinct terms one from loops in the $4/\bar{4}$ representation and one from loops in the 6 representation with undetermined coefficients which are the analogues of the two coupling constants in the general Ashkin-Teller model. Note in particular that this argument does not fix the relative size of the two coefficients and one thus requires additional information e.g. from a strong coupling expansion.

Self-duality

Duality transformations in the sense of Kramers and Wannier are very powerful methods in the context of statistical physics. They involve rewriting the partition function in terms of variables of the dual lattice. In the infinite volume case there are many known duality relations [142] such as the one for the 3d Ising model which

5.2. Twisted Boundary Conditions, Vortices, Universality and Self-Duality

is dual to a Z_2 gauge theory. Of particular interest are self-dual models where the original model and the dual model are of the same kind as the duality transformation then connects two models with different coupling constants. Such a self-dual model is for example the 2d Z_N spin model but most importantly in our context all q -state Potts models in two dimensions.

In the finite volume which is relevant here much less is known. The main complication here is the fact that there are different partition functions corresponding to different boundary conditions, which mix during the duality transformation. Indeed, all q -state Potts models on the torus turn out to be self-dual with partition functions related via¹

$$Z_q^{(-s,r)}(\tilde{K}) = \left(\frac{e^{\tilde{K}} - 1}{e^K - 1} \right)^{N_{\text{sites}}} \frac{1}{q} \sum_{m,n=0}^{q-1} e^{2\pi i(rm+sn)/q} Z_q^{(m,n)}(K), \quad (5.8)$$

where N_{sites} denotes the number of lattice sites and the coupling per temperature $K = J/T$ is related to its dual \tilde{K} via

$$(e^{\tilde{K}} - 1)(e^K - 1) = q, \quad (5.9)$$

which are then mirrored around the critical value $K_c = \tilde{K}_c = \log(1 + \sqrt{q})$ which is easily obtained from Eq. (5.9).

The most important fact in this context is that the duality relation Eq. (5.8) has the form of a Z_q Fourier transform which is the same relation as that between center vortex and electric partition functions discussed in Eq. (5.4). This means we can rewrite Eq. (5.4) as

$$R_e^{(\vec{e})}[K] = \frac{\sum_{\vec{k}} e^{2\pi i(\vec{k} \cdot \vec{e})/N} R_k^{(\vec{k})}[K]}{\sum_{\vec{k}'} R_k^{(\vec{k}')}[K]} = R_k^{(\hat{e})}[\tilde{K}], \quad (5.10)$$

where $\hat{e} = (-e_2, e_1)$ for $\vec{e} = (e_1, e_2)$.² This implies in particular $R_e^{(\vec{e})}[K_c] = R_k^{(\hat{e})}[K_c]$ at the critical coupling K_c . Furthermore, from Eq. (5.9) we have $\frac{\partial \tilde{K}}{\partial K} \Big|_{K_c} = -1$ implying $(K - K_c) = -(\tilde{K} - K_c) + \mathcal{O}(K^2)$. We know that $F_e^{\vec{e}} = -\log \hat{Z}_e^{\vec{e}}$ and $F_k^{\vec{e}} = -\log \hat{Z}_k^{\vec{e}}$ are universal scaling functions of the finite size scaling variable $x = N_s t^\nu$, where $t = T/T_{\text{crit}} - 1$ is the reduced temperature. In this context self-duality simply implies $F_k^{\vec{e}}(x) = F_e^{\vec{e}}(-x)$ or equivalently

$$R_k^{\vec{e}}(x) = R_e^{\vec{e}}(-x) \quad (5.11)$$

¹The most elegant proof of the duality relation [140] uses the random cluster formulation of the Potts model [147]. Alternatively one can follow [142] with appropriate finite volume modifications similar to [149]. For $q = 2$ and with the conventional replacement $K \rightarrow K/2$ one reproduces the known result for the Ising model in a finite volume which can even be verified exactly using the existing analytical expressions for the partition functions.

²For an isotropic square lattice one can employ the relations $Z_q^{(r,s)} = Z_q^{(s,r)}$ and $Z_q^{(q-r,s)} = Z_q^{(r,s)}$ and thus simply set $\hat{e} = \vec{e}$ as we will do in the following.

5. $SU(N)$ Gauge Theories in 2+1 Dimensions—Universality and Self-Duality

because by assumption we are dealing with a region where the dual coupling scales linearly with the original coupling. This property is nicely reflected in the numerical data for $SU(2)$ and $SU(3)$ shown in Fig. 5.3 where $R_k(x)$ and $R_e(-x)$ collapse onto a single curve thus providing direct numerical evidence for the self-duality.

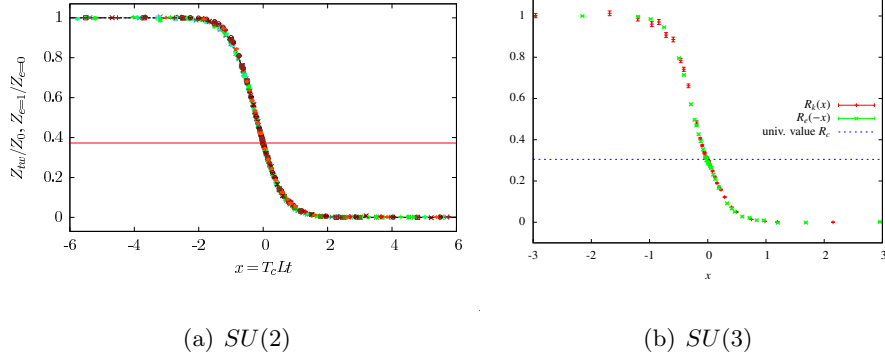


Figure 5.3.: Direct numerical evidence for self-duality for a single twist $\vec{e} = (1, 0)$
 (a) in $SU(2)$ ($N_t = 4$ and N_s up to 96) [4],
 (b) in $SU(3)$ ($N_t = 2$ and $N_s = 24$) [3] .

Algorithmic details

For a general introduction to Lattice gauge theory and description of standard algorithms see [80, 150]. Here we use a standard Wilson gauge action and a heat bath algorithm supplemented by overrelaxation steps. $SU(N)$ updates are implemented in the usual way as subsequent updates of $SU(2)$ subgroups [151]. Apart from this standard setup a few words about the calculation of ratios R_k are required. Due to poor overlap it is numerically advantageous not to compute the ratio $\frac{Z_{tw}}{Z_0}$ at once but rather to determine it from independently simulated ratios $\frac{Z_{k+1}}{Z_k}$ of partition functions corresponding to ensembles which differ only by a single flipped plaquette. Here we describe the procedure for a single twist where for example $Z_{tw} = Z_k^{(1,0)}$ and $Z_0 = Z_k^{(0,0)}$. This is the idea of the Snake algorithm [152]. At the end the different ratios are just multiplied to yield the desired ratio of partition functions

$$\frac{Z_{tw}}{Z_0} = \frac{Z_M}{Z_{M-1}} \cdot \frac{Z_{M-1}}{Z_{M-2}} \dots \frac{Z_1}{Z_0}, \quad (5.12)$$

where M designates the extension of the lattice in the direction of the twist.

We start with the partition function in the untwisted ensemble

$$Z_0 = \int \prod_i dU_i e^{\beta \sum_j \text{Re Tr} P_j} \quad (5.13)$$

5.3. Critical Couplings from Universality and Self-Duality

where P_j are the plaquette variables. In $SU(N)$ flipping plaquettes means multiplying it by a center element z , which just implies flipping the sign of the plaquette coupling in $SU(2)$. For the partition function with $k + 1$ flipped plaquettes we find

$$\begin{aligned} Z_{k+1} &= \int \prod_i dU_i e^{+\beta \sum_{j=1}^{k+1} \text{Re Tr}(zP_j) + \beta \sum_{j=k+2}^N \text{Re Tr}P_j} \\ &= \int \prod_i dU_i e^{\beta \text{Re Tr}zP_{k+1}} e^{\beta \sum_{j=1}^k \text{Re Tr}zP_j + \beta \sum_{j=k+2}^N \text{Re Tr}P_j} \\ &= \langle e^{\beta \text{Re Tr}zP_{k+1}} \rangle_k, \end{aligned} \quad (5.14)$$

where $\langle \dots \rangle_k$ denotes the expectation value take in an ensemble with $1, \dots, k - 1$ flipped plaquettes and where the k th coupling set to zero. Writing Z_k in a similar fashion, the ratio Z_{k+1}/Z_k can be calculated using

$$\frac{Z_{k+1}}{Z_k} = \frac{\langle e^{\beta \text{Re Tr}zP_{k+1}} \rangle_k}{\langle e^{\beta \text{Re Tr}P_{k+1}} \rangle_k} \quad (5.15)$$

via measurements in an ensemble with $k - 1$ flipped plaquettes.

5.3 Critical Couplings from Universality and Self-Duality

Critical couplings from intersection with the universal value

The determination of critical couplings in pure gauge theories has a longer history with increasingly efficient methods ranging from pairwise intersections of Binder cumulants to the intersection of partition functions with different boundary conditions. An even more efficient method which exploits the universal properties of the universally related spin models was put forward in [139]. We saw in the previous section the ratios R_k of center vortex partition functions at T_c assume a universal value $R_{k,c}^{\vec{k}}$ which can be calculated for the corresponding spin models and is listed for the relevant cases in [140]. Here temperature is controlled via the lattice coupling β . The extrapolation based on the *finite-size-scaling* (FSS) Ansatz

$$R_k^{(\vec{k})}(\beta) = R_{k,c}^{(\vec{k})} + b_k^{(\vec{k})}(\beta - \beta_c(N_t))N_s^{1/\nu} + c_k^{(\vec{k})}N_s^{-\omega_k^{(\vec{k})}} + \dots, \quad (5.16)$$

where $\omega_k^{(\vec{k})}$ is the correction to scaling exponent related to the breaking of rotational symmetry, which is determined as a by-product in our analysis. We use the expression from above to define pseudo-critical couplings $\beta_c(N_t, N_s)$ by the intersections of $R_k^{(\vec{k})}(\beta)$ with the universal value which is precisely the value of β for which the correction terms in Eq. (5.16) vanish i.e.

$$\beta_c(N_t, N_s) = \beta_{c,\infty}(N_t) - d(N_t)N_s^{-(\omega_k^{(\vec{k})} + 1/\nu)} + \dots, \quad (5.17)$$

5. $SU(N)$ Gauge Theories in 2+1 Dimensions–Universality and Self-Duality

where $d(N_t)$ will be simply determined as a N_t dependent fit parameter. At fixed N_t and for fixed critical exponent ν , a three parameter fit of the pseudo-critical couplings yields the continuum critical coupling $\beta_{c,\infty}(N_t)$ and the correction to scaling exponent ω .

Critical couplings from self-duality

However, there is an even more efficient method which makes use of self-duality. Therefore, one has to recall from Eq. (5.10) that selfduality requires $R_k^{\vec{k}}(\beta_c) = R_e^{\vec{k}}(\beta_c)$. This means we can alternatively extract β_c from the value $\beta_{c,\text{int}}(N_t, N_s)$ where $R_k^{\vec{k}}(\beta)$ and $R_e^{\vec{k}}(\beta)$ intersect. This gives a numerical estimate for the critical coupling β_c , which shows a significantly faster speed of convergence than the already very efficient method discussed in the previous subsection. The reason for these extremely good convergence properties is the fact that the leading finite size scaling corrections to β_c as determined by this method vanish, which is in turn a direct consequence of the self-duality. To see this consider a FSS Ansatz for $R_e^{\vec{k}}$ completely analogous to that for $R_k^{\vec{k}}$, Eq. (5.16),

$$R_e^{\vec{k}}(\beta) = R_{e,c}^{\vec{k}} + b_e^{\vec{k}}(\beta - \beta_c(N_t))N_s^{1/\nu} + c_e^{\vec{k}}N_s^{-\omega_e^{\vec{k}}} + \dots \quad (5.18)$$

Defining critical couplings β_{int} via $R_k^{\vec{k}}(\beta_{\text{int}}) = R_e^{\vec{k}}(\beta_{\text{int}})$, we obtain

$$\beta_{\text{int}} = \beta_c + \frac{1}{N_s^{1/\nu}(b_k^{\vec{k}} - b_e^{\vec{k}})} \left(R_{e,c}^{\vec{k}} - R_{k,c}^{\vec{k}} + c_e^{\vec{k}}N_s^{-\omega_k^{\vec{k}}} - c_e^{\vec{k}}N_s^{-\omega_e^{\vec{k}}} \right). \quad (5.19)$$

Self-duality in a finite volume requires that $R_k^{\vec{k}}(\beta_{\text{int}}) = R_e^{\vec{k}}(\beta_{\text{int}})$ and $R_k^{\vec{k}\prime}(\beta_{\text{int}}) = -R_e^{\vec{k}\prime}(\beta_{\text{int}})$, which implies $R_{e,c}^{\vec{k}} = R_{k,c}^{\vec{k}}$, $\omega_k^{\vec{k}} = \omega_e^{\vec{k}}$, $c_k^{\vec{k}} = c_e^{\vec{k}}$ and $b_k^{\vec{k}} = -b_e^{\vec{k}}$ and Eq. (5.19) then shows that the leading FSS corrections cancel. At criticality we find $R_k^{\vec{k}}(\beta_c) = R_{k,c}^{\vec{k}} + c_k^{\vec{k}}N_s^{-\omega_k^{\vec{k}}}$, which means that the intersection point is only shifted vertically away from universal value due to finite size effects. This property allows in principle to determine the correction to scaling exponent ω from the differences to the universal value although it is numerically simpler to employ Eq. (5.17). Again, this is nicely observed in numerical data for $SU(2)$ and $SU(3)$, here exemplarily shown for $N_t = 4$ in Fig. 5.4. In both cases one observes an improved rate of convergence for the self-duality method compared to the previously discussed method of intersections with the universal value. Note in particular that in both cases the unextrapolated critical coupling from the self-duality method for $N_s = 16$ already overlaps with the previously extrapolated value within errors.

The critical couplings for $SU(3)$ given in Tab. 5.1 are consistent with the existing literature values but represent an improvement in accuracy of up to one order of magnitude. Again the critical couplings from the two methods discussed in detail agree within errors. The critical couplings obtained from intersection with the universal value were extrapolated using Eq. (5.16), whereas the critical couplings from self-duality just

5.3. Critical Couplings from Universality and Self-Duality

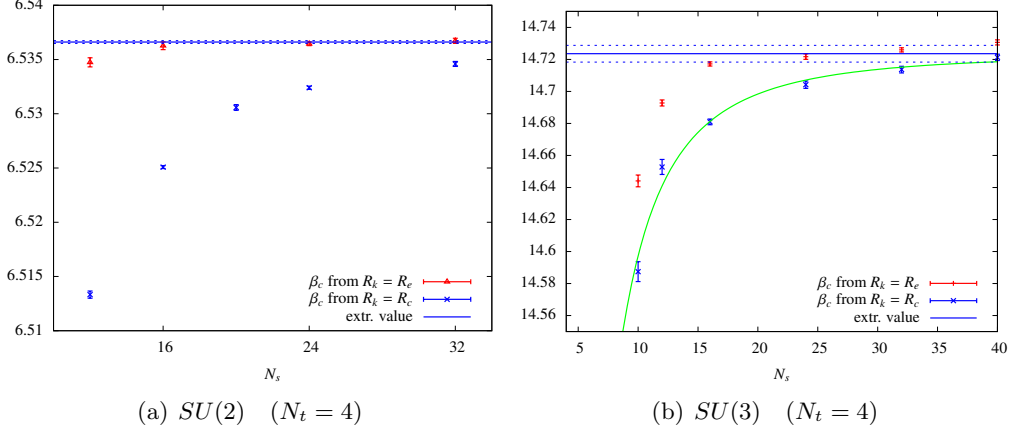


Figure 5.4.: Critical couplings from intersection with the universal value ($R_k = R_c$) compared to critical couplings from self-duality ($R_k = R_e$) [3].

represent weighted means from values for different spatial lattice extensions N_s with sufficiently large aspect ratios N_s/N_t .

N_t	$\beta_c(R_k = R_e)$	$\beta_c(R_k = R_c)$	Lit.
2	8.15309(11)	8.15297(57)	8.1489(31) [†]
4	14.7262(9)	14.7194(45)	14.717(17) [†]
6	21.357(25)	-	21.34(4) [‡]
8	27.84(12)	-	-

Table 5.1.: $SU(3)$ critical couplings from self-duality (weighted means), intersection with the universal value (extrapolated), and literature values from [†][153], [‡][154].

Critical temperature and critical exponents

Given the critical couplings $\beta_c(N_t)$ one can determine the critical temperature straightforwardly. Unlike in 3+1 dimensions, where the coupling is dimensionless, the coupling g_3^2 has dimensions of mass in 2+1 dimensions and is related to the bare lattice coupling β via $\beta = \frac{2N_c}{ag_{3B}^2}$, where a is the lattice distance. Expanding the bare coupling as $g_{3B}^2 = g_3^2 + c_1 a g_3^4 + c_2 a^2 g_3^6 + \dots$ and substituting it into β yields

$$\frac{\beta}{2N_c} = \frac{T_c}{g_3^2} - c_1 - c_2 \frac{g_3^2}{T_c} \frac{1}{N_t} + \dots \quad (5.20)$$

5. $SU(N)$ Gauge Theories in 2+1 Dimensions—Universality and Self-Duality

Now we exploit the relation $T = \frac{1}{N_t a}$ by evaluating it at fixed temperature T_c . This yields

$$\beta_c(N_t) = 2N_c \frac{T_c}{g_3^2} N_t - 2N_c c_1 - 2N_c c_2 \frac{g_3^2}{T_c} \frac{1}{N_t} + \dots \quad (5.21)$$

Fitting $\beta_c(N_t)$ according to an Ansatz of the form of Eq. (5.21) allows us to extract T_c in terms of the coupling g_3^2 . Using literature values for $\sqrt{\sigma}/g_3^2$ this can then be converted into T_c in terms of the zero temperature string tension $\sqrt{\sigma}$. In $SU(2)$ it was demonstrated using critical couplings for a large number of different N_t values that it is even possible to numerically determine the subleading $1/N_t$ corrections in Eq. (5.21) [139]. In $SU(3)$ we do not aim to quantify these and fit the values $\beta_c(N_t)$ for $N_t = 4, 6, 8$ according to Eq. (5.21) with $c_2 = 0$ which yields $T_c/g_3^2 = 0.5475(3)$ and correspondingly $T_c/\sqrt{\sigma} = 0.9938(9)$ using the weighted average $\sqrt{\sigma}/g_3^2 = 0.5509(4)$ of the literature values from [155].

Furthermore, we can numerically determine the correlation length critical exponent ν . For the case of $SU(3)$ this is just a cross check as the critical exponent $\nu = 5/6$ for the 2d 3-state Potts model is an established although still conjectured value, but it will turn out useful for the case of $SU(4)$, to be discussed in the next subsection, where the universal spin model and correspondingly its critical exponents are not fixed by the global Z_4 symmetry. To extract the correlation length critical exponent one exploits the fact that the center vortex free energies F_k are just a function of $L^{1/\nu} t$ for sufficiently large L . Using $t \propto (\beta - \beta_c)$ and expanding $F_k(\beta) = -\log R_{k,c} + d(N_s)(\beta - \beta_c) + \dots$ one observes that the slope $d(N_s)$ should scale as $d(N_s) \propto N_s^{1/\nu}$. Fitting these slopes in $SU(3)$ yields an exponent $\nu = 0.82(4)$ which is consistent with the exponent $\nu = 5/6$ from the 2d 3-state Potts model.

Order of the phase transition in $SU(4)$ in 2+1 dimensions

We close this chapter with a few remarks on the case of $SU(4)$ in 2+1 dimensions. This case is interesting for two reasons: Firstly, the order of the phase transition was discussed extensively in the literature [153, 156, 157]. Although the recent investigations [153, 157] favor a weakly first order transition, the distinction between a second order and a weakly first order transition is a notoriously difficult task on the lattice. This is why we apply our universality methods to $SU(4)$ as well, which should lead to inconsistencies for large spatial extensions where the (approximate) second order scaling eventually breaks down. But secondly, even in the case of (approximate) second order scaling the question is which of the Ashkin-Teller models, all consistent with the global Z_4 symmetry, is the universal partner of the $SU(4)$ gauge theory in 2 + 1 dimensions.

Assuming a second order phase transition but without demanding Potts scaling we can still determine critical couplings from pairwise intersections of F_k 's, here using pairs of lattices with N_s ratios of 2:1, see Fig. 5.5(a). Here the extrapolated value for $N_t = 4$, $\beta_c = 26.283(9)$, turns out to be consistent within errors with the critical coupling $\beta_c = 26.294(2)$ extracted from intersection with the universal value for the

5.3. Critical Couplings from Universality and Self-Duality

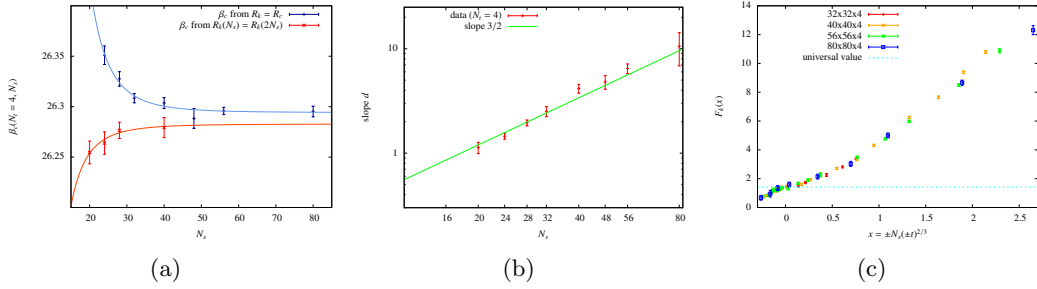


Figure 5.5.: $SU(4)$ analysis [3]:

- (a) $SU(4)$ critical couplings ($N_t = 4$),
- (b) Slopes $d(N_s)$ compared to power law with Potts model exponent $\nu = 2/3$,
- (c) Check of Potts model scaling for $SU(4)$ ($N_t = 4$).

4-state Potts model as discussed above. Interestingly, the correlation length critical exponent determined as discussed in the previous subsection is found to be $\nu = 0.59(5)$, where the error takes into account a systematic uncertainty due to the uncertainty in β_c . As observed for $SU(2)$ and $SU(3)$ the method tends to underestimate ν , so the result seems to be most consistent with the 4-state Potts model critical exponent $\nu = 2/3$, which is the smallest value among all Ashkin-Teller models. The consistency of the slopes $d(N_s)$ with a power law and Potts model critical exponent $\nu = 2/3$ is illustrated in Fig. 5.5(b).

The Potts scaling is illustrated in Fig. 5.5(c) with data from lattices with spatial extension N_s up to 80. Up to this spatial extension one observes no obvious violation of Potts model scaling. One should, however, be careful interpreting this as a sign for a second order phase transition as the investigated lattice sizes are probably still too small to discriminate between a second order and a weakly first order transition. Furthermore, the order of the phase transition might even depend on N_t . Even in the case of a weakly first order transition it is, however, an interesting observation that the approximate second order scaling seems to be most consistent with Potts model scaling, although there is no obvious reason which prefers it over the other Ashkin-Teller models with the same global Z_4 symmetry.

6

Summary and Outlook

The common theme of all topics subsumed in this thesis is the study of different aspects of QCD and here in particular aspects of finite density QCD and the deconfinement transition. These were, however, not investigated in QCD itself but rather in QCD-like theories obtained by slight deformations of the QCD Lagrangian. In this chapter we want to highlight some of the most important results together with an outlook on possible next steps for the future.

We start our summary with the last chapter, which should be seen as an example for choosing the right set of tools for a particular problem and for the benefits of connecting knowledge from different branches of physics. More specifically, it demonstrates the power of universality methods. These are of course not directly applicable to $SU(3)$ in 3+1 dimensions due to the first order nature of the phase transition in the pure gauge theory. However, if we either reduce the number of colors or the number of spatial dimensions they can be applied very efficiently. Here it is a quite remarkable result that properties of the corresponding universally related spin models– in 2+1 dimensions in particular their self-duality– can be directly observed in the gauge theory. But even given these very efficient tools the analysis of the case of $SU(4)$ in 2+1 dimensions illustrates the difficulties in the analysis of phase transitions in general and the discrimination between a second order and a weakly first order transition in particular.

We saw that strongly interacting theories like QCD at the scales relevant for hadron physics require dedicated non-perturbative tools and encountered lattice QCD and the Functional Renormalization Group as two complementary approaches. With regard to the application to the QCD phase diagram one message is that these different approaches should be tested against each other, which is of course hard to achieve in 3-color QCD at finite densities due to the fermion sign problem in Lattice QCD. It provides at the same time one of the main motivations for studies of theories where

6. Summary and Outlook

such a comparison is possible at finite chemical potential, may it be in QCD-like theories with positive fermion determinants or in non-relativistic systems like ultracold fermionic gases. Such studies can then also tell us something about the reliability of our methods in general and for the 3-color case in particular. The second important message is that effective model studies as employed here are extremely valuable tools for the understanding of lattice results and can even be used to guide future lattice simulations.

Let us now turn to the first part of the thesis, and in particular to the second part of Chapter 2, where we proposed a very simple truncation for the flow of the 2-point function. This represents, however, just the first step required for the computation of real-time quantities. The crucial step remains the analytical continuation from Euclidean to Minkowski spacetime, which was carried out here on the level of the flow equations and which allowed to extract spectral functions and pole masses. Such a proper mass definition via the pole of the corresponding propagator was found to be essential to satisfy the Silver Blaze property at zero temperature. Of further general relevance for effective model calculations is the observed deviation of the commonly used pion screening mass and the physical pion mass, which were expected to represent a subleading effect but turned out to be of the order of 30% in a model with both fermionic and bosonic degrees of freedom at leading order in the derivative expansion.

Another focus of this thesis was the study of QCD-like theories with positive fermion determinants. These were discussed in effective model approaches for the three representative examples of 2-color QCD, adjoint QCD and QCD with isospin chemical potential. In particular, we presented numerical results for the phase diagrams of 2-color QCD and QCD with isospin chemical potential taking into account both fermionic and collective mesonic/baryonic fluctuations within the framework of the FRG. Here the development of solution methods for flow equations of full field-dependent effective potential parametrized by several invariants represented an important advance from the technical point of view. These first FRG studies represent already an important step beyond the well-studied mean-field approaches but remain to be improved in particular in two important aspects in the future. The first concerns the inclusion of gauge degrees of freedom, which was presented here only as an outlook in the form of the coupling to a phenomenological Polyakov loop potential, however, including matter-backcoupling to the gauge sector in the form of an adjusted transition temperature in the Polyakov loop potential. The latter is, however, just the first step in the direction of a proper inclusion of the full flow of the gauge sector. Also in this context 2-color QCD may serve as a useful test case for different approaches for incorporating gauge degrees of freedom in order to eventually firmly anchor effective model calculations in full QCD. The second important point is to check the reliability of the obtained results in more refined truncations. Here we proposed a truncation which goes beyond the zeroth order derivative expansion and presented flow equations which remain to be solved numerically in the future.

Apart from the absence of a fermion-sign problem, another reason to concentrate on 2-color QCD was that it allows a very transparent demonstration of the impact of baryonic degrees of freedom; its phase diagram neglecting diquark condensation closely

resembles the corresponding quark-meson model phase diagrams for 3-color QCD including a critical endpoint which, however, vanishes in the diquark condensation phase after properly including diquark degrees of freedom. The impact of baryonic degrees of freedom in 2-color QCD is one example for the predictive power of QCD-like theories as it stresses the importance of these degrees of freedom for the 3-color phase diagram in general and the fate of the critical endpoint in particular. The study of baryonic degrees of freedom in 3-color QCD but perhaps also in adjoint QCD is the next important step in the direction of a further improvement of functional methods calculations at finite baryon densities. One starting point in this direction could be the study of baryon-meson models as baryons and mesons represent the relevant degrees of freedom for the description of the experimentally well-established nuclear matter liquid gas transition. With the baryon-meson sector under control it is then a comparably simple step to augment it by quarks and (color charged) diquarks and appropriately constructed interaction terms consistent with Lorentz and isospin symmetry to construct a quark-meson-diquark-baryon model.

Finally, the case of QCD with isospin chemical potential represents not only an interesting problem on its own, which is related to that of 2-color QCD and which allows in addition to study the competing effects of both baryon and isospin chemical potential, but was supposed to illustrate the close relations between relativistic QCD-like theories and non-relativistic polarized Fermi gases. Here the strong similarities between the phase diagrams of these two physically vastly different systems was an interesting observation, which might be interpreted as emergence of universal behavior of strongly coupled systems in general. Furthermore, only the analogy to the polarized Fermi gases helped to clarify the interpretation of the additional first order transition inside the superfluid phase as a quantum phase transition to a Sarma phase, which was stabilized by fluctuations. The fate of the Sarma phase in the original non-relativistic system under inclusion of bosonic fluctuations is just one of several questions which might be triggered by this correspondence and which remain to be investigated in the future.

A

Notations and Conventions

Integration and Fourier transform

We define a shorthand notation for integrations

$$\int_p \equiv \int \frac{d^d p}{(2\pi)^d} \quad \int_x \equiv \int d^d x \quad \oint_p = T \sum_{n \in \mathbb{Z}} \int \frac{d^{d-1} p}{(2\pi)^{d-1}}, \quad (\text{A.1})$$

where a sum over periodic (antiperiodic) Matsubara modes $p_0 = \omega_n \equiv 2n\pi T$ ($p_0 = \nu_n \equiv (2n+1)\pi T$) is understood.

For Fourier transformation we employ the following conventions

$$\phi(p) \equiv \int_x \phi(x) e^{-ipx} \quad \phi(x) = \int_p \phi(p) e^{ipx}; \quad \psi(p) \equiv \int_x \psi(x) e^{-ipx} \quad \bar{\psi}(p) \equiv \int_x \bar{\psi}(x) e^{ipx}. \quad (\text{A.2})$$

Dirac algebra

For Euclidean signature we use hermitian gamma matrices obeying

$$\{\gamma^i, \gamma^j\} = 2\delta^{ij} \quad (\text{A.3})$$

which can be represented explicitly as

$$\gamma^\mu = i \begin{pmatrix} 0 & \tilde{\sigma}^\mu \\ \sigma^\mu & 0 \end{pmatrix} \quad \text{where} \quad \sigma^\mu = (-i, \sigma^j), \quad \tilde{\sigma}^\mu = (-i, -\sigma^j) = -\sigma^{\mu\dagger} \quad (\text{A.4})$$

and

$$\gamma^5 = \gamma^1 \gamma^2 \gamma^3 \gamma^0 = \begin{pmatrix} 1 & 0 \\ 0 & -1 \end{pmatrix} \quad (\text{A.5})$$

A. Notations and Conventions

The charge conjugation matrix $C = \gamma^2\gamma^0$ obeys

$$\begin{aligned}
C^T &= C^\dagger = C^{-1} = -C, \quad \text{i.e.} \quad C^2 = -1 \\
C\gamma^\mu C &= \gamma^{\mu T} \quad \text{and} \quad C\gamma^5 C = -\gamma^5 \quad \text{i.e.} \quad [C, \gamma^5] = 0 \\
\psi^C &= C\bar{\psi}^T (= C\gamma^0\psi^* = -\gamma^0 C\psi^*) \quad \text{and thus} \quad \overline{\psi^C} = \psi^T C \\
S^{\mu\nu T} C\gamma^5 &= -C\gamma^5 S^{\mu\nu}
\end{aligned} \tag{A.6}$$

For Lorentz transformations of spinors we define

$$\Lambda_{\frac{1}{2}} = \exp\left(\frac{i}{2}\omega_{\mu\nu}S^{\mu\nu}\right) \quad S^{\mu\nu} = \frac{i}{4}[\gamma^\mu, \gamma^\nu]. \tag{A.7}$$

B

Flow Equations for the 2-point Functions in the $O(N)$ Model

In this appendix we explicitly evaluate the different contributions to the flow equation for the mesonic 2-point functions in the $O(N)$ model for the sharp 3-momentum regulator

$$R_k(\vec{q}^2) = (k^2 - \vec{q}^2)\Theta(k^2 - \vec{q}^2) \quad (\text{B.1})$$

from Eq. (3.66). For $I_k^{(n)}(\phi^2)_m$ from Eq. (2.28) one obtains explicitly

$$I_k^{(1)}(\phi^2)_m = \frac{k^5}{3\pi^2}(1 + 2n_b(E))\frac{1}{2E}, \quad (\text{B.2})$$

$$I_k^{(2)}(\phi^2)_m = \frac{k^5}{3\pi^2} \left(\frac{1}{4E^3}(1 + 2n_b(E)) - \frac{1}{2E^2}n_b'(E) \right), \quad (\text{B.3})$$

where $E^2 = k^2 + m^2$ and $n_b(E)$ designates the Bose-Einstein distribution function

$$n_b(E) \equiv n_b(E; T) = \frac{1}{e^{E/T} - 1}. \quad (\text{B.4})$$

The symmetrized expression $J_k(p_0, \phi^2)_{m_1, m_2} + J_k(p_0, \phi^2)_{m_2, m_1}$, which is related to Eq. (2.32) and appears in the flow equations (2.30) and (2.31), evaluated for purely

B. Flow Equations for the 2-point Functions in the $O(N)$ Model

timelike external momentum $p_\mu = (p_0, \vec{0})$ yields

$$\begin{aligned}
& J_k(p_0, \phi^2)_{m_1, m_2} + J_k(p_0, \phi^2)_{m_2, m_1} \\
&= \frac{k^5}{3\pi^2} \left([1 + n_b(E_1) + n_b(E_2)] \frac{(E_1 + E_2)^3 (E_1^2 + E_1 E_2 + E_2^2) + (E_1^3 + E_2^3) p_0^2}{4E_1^3 E_2^3 (p_0^2 + (E_1 + E_2)^2)^2} \right. \\
&\quad - [n_b(E_1) - n_b(E_2)] \frac{(E_1 - E_2)^3 (E_1^2 - E_1 E_2 + E_2^2) + (-E_1^3 + E_2^3) p_0^2}{4E_1^3 E_2^3 (p_0^2 + (E_1 - E_2)^2)^2} \\
&\quad - [n'_b(E_1) + n'_b(E_2)] \frac{(E_1^2 - E_2^2)^2 + (E_1^2 + E_2^2) p_0^2}{4E_1^2 E_2^2 (p_0^2 + (E_1 - E_2)^2) (p_0^2 + (E_1 + E_2)^2)} \\
&\quad \left. + [n'_b(E_1) - n'_b(E_2)] \frac{(E_1^2 - E_2^2) (E_1^2 + E_2^2 + p_0^2)}{4E_1^2 E_2^2 (p_0^2 + (E_1 - E_2)^2) (p_0^2 + (E_1 + E_2)^2)} \right), \tag{B.5}
\end{aligned}$$

where $E_i^2 = \sqrt{k^2 + m_i^2}$ as defined above.



$SU(2N)/Sp(N)$ and $SU(2N)/SO(2N)$ Cosets and their Properties

C.1 Coset Generators

In this section we outline the explicit construction of the generators of the coset $SU(2N)/Sp(N)$, which is coset relevant for the symmetry breaking in fundamental 2-color matter, and of the generators of $SU(2N)/SO(2N)$, which is relevant for adjoint matter. More explicitly, we are looking for $U \in SU(2N)$ which preserve

$$U^T \Sigma_0 U = \Sigma_0, \quad (\text{C.1})$$

where Σ_0 is given by Eq. (3.13) and Eq. (3.14) respectively. Therefore we split the $(2N)^2 - 1$ generators of $SU(2N)$, given just as a basis of the $2N \times 2N$ traceless hermitian matrices, into unbroken generators $\{T^a\}$ giving rise to group elements satisfying Eq. (C.1) and the remaining coset generators $\{X^a\}$. On the level of the generators condition (C.1) translates itself into

$$T^{aT} \Sigma_0 + \Sigma_0 T^a = 0. \quad (\text{C.2})$$

We define the coset generators as subset of $SU(2N)$ generators obeying

$$X^{aT} \Sigma_0 - \Sigma_0 X^a = 0. \quad (\text{C.3})$$

This statement will be checked below by simply ensuring that the vector space spanned by the hermitian traceless generators T^a and X^a satisfying Eq. (C.2) and Eq. (C.3) really constitutes the Lie algebra of $SU(2N)$.

C. $SU(2N)/Sp(N)$ and $SU(2N)/SO(2N)$ Cosets and their Properties

$SU(2N)/Sp(N)$ generators

The Lie algebra of $SU(2N)$ can be split explicitly into the subspaces

$$\begin{aligned} T &= \left\{ \begin{pmatrix} D & E \\ E^\dagger & -D^T \end{pmatrix} \mid D = D^\dagger, E^T = E \right\}, \\ X &= \left\{ \begin{pmatrix} F & G \\ G^\dagger & F^T \end{pmatrix} \mid F = F^\dagger, \text{Tr}(F) = 0, G^T = -G \right\}. \end{aligned} \quad (\text{C.4})$$

T forms a $N(2N + 1) = \dim Sp(N)$ -dimensional vectorspace which turns out to be the Lie algebra of $Sp(N)$ as the elements $T^a \in T$ satisfy $T^{aT}\Sigma_0 + \Sigma_0 T^a = 0$. X forms a $N(2N - 1) - 1$ dimensional vectorspace and can then be identified with the generators of the coset where the coset elements $X^a \in X$ indeed satisfying $X^{aT}\Sigma_0 - \Sigma_0 X^a = 0$.

As we are particularly interested in the case of $N = 2$ we explicitly state a basis for the coset generators

$$X_1 = \begin{pmatrix} \sigma_1 & 0 \\ 0 & \sigma_1 \end{pmatrix}, X_2 = \begin{pmatrix} \sigma_2 & 0 \\ 0 & -\sigma_2 \end{pmatrix}, X_3 = \begin{pmatrix} \sigma_3 & 0 \\ 0 & \sigma_3 \end{pmatrix}, X_4 = \begin{pmatrix} 0 & -i\sigma_2 \\ i\sigma_2 & 0 \end{pmatrix}, X_5 = \begin{pmatrix} 0 & -\sigma_2 \\ -\sigma_2 & 0 \end{pmatrix}. \quad (\text{C.5})$$

$SU(2N)/SO(2N)$ generators

In the second case we make use of the identity¹ $V^T \Sigma_0 V = i\mathbb{1}$, for the unitary matrix $V = \frac{1}{\sqrt{2}}(\mathbb{1} + i\Sigma_0)$. Now we define

$$\begin{aligned} \tilde{T}^a &= V^{-1} T^a V \\ \tilde{X}^a &= V^{-1} X^a V \end{aligned} \quad (\text{C.6})$$

and find from Eq. (C.2)

$$V^T T^{aT} V^{-1T} V^T \Sigma_0 V = -V^T \Sigma_0 V V^{-1} T^a V \quad (\text{C.7})$$

which implies $\tilde{T}^{aT} = -\tilde{T}^a$. The $N(2N - 1)$ dimensional space of purely imaginary, antisymmetric matrices constitutes the Lie algebra of $SO(2N)$. As the generators of the unbroken symmetry are unitary equivalent to those of $SO(2N)$ the same is at least locally true for the corresponding unbroken symmetry group and $SO(2N)$. Analogously one finds for the coset generators $\tilde{X}^{aT} = \tilde{X}^a$ giving rise to $N(2N + 1) - 1$ coset generators $X^a = V^{-1} X^a V$, which together with the $N(2N - 1)$ unbroken generators constitute the $(2N)^2 - 1$ dimensional Lie algebra of $SU(2N)$ again. This procedure can be used to construct an explicit basis of the coset generators for the case of $N = 2$

$$\begin{aligned} X_1 &= \begin{pmatrix} \sigma_1 & 0 \\ 0 & \sigma_1 \end{pmatrix}, X_2 = \begin{pmatrix} \sigma_2 & 0 \\ 0 & -\sigma_2 \end{pmatrix}, X_3 = \begin{pmatrix} \sigma_3 & 0 \\ 0 & \sigma_3 \end{pmatrix}, X_4 = \begin{pmatrix} 0 & -i\mathbb{1} \\ i\mathbb{1} & 0 \end{pmatrix}, X_5 = \begin{pmatrix} 0 & -i\sigma_1 \\ i\sigma_1 & 0 \end{pmatrix}, \\ X_6 &= \begin{pmatrix} 0 & -i\sigma_3 \\ i\sigma_3 & 0 \end{pmatrix}, X_7 = \begin{pmatrix} 0 & \mathbb{1} \\ \mathbb{1} & 0 \end{pmatrix}, X_8 = \begin{pmatrix} 0 & \sigma_1 \\ \sigma_1 & 0 \end{pmatrix}, X_9 = \begin{pmatrix} 0 & \sigma_3 \\ \sigma_3 & 0 \end{pmatrix}, \end{aligned} \quad (\text{C.8})$$

¹This is a special case of the Takagi factorization, which states that a general complex symmetric matrix Σ_0 can be decomposed as $\Sigma_0 = V^T D V$ in terms of a unitary matrix V and a diagonal matrix D with entries given by the positive roots of the eigenvalues of the matrix $\Sigma_0^\dagger \Sigma_0$.

and for the simpler case of $N = 1$

$$X_1 = \begin{pmatrix} 0 & -i \\ i & 0 \end{pmatrix}, X_2 = \begin{pmatrix} 0 & 1 \\ 1 & 0 \end{pmatrix}. \quad (\text{C.9})$$

C.2 Coset Properties

In this section we consider some general properties of the cosets $SU(2N)/Sp(N)$ and $SU(2N)/SO(2N)$ and in particular of the two simplest non-trivial cases $SU(4)/Sp(2)$ and $SU(2)/SO(2)$. We start with some general remarks about the coset elements. Cartan's immersion theorem states that a general coset element Σ can be written as $\Sigma = U^T \Sigma_0 U$ for appropriately chosen $U \in SU(2N)$. This readily implies $\Sigma^\dagger \Sigma = 1$, $\det \Sigma = \det \Sigma_0 = 1$, $\Sigma^T = \pm \Sigma$, where the upper(lower) sign applies to $SU(2N)/Sp(N)$ ($SU(2N)/SO(2N)$). This means that the coset is formed by unitary, unimodular and antisymmetric (for $SU(2N)/Sp(N)$) or symmetric (for $SU(2N)/SO(2N)$) matrices. Furthermore note that Σ_0 together with $\Sigma_i = i\Sigma_0 X_i$ forms a basis of the complex vector space of (anti)symmetric $2N \times 2N$ matrices.

It turns out that in the two simplest cases $SU(4)/Sp(2)$ and $SU(2)/SO(2)$ the coset elements themselves can be parametrized by unit vectors i.e. $\Sigma = n_i \Sigma_i$, where $\Sigma_i = i\Sigma_0 X_i$ and $|\vec{n}| = 1$, which was shown for $SU(4)/Sp(2)$ in [158]. In fact since at least locally $SU(4)/Sp(2) \simeq SO(6)/SO(5)$ and $SU(2)/SO(2) \simeq SO(3)/SO(2)$ this is just the explicit expression of the well-known relation $SO(N)/SO(N-1) \simeq \mathcal{S}^{N-1}$.

To see this explicitly for $SU(2)/SO(2)$ and $SU(4)/Sp(2)$ we start from a general (anti)symmetric matrix Σ which we expand in terms of the basis of Σ_i i.e.

$$\Sigma = z_i \Sigma_i = (x_i + iy_i) \Sigma_i. \quad (\text{C.10})$$

Demanding unitarity leads to

$$\mathbb{1} = \Sigma^\dagger \Sigma = \mathbb{1} \sum_i |z_i|^2 + \sum_{1 \leq i < j} (x_i y_j - x_j y_i) i [X_i, X_j] \quad (\text{C.11})$$

Note that $i[X_i, X_j]$ either vanishes or is an unbroken generator. Only in the two cases from above all of them are linearly independent, which then implies $\sum_i |z_i|^2 = 1$ and $x_i y_j = x_j y_i$ for all $i \neq j$. This in turn implies $z_i = n_i e^{i\phi}$ with $\sum_i n_i^2 = 1$. In the mentioned cases one explicitly calculates the determinant and demanding unimodularity yields

$$1 = \det \Sigma = e^{2iN\phi}, \quad (\text{C.12})$$

which implies at least for the component containing Σ_0 that a general coset element can be represented in terms of a unit vector (n_i) as

$$\Sigma = n_i \Sigma_i. \quad (\text{C.13})$$

C.3 Transformation Properties of $\Psi^T \Sigma_i \Psi$

For the construction of effective models for 2-color QCD with fundamental quarks and QCD with quarks in the adjoint representation, it is instructive to consider the transformation properties of quark bilinears of the form $\Psi^T \Sigma_i \Psi$, for $\Sigma_i = i\Sigma_0 X_i$ as before, under enlarged flavor transformations $\Psi \rightarrow U\Psi$ and $U \in SU(2N_f)$. For $U = \exp(i\theta_a^X X_a + i\theta_a^T T_a)$ we find the infinitesimal transformation behavior

$$\Psi^T \Sigma_a \Psi \rightarrow \Psi^T \Sigma_a \Psi + i\theta_k^X \Psi^T (X_k^T \Sigma_a + \Sigma_a X_k) \Psi + i\theta_k^T \Psi^T (T_k^T \Sigma_a + \Sigma_a T_k) \Psi + \dots \quad (\text{C.14})$$

Employing the definition of Σ_i one finds $(X_k^T \Sigma_a + \Sigma_a X_k) = i\Sigma_0 X_k$, X_a and $(T_k^T \Sigma_a + \Sigma_a T_k) = i\Sigma_0 [X_a, T_k]$ and can now easily work out the infinitesimal transformation properties of $(\Psi^T \Sigma_i \Psi)$ using an explicit basis for the generators T_k and X_a :

1. $SU(4)/Sp(2) \simeq SO(6)/SO(5)$ ($\beta = 1, N_f = 2$):

$$\delta \begin{pmatrix} \Psi^T \Sigma_0 \Psi \\ \Psi^T \Sigma_1 \Psi \\ \Psi^T \Sigma_2 \Psi \\ \Psi^T \Sigma_3 \Psi \\ \Psi^T \Sigma_4 \Psi \\ \Psi^T \Sigma_5 \Psi \end{pmatrix} = i2i \begin{pmatrix} 0 & \theta_2^X & \theta_3^X & \theta_4^X & \theta_5^X & \theta_6^X \\ -\theta_1^X & 0 & -\theta_4^T & -\theta_3^T & \theta_{10}^T & \theta_9^T \\ -\theta_2^X & \theta_4^T & 0 & -\theta_2^T & \theta_7^T & -\theta_8^T \\ -\theta_3^X & \theta_3^T & \theta_2^T & 0 & -\theta_6^T & -\theta_5^T \\ -\theta_4^X & -\theta_{10}^T & -\theta_7^T & \theta_6^T & 0 & -\theta_1^T \\ -\theta_5^X & -\theta_9^T & \theta_8^T & \theta_5^T & \theta_1^T & 0 \end{pmatrix} \begin{pmatrix} \Psi^T \Sigma_0 \Psi \\ \Psi^T \Sigma_1 \Psi \\ \Psi^T \Sigma_2 \Psi \\ \Psi^T \Sigma_3 \Psi \\ \Psi^T \Sigma_4 \Psi \\ \Psi^T \Sigma_5 \Psi \end{pmatrix} \quad (\text{C.15})$$

This is the transformation law of a (complex) vector of $SO(6)$.

2. $SU(2)/SO(2) \simeq SO(3)/SO(2)$ ($\beta = 4, N_f = 1$):

$$\delta \begin{pmatrix} \Psi^T \Sigma_0 \Psi \\ \Psi^T \Sigma_1 \Psi \\ \Psi^T \Sigma_2 \Psi \end{pmatrix} = i2i \begin{pmatrix} 0 & \theta_1^X & \theta_2^X \\ -\theta_1^X & 0 & -\theta_1^T \\ -\theta_2^X & \theta_1^T & 0 \end{pmatrix} \begin{pmatrix} \Psi^T \Sigma_0 \Psi \\ \Psi^T \Sigma_1 \Psi \\ \Psi^T \Sigma_2 \Psi \end{pmatrix} \quad (\text{C.16})$$

This is the transformation law of a (complex) vector of $SO(3)$.

3. $SU(4)/SO(4) \simeq SO(6)/SO(4)$ ($\beta = 4, N_f = 2$):

$$\delta \begin{pmatrix} \Psi^T \Sigma_0 \Psi \\ \Psi^T \Sigma_1 \Psi \\ \Psi^T \Sigma_2 \Psi \\ \Psi^T \Sigma_3 \Psi \\ \Psi^T \Sigma_4 \Psi \\ \Psi^T \Sigma_5 \Psi \\ \Psi^T \Sigma_6 \Psi \\ \Psi^T \Sigma_7 \Psi \\ \Psi^T \Sigma_8 \Psi \\ \Psi^T \Sigma_9 \Psi \end{pmatrix} = i2i \begin{pmatrix} 0 & \theta_1^X & \theta_2^X & \theta_3^X & \theta_4^X & \theta_5^X & \theta_6^X & \theta_7^X & \theta_8^X & \theta_9^X \\ -\theta_1^X & 0 & -\theta_4^T & \theta_1^T & i\theta_5^X & i\theta_4^X & \theta_2^T & i\theta_8^X & i\theta_7^X & -\theta_6^T \\ -\theta_2^X & \theta_4^T & 0 & -\theta_5^T & -\theta_6^T & -i\theta_9^X & i\theta_8^X & -\theta_2^T & i\theta_6^X & -i\theta_5^T \\ -\theta_3^X & -\theta_1^T & \theta_5^T & 0 & i\theta_6^X & \theta_2^T & i\theta_4^X & i\theta_9^X & -\theta_6^T & i\theta_7^X \\ -\theta_4^X & i\theta_5^X & -\theta_6^T & i\theta_6^X & 0 & i\theta_1^X & i\theta_2^X & \theta_3^T & \theta_5^T & \theta_4^T \\ -\theta_5^X & i\theta_4^X & -i\theta_9^X & -\theta_2^T & i\theta_1^X & 0 & \theta_1^T & \theta_5^T & \theta_3^T & -i\theta_2^X \\ -\theta_6^X & -\theta_2^T & i\theta_8^X & i\theta_4^X & i\theta_3^X & -\theta_1^T & 0 & \theta_4^T & i\theta_2^X & \theta_3^T \\ -\theta_7^X & i\theta_8^X & \theta_2^T & i\theta_9^X & -\theta_3^T & -\theta_5^T & -\theta_4^T & 0 & i\theta_1^X & i\theta_3^X \\ -\theta_8^X & i\theta_7^X & i\theta_6^X & \theta_6^T & -\theta_5^T & -\theta_3^T & i\theta_2^X & i\theta_1^X & 0 & \theta_1^T \\ -\theta_9^X & \theta_6^T & -i\theta_5^X & i\theta_7^X & -\theta_4^T & -i\theta_2^X & -\theta_3^T & i\theta_3^X & -\theta_1^T & 0 \end{pmatrix} \begin{pmatrix} \Psi^T \Sigma_0 \Psi \\ \Psi^T \Sigma_1 \Psi \\ \Psi^T \Sigma_2 \Psi \\ \Psi^T \Sigma_3 \Psi \\ \Psi^T \Sigma_4 \Psi \\ \Psi^T \Sigma_5 \Psi \\ \Psi^T \Sigma_6 \Psi \\ \Psi^T \Sigma_7 \Psi \\ \Psi^T \Sigma_8 \Psi \\ \Psi^T \Sigma_9 \Psi \end{pmatrix} \quad (\text{C.17})$$

This is not the transformation law of simple vector and reiterates the fact that the $\beta = 4, N_f = 2$ case cannot be treated in terms of a simple vector model as the two cases discussed before but requires a matrix model due to the more complicated structure of the coset $SU(4)/SO(4)$.

D

Flow Equations for the (P)QMD Model

In this appendix we sketch the derivation of the flow equations for the (P)QMD model. In the first section we introduce massive energy projectors as a particularly convenient way of representing fermion propagators and evaluating the corresponding Dirac traces. In Section D.2 we discuss the flow equation for the effective potential for the PQMD model at zeroth order in the derivative expansion. Finally in Section D.3 we discuss the flow equations for the extended truncation introduced in Section 3.5.3.

D.1 Massive Energy Projectors

To conveniently handle expressions involving fermion propagators at finite chemical potential, it turns out to be useful to introduce the Euclidean analogues of the commonly used massive energy projectors [108]. Therefore we define

$$\Lambda_{\pm}(\vec{p}) = \frac{1}{2} \left(1 \pm \frac{\gamma^0(\mathbf{i}\vec{p} + M)}{E_p} \right) \quad \text{and} \quad \Lambda_{\pm}^{(M=0)}(\vec{p}) = \frac{1}{2} \left(1 \pm \frac{\mathbf{i}\gamma^0\vec{p}}{|\vec{p}|} \right), \quad (\text{D.1})$$

where $E_p = \sqrt{\vec{p}^2 + M^2}$. This allows us to write the Euclidean Dirac equation as

$$(\mathbf{i}\not{p} - \mu\gamma^0 + M) = \gamma^0 \sum_{j=\pm} (\mathbf{i}p_0 - \mu + jE_p)\Lambda_j. \quad (\text{D.2})$$

Furthermore one easily verifies that Λ_{\pm} are projection operators i.e. they satisfy $\Lambda_{\pm}\Lambda_{\pm} = \Lambda_{\pm}$, $\Lambda_{\pm}\Lambda_{\mp} = 0$ and $\Lambda_{+} + \Lambda_{-} = 1$. These projectors can now be used to conveniently invert matrices of the form

$$B^{-1}(p^{\mu}) = \begin{pmatrix} \mathbf{i}\not{p} - \mu\gamma^0 + M & \Delta\gamma^5 \\ -\Delta^*\gamma^5 & \mathbf{i}\not{p} + \mu\gamma^0 + M \end{pmatrix}, \quad (\text{D.3})$$

D. Flow Equations for the (P)QMD Model

as the inverse matrix can be written as

$$B(p^\mu) = \begin{pmatrix} B_{11}(p^\mu) & B_{12}(p^\mu) \\ B_{21}(p^\mu) & B_{22}(p^\mu) \end{pmatrix}, \quad (\text{D.4})$$

where

$$B_{11} = b_{11}^+ \Lambda_+ \gamma^0 + b_{11}^- \Lambda_- \gamma^0, \quad (\text{D.5})$$

$$B_{12} = b_{12}^+ \Lambda_+ \gamma^5 + b_{12}^- \Lambda_- \gamma^5, \quad (\text{D.6})$$

$$B_{21} = b_{21}^+ \Lambda_+ \gamma^5 + b_{21}^- \Lambda_- \gamma^5, \quad (\text{D.7})$$

$$B_{22} = b_{22}^+ \Lambda_+ \gamma^0 + b_{22}^- \Lambda_- \gamma^0, \quad (\text{D.8})$$

with coefficients b_{ij}^\pm given by

$$b_{11}^\pm = \frac{ip_0 + \mu \mp E_p}{(ip_0 - E_p^\pm)(ip_0 + E_p^\pm)}, \quad (\text{D.9})$$

$$b_{12}^\pm = \frac{\Delta}{(ip_0 - E_p^\pm)(ip_0 + E_p^\pm)}, \quad (\text{D.10})$$

$$b_{21}^\pm = \frac{-\Delta^*}{(ip_0 - E_p^\pm)(ip_0 + E_p^\pm)}, \quad (\text{D.11})$$

$$b_{22}^\pm = \frac{ip_0 - \mu \mp E_p}{(ip_0 - E_p^\pm)(ip_0 + E_p^\pm)}, \quad (\text{D.12})$$

D.2. Flow of the Effective Potential in the PQMD Model

where $E_p^\pm = \sqrt{(E_p \pm \mu)^2 + \Delta\Delta^*}$. Dirac traces can now be worked out easily using the expressions for Dirac traces involving combinations of projectors such as

$$\text{Tr}(\Lambda_\pm(\vec{p})\gamma^0\Lambda_\pm(\vec{q})\gamma^0) = \frac{1}{E_p E_q}(E_p E_q + M^2 - \vec{p}\vec{q}), \quad (\text{D.13})$$

$$\text{Tr}(\Lambda_\pm(\vec{p})\gamma^0\Lambda_\mp(\vec{q})\gamma^0) = \frac{1}{E_p E_q}(E_p E_q - M^2 + \vec{p}\vec{q}), \quad (\text{D.14})$$

$$\text{Tr}(\Lambda_\pm(\vec{p})\gamma^5\Lambda_\pm(\vec{q})\gamma^5) = \frac{1}{E_p E_q}(E_p E_q - M^2 + \vec{p}\vec{q}), \quad (\text{D.15})$$

$$\text{Tr}(\Lambda_\pm(\vec{p})\gamma^5\Lambda_\mp(\vec{q})\gamma^5) = \frac{1}{E_p E_q}(E_p E_q + M^2 - \vec{p}\vec{q}), \quad (\text{D.16})$$

$$\text{Tr}(\Lambda_\pm(\vec{p})\gamma^0\gamma^5\Lambda_\pm(\vec{q})\gamma^0\gamma^5) = \frac{1}{E_p E_q}(-E_p E_q + M^2 + \vec{p}\vec{q}), \quad (\text{D.17})$$

$$\text{Tr}(\Lambda_\pm(\vec{p})\gamma^0\gamma^5\Lambda_\mp(\vec{q})\gamma^0\gamma^5) = \frac{1}{E_p E_q}(-E_p E_q - M^2 - \vec{p}\vec{q}), \quad (\text{D.18})$$

$$\text{Tr}(\Lambda_\pm(\vec{p})\Lambda_\pm(\vec{q})) = \frac{1}{E_p E_q}(E_p E_q + M^2 + \vec{p}\vec{q}), \quad (\text{D.19})$$

$$\text{Tr}(\Lambda_\pm(\vec{p})\Lambda_\mp(\vec{q})) = \frac{1}{E_p E_q}(E_p E_q - M^2 - \vec{p}\vec{q}), \quad (\text{D.20})$$

$$\text{Tr}(\Lambda_\pm^{(M=0)}(\vec{p})\gamma^0\Lambda_\pm(\vec{q})\gamma^0) = 1 - \frac{\vec{p}\vec{q}}{|\vec{p}|E_q}, \quad (\text{D.21})$$

$$\text{Tr}(\Lambda_\pm^{(M=0)}(\vec{p})\gamma^0\Lambda_\mp(\vec{q})\gamma^0) = 1 + \frac{\vec{p}\vec{q}}{|\vec{p}|E_q}. \quad (\text{D.22})$$

D.2 Flow of the Effective Potential in the PQMD Model

Fermionic contributions

To obtain the flow equation for the effective potential we have to evaluate the right hand side of the flow equation for a constant field configuration here chosen as $(\bar{\phi}_i) = (\bar{\sigma}, \text{Re } \bar{\Delta}, \text{Im } \bar{\Delta}, \bar{\pi})^T = (\rho, \text{Re } \Delta, \text{Im } \Delta, \vec{0})^T$. For a general 3-momentum regulator

$$R_{k,F} = \begin{pmatrix} i\vec{p}r_{k,F} & 0 \\ 0 & i\vec{p}r_{k,F} \end{pmatrix} \quad (\text{D.23})$$

we find using the Ansatz (3.67)

$$(\Gamma_k^{(2,0)} + R_{k,F})|_{\phi=\bar{\phi}} = \begin{pmatrix} (ip_0 - \mu - i\frac{a_0}{2})\gamma^0 + i\vec{p}(1+r_{k,F}) + g\rho & g\Delta\gamma^5 \\ -g\Delta^*\gamma^5 & (ip_0 + \mu - i\frac{a_0}{2})\gamma^0 + i\vec{p}(1+r_{k,F}) + g\rho \end{pmatrix} \quad (\text{D.24})$$

and obviously

$$\partial_t R_{k,F} = \begin{pmatrix} i\vec{p}\partial_t r_{k,F} & 0 \\ 0 & i\vec{p}\partial_t r_{k,F} \end{pmatrix} = \partial_t r_{k,F} |\vec{p}| (\Lambda_-^{(M=0)}\gamma^0 - \Lambda_+^{(M=0)}\gamma^0). \quad (\text{D.25})$$

D. Flow Equations for the (P)QMD Model

We can now use Eq. (D.4) to invert Eq. (D.24) and easily evaluate the Dirac traces using Eq. (D.21) and Eq. (D.22), which yields the following expression for the fermionic contribution to the flow of the effective potential

$$\begin{aligned}
\partial_t U_{k,F} &= -\frac{1}{\mathcal{V}} \text{Tr} \left[(\Gamma^{(2,0)} + R_{k,F})^{-1} \partial_t R_{k,F} \right] \\
&= -4N_f \int_p \bar{p}^2 (1 + r_{k,F}) \partial_t r_{k,F} \left(\frac{1 + \frac{\mu}{E}}{(\nu_n - \frac{a_0}{2} + iE^+)(\nu_n - \frac{a_0}{2} - iE^+)} + \frac{1 - \frac{\mu}{E}}{(\nu_n - \frac{a_0}{2} + iE^-)(\nu_n - \frac{a_0}{2} - iE^-)} \right) \\
&= -2N_f \int \frac{d^3 p}{(2\pi)^3} \bar{p}^2 (1 + r_{k,F}) \partial_t r_{k,F} \sum_{\pm} \left(1 \pm \frac{\mu}{E} \right) \frac{1}{E_{\pm}} \frac{\sinh(\beta E_{\pm})}{\Phi + \cosh(\beta E_{\pm})},
\end{aligned} \tag{D.26}$$

where $E = \sqrt{\bar{p}^2(1 + r_{k,F})^2 + h^2 \rho^2}$, $E^{\pm} = \sqrt{(E \pm \mu)^2 + h^2 |\Delta|^2}$ and \mathcal{V} denotes the spacetime volume. For the sharp 3-momentum regulator $r_{k,F} = \left(-1 + \sqrt{\frac{k^2}{\bar{p}^2}}\right) \Theta(k^2 - \bar{p}^2)$, one recovers the fermionic contribution listed in Eq. (3.68).

Bosonic contributions

Again evaluating the RHS of the flow equation for the Ansatz from (3.67) for a constant field configuration $(\bar{\phi}_i) = (\bar{\sigma}, \text{Re } \bar{\Delta}, \text{Im } \bar{\Delta}, \vec{\pi})^T = (\rho, d, 0, \vec{0})^T$ yields

$$(\Gamma^{(0,2)} + R_k)_{ij} |_{\phi=\bar{\phi}} = \begin{pmatrix} A & & 0 \\ & (p_0^2 + \bar{p}^2(1 + r_{k,B}) + 2U_{k,\rho}) \mathbf{1}_{3 \times 3} & \\ 0 & & \end{pmatrix}, \tag{D.27}$$

using a 3-momentum regulator

$$R_{k,B} = \mathbf{1}_{6 \times 6} \bar{p}^2 r_{k,B} \tag{D.28}$$

with

$$A = \begin{pmatrix} p_0^2 + \bar{p}^2(1 + r_{k,B}) + 2U_{k,\rho} + 4U_{k,\rho\rho} \rho^2 & & 4U_{k,\rho d} \rho d & & 0 \\ & 4U_{k,\rho d} \rho d & & p_0^2 + \bar{p}^2(1 + r_{k,B}) + 2U_{k,d} + 4U_{k,dd} - 4\mu^2 & -4p_0 \mu \\ 0 & & 0 & 4p_0 \mu & p_0^2 + \bar{p}^2(1 + r_{k,B}) + 2U_{k,d} - 4\mu^2 \end{pmatrix}. \tag{D.29}$$

Using the bosonic regulator $R_{k,B}$ from Eq. (D.28) we end up with the following bosonic contribution to the flow of the effective potential:

$$\begin{aligned}
\partial_t U_{k,B} &= \frac{1}{2\mathcal{V}} \text{Tr} \left[(\Gamma_{k,B}^{(2)} + R_{k,B})^{-1} \partial_t R_{k,B} \right] \\
&= \frac{1}{2} \int_p \bar{p}^2 \partial_t r_{k,B} \left(\frac{3}{p_0^2 + E_{\pi}^2} + \text{Tr } A^{-1} \right),
\end{aligned} \tag{D.30}$$

where $E_{\pi} = \sqrt{\bar{p}^2(1 + r_{k,B}) + 2U_{k,\rho}}$. All Matsubara sums can still be evaluated analytically by noting that $\text{Tr } A^{-1}$ is a rational function in p_0^2 with quadratic numerator and cubic denominator. It is particularly convenient to employ the sharp 3-momentum

regulator $r_{k,B} = (\frac{k^2}{\bar{p}^2} - 1)\Theta(k^2 - \bar{p}^2)$ for which the spatial momentum integration becomes trivial. In this case one finds

$$\partial_t U_{k,B} = \frac{k^5 T}{6\pi^2} \sum_n \left(\frac{3}{\omega_n^2 + k^2 + 2U_{k,\rho}} + \frac{3(\omega_n^2)^2 + \alpha_1 \omega_n^2 + \alpha_0}{(\omega_n^2)^3 + \beta_2 (\omega_n^2)^2 + \beta_1 \omega_n^2 + \beta_0} \right) \quad (\text{D.31})$$

with coefficients α_i, β_i depending on chemical potential and derivatives of the effective potential listed explicitly below. Denoting the roots of the denominator by $\omega_{n,0}^2 = -z_i^2$ for $i = 1, 2, 3$ one can evaluate all Matsubara sums analytically using standard methods and obtains the corresponding bosonic contribution to Eq. (3.68).

For completeness we list the coefficients α_i and β_i appearing in Eq. (D.31)

$$\begin{aligned} \alpha_0 = & 3k^4 + 4k^2(-4\mu^2 + 2U_{k,d} + 2d^2U_{k,dd} + U_{k,\rho} + 2\rho^2U_{k,\rho\rho}) \\ & + 4(4\mu^4 + U_{k,d}^2 + 2U_{k,d}(d^2U_{k,dd} + U_{k,\rho} + 2\rho^2U_{k,\rho\rho}) - \\ & 4\mu^2(U_{k,d} + d^2U_{k,dd} + U_{k,\rho} + 2\rho^2U_{k,\rho\rho}) \\ & + 2d^2(U_{k,dd}U_{k,\rho} - 2\rho^2U_{k,\rho d}^2 + 2\rho^2U_{k,dd}U_{k,\rho\rho})) \end{aligned} \quad (\text{D.32})$$

$$\alpha_1 = 6k^2 + 8U_{k,d} + 8d^2U_{k,dd} + 4U_{k,\rho} + 8\rho^2U_{k,\rho\rho} \quad (\text{D.33})$$

$$\begin{aligned} \beta_0 = & (k^2 - 4\mu^2 + 2U_{k,d})(k^4 + 2k^2(-2\mu^2 + U_{k,d} + 2d^2U_{k,dd} + U_{k,\rho} + 2\rho^2U_{k,\rho\rho}) \\ & + 4(-2\mu^2U_{k,\rho} + U_{k,d}U_{k,\rho} + 2d^2U_{k,dd}U_{k,\rho} - 4d^2\rho^2U_{k,\rho d}^2 \\ & + 2\rho^2(-2\mu^2 + U_{k,d} + 2d^2U_{k,dd})U_{k,\rho\rho})) \end{aligned} \quad (\text{D.34})$$

$$\begin{aligned} \beta_1 = & 3k^4 + 4k^2(2U_{k,d} + 2d^2U_{k,dd} + U_{k,\rho} + 2\rho^2U_{k,\rho\rho}) \\ & + 4(4\mu^4 + U_{k,d}^2 - 4\mu^2(U_{k,d} + d^2U_{k,dd} - U_{k,\rho} - 2\rho^2U_{k,\rho\rho}) \\ & + 2U_{k,d}(d^2U_{k,dd} + U_{k,\rho} + 2\rho^2U_{k,\rho\rho}) \\ & + 2d^2(U_{k,dd}U_{k,\rho} - 2\rho^2U_{k,\rho d}^2 + 2\rho^2U_{k,dd}U_{k,\rho\rho})) \end{aligned} \quad (\text{D.35})$$

$$\beta_2 = 3k^2 + 8\mu^2 + 4U_{k,d} + 4d^2U_{k,dd} + 2U_{k,\rho} + 4\rho^2U_{k,\rho\rho}. \quad (\text{D.36})$$

D.3 Improved Truncation

In this appendix we sketch the derivation of the flow equations for the improved QMD model truncation introduced in Section 3.5.3. The flow equation for the effective potential is obtained as in the previous section by evaluating the flow equation for a constant field configuration $(\tilde{\phi}_i) = (\tilde{\sigma}, \tilde{\Delta}_R, \tilde{\Delta}_I, \tilde{\vec{\pi}})^T = (\tilde{\rho}, \tilde{d}, 0, \vec{0})^T$. The flow equations for wavefunction renormalization factors and Yukawa couplings are most conveniently obtained following [49]. Therefore one decomposes the scale-dependent inverse propagator into a field-independent part ($\Gamma_0^{(2)}$) containing propagators and cutoff functions and a field-dependent part ($\Delta\Gamma^{(2)}$) i.e.

$$\Gamma_k^{(2)} + R_k = \Gamma_0^{(2)} + \Delta\Gamma^{(2)}. \quad (\text{D.37})$$

D. Flow Equations for the (P)QMD Model

Now one formally expands the flow equation Eq. (2.17)

$$\begin{aligned} \partial_t \Gamma_k &= \frac{1}{2} \tilde{\partial}_t \text{STr} \left[\Gamma_0^{(2)-1} \Delta \Gamma^{(2)} \right] - \frac{1}{2} \cdot \frac{1}{2} \tilde{\partial}_t \text{STr} \left[\left(\Gamma_0^{(2)-1} \Delta \Gamma^{(2)} \right)^2 \right] \\ &\quad + \frac{1}{2} \cdot \frac{1}{3} \tilde{\partial}_t \text{STr} \left[\left(\Gamma_0^{(2)-1} \Delta \Gamma^{(2)} \right)^3 \right] + \dots, \end{aligned} \quad (\text{D.38})$$

where $\tilde{\partial}_t = \partial_t R_k \frac{\partial}{\partial R_k}$ is a formal derivative which acts on the regulator only and the dots denote field-independent parts and higher order terms in the expansion. The formulation (D.38) is particularly convenient because powers of $(\Gamma_0^{(2)-1} \Delta \Gamma^{(2)})$ can be worked out as simple matrix multiplications. The flow of the fermionic wavefunction renormalization Z_ψ is now obtained via the projection

$$\begin{aligned} \delta(0) \partial_t Z_\psi &= \frac{(-i)}{(d-1)d_\gamma N_f N_c} \text{Tr}_{\text{D,f,NG}} \left[\gamma^i \frac{\partial}{\partial p^i} \frac{\vec{\delta}}{\delta \tilde{\Psi}(p)} \partial_t \Gamma_k \frac{\overleftarrow{\delta}}{\delta \tilde{\Psi}(q)} \right] \Big|_{p=q=0} \\ &= -\frac{1}{4} \frac{(-i)}{(d-1)d_\gamma N_f N_c} \text{Tr}_{\text{D,f,NG}} \left[\gamma^i \frac{\partial}{\partial p^i} \frac{\vec{\delta}}{\delta \tilde{\Psi}(p)} \tilde{\partial}_t \text{STr} \left[\left(\Gamma_0^{(2)-1} \Delta \Gamma^{(2)} \right)^2 \right] \frac{\overleftarrow{\delta}}{\delta \tilde{\Psi}(q)} \right] \Big|_{p=q=0}, \end{aligned} \quad (\text{D.39})$$

where the outer trace runs over Dirac, flavor and Nambu-Gorkov space. The bosonic wavefunction renormalization factors Z_r and Z_d are calculated via

$$\delta(0) \partial Z_r = \frac{\partial}{\partial p^2} \frac{\delta^2 \partial_t \Gamma_k}{\delta \tilde{\pi}_1(-p) \delta \tilde{\pi}_1(q)} \Big|_{p=q=0} = -\frac{1}{4} \frac{\partial}{\partial p^2} \frac{\delta^2 \tilde{\partial}_t \text{STr} \left[\left(\Gamma_0^{(2)-1} \Delta \Gamma^{(2)} \right)^2 \right]}{\delta \tilde{\pi}_1(-p) \delta \tilde{\pi}_1(q)} \Big|_{p=q=0} \quad (\text{D.40})$$

$$\delta(0) \partial Z_d = \frac{\partial}{\partial p^2} \frac{\delta^2 \partial_t \Gamma_k}{\delta \tilde{\Delta}_I(-p) \delta \tilde{\Delta}_I(q)} \Big|_{p=q=0} = -\frac{1}{4} \frac{\partial}{\partial p^2} \frac{\delta^2 \tilde{\partial}_t \text{STr} \left[\left(\Gamma_0^{(2)-1} \Delta \Gamma^{(2)} \right)^2 \right]}{\delta \tilde{\Delta}_I(-p) \delta \tilde{\Delta}_I(q)} \Big|_{p=q=0} \quad (\text{D.41})$$

We stress the importance of extracting the flow of the wavefunction renormalization factors in both cases from the Goldstone modes as only this ensures that both coincide for $\mu = 0$. The flow of the Yukawa couplings h_r and h_d is obtained from

$$\begin{aligned} \delta(0) \partial_t h_r &= \frac{(-i)}{N_f d_\gamma N_c} \text{Tr}_{\text{D,f,NG}} \left[\tau_1 \gamma^5 \hat{P}_r \frac{\vec{\delta}}{\delta \tilde{\Psi}(p)} \frac{\vec{\delta}}{\delta \tilde{\pi}_1(q)} \partial_t \Gamma_k \frac{\overleftarrow{\delta}}{\delta \tilde{\Psi}(r)} \right] \Big|_{p=q=r=0} \\ &= \frac{1}{6} \frac{(-i)}{N_f d_\gamma N_c} \text{Tr}_{\text{D,f,NG}} \left[\tau_1 \gamma^5 \hat{P}_r \frac{\vec{\delta}}{\delta \tilde{\Psi}(p)} \frac{\vec{\delta}}{\delta \tilde{\pi}_1(q)} \tilde{\partial}_t \text{STr} \left[\left(\Gamma_0^{(2)-1} \Delta \Gamma^{(2)} \right)^3 \right] \frac{\overleftarrow{\delta}}{\delta \tilde{\Psi}(r)} \right] \Big|_{p=q=r=0} \end{aligned} \quad (\text{D.42})$$

D. Flow Equations for the (P)QMD Model

where

$$P_s = \hat{p}_0^2 + x(1 + r_{k,Br}) + (2U_r + 4U_{rr}\rho^2)k^{-2}, \quad (\text{D.47})$$

$$P_\pi = \hat{p}_0^2 + x(1 + r_{k,Br}) + 2U_r k^{-2}, \quad (\text{D.48})$$

$$P_{d1} = \hat{p}_0^2 + x(1 + r_{k,Bd}) + (2U_d + 4U_{dd}d^2)k^{-2} - 4\hat{\mu}^2, \quad (\text{D.49})$$

$$P_{d2} = \hat{p}_0^2 + x(1 + r_{k,Bd}) + 2U_d k^{-2} - 4\hat{\mu}^2, \quad (\text{D.50})$$

$$P_{dd} = -4\hat{p}_0\hat{\mu}, \quad (\text{D.51})$$

$$P_{ds} = 4U_{rd}\rho dk^{-2}, \quad (\text{D.52})$$

$$\det_B = P_s(P_{dd}^2 + P_{d1}P_{d2}) - P_{d2}P_{ds}^2, \quad (\text{D.53})$$

$$(\text{D.54})$$

and fermion propagators

$$b_{11}^\pm = -\frac{i\hat{p}_0 + \hat{\mu} \mp \hat{\epsilon}_x}{\hat{p}_0^2 + \hat{E}_x^{\mp 2}}, \quad b_{12}^\pm = -\frac{h_d\Delta k^{-1}}{\hat{p}_0^2 + \hat{E}_x^{\mp 2}}, \quad b_{21}^\pm = -\frac{-h_d\Delta^* k^{-1}}{\hat{p}_0^2 + \hat{E}_x^{\pm 2}}, \quad b_{22}^\pm = -\frac{i\hat{p}_0 - \hat{\mu} \mp \hat{\epsilon}_x}{\hat{p}_0^2 + \hat{E}_x^{\pm 2}}, \quad (\text{D.55})$$

where

$$\hat{\epsilon}_x = \sqrt{x(1 + r_{k,F})^2 + h_r^2\rho^2 k^{-2}}, \quad \hat{\epsilon}_x^\pm = \hat{\epsilon}_x \pm \hat{\mu}, \quad \hat{E}_x^\pm = \sqrt{\hat{\epsilon}_x^{\pm 2} + h_d^2 d^2 k^{-2}} \quad (\text{D.56})$$

and

$$\tilde{b}_{ij}^\pm = \frac{b_{ij}^\pm}{\hat{\epsilon}_x}, \quad \check{b}_{ij}^\pm = \frac{b_{ij}^\pm(1 + r_{k,F})}{\hat{\epsilon}_x}. \quad (\text{D.57})$$

Effective potential

The flow equation for the effective potential evaluated at fixed renormalized fields ρ^2 and d^2 is given by

$$\partial_t U_k |_{\rho^2, d^2} = \partial_t U_{k,B} |_{\tilde{\rho}^2, \tilde{d}^2} + \partial_t U_{k,F} |_{\tilde{\rho}^2, \tilde{d}^2} + \eta_r \rho^2 U_r + \eta_d d^2 U_d, \quad (\text{D.58})$$

where the fermionic/bosonic contributions generalize the expression from the simple truncation discussed in the previous section

$$\begin{aligned} \partial_t U_{k,B} |_{\tilde{\rho}, \tilde{d}} = v_{d-1} k^d \hat{T} \sum_{\hat{p}_0} \int dx x^{\frac{d-1}{2}} [(\partial_t r_{k,Br} - \eta_r r_{k,Br})(N_B P_\pi^{-1} + A_{11}) \\ + (\partial_t r_{k,Bd} - \eta_d r_{k,Bd})(A_{22} + A_{33})] \end{aligned} \quad (\text{D.59})$$

$$\partial_t U_{k,F} |_{\tilde{\rho}, \tilde{d}} = -4N_c N_f \frac{d_\gamma}{4} v_{d-1} k^d \hat{T} \sum_{\hat{p}_0} \int dx x^{\frac{d-1}{2}} (\partial_t r_{k,F} - \eta_\psi r_{k,F})(1 + r_{k,F}) \sum_{\pm} \frac{1 \pm \frac{\hat{\mu}}{\hat{\epsilon}_x}}{\hat{p}_0^2 + \hat{E}_x^{\pm 2}} \quad (\text{D.60})$$

Bosonic anomalous dimensions

The bosonic anomalous dimensions receive contributions from a fermionic and a bosonic loop diagram, i.e. $\eta_{r/d} = \eta_{r/d}^{\text{ferm}} + \eta_{r/d}^{\text{bos}}$, where the fermionic contributions read explicitly

$$\begin{aligned} \eta_r^{\text{ferm}} = & \frac{N_c N_f}{d-1} h_r^2 2v_{d-1} k^{d-4} \frac{d_\gamma}{4} \hat{T} \sum_{\hat{p}_0} \tilde{\partial}_t \int dx \left[\right. \\ & - x^{\frac{d-1}{2}} \sum_{\pm} [(b_{11}^{\pm'})^2 + (b_{22}^{\pm'})^2 + b_{11}^{\pm'} b_{11}^{\mp'} + b_{22}^{\pm'} b_{22}^{\mp'} + 2b_{12}^{\pm'} b_{21}^{\pm'} + 2b_{12}^{\pm'} b_{21}^{\mp'}] \\ & + h_r^2 \rho^2 k^{-2} x^{\frac{d-1}{2}} \sum_{\pm} [(\tilde{b}_{11}^{\pm'})^2 + (\tilde{b}_{22}^{\pm'})^2 - \tilde{b}_{11}^{\pm'} \tilde{b}_{11}^{\mp'} - \tilde{b}_{22}^{\pm'} \tilde{b}_{22}^{\mp'} - 2\tilde{b}_{12}^{\pm'} \tilde{b}_{21}^{\pm'} + 2\tilde{b}_{12}^{\pm'} \tilde{b}_{21}^{\mp'}] \\ & \left. + x^{\frac{d+1}{2}} \sum_{\pm} [(\check{b}_{11}^{\pm'})^2 + (\check{b}_{22}^{\pm'})^2 - \check{b}_{11}^{\pm'} \check{b}_{11}^{\mp'} - \check{b}_{22}^{\pm'} \check{b}_{22}^{\mp'} - 2\check{b}_{12}^{\pm'} \check{b}_{21}^{\pm'} + 2\check{b}_{12}^{\pm'} \check{b}_{21}^{\mp'}] \right] \end{aligned} \quad (\text{D.61})$$

and

$$\begin{aligned} \eta_d^{\text{ferm}} = & \frac{N_c N_f}{d-1} h_d^2 2v_{d-1} k^{d-4} \frac{d_\gamma}{4} \hat{T} \sum_{\hat{p}_0} \tilde{\partial}_t \int dx \left[\right. \\ & + x^{\frac{d-1}{2}} \sum_{\pm} [(b_{12}^{\pm'})^2 + (b_{21}^{\pm'})^2 + b_{12}^{\pm'} b_{12}^{\mp'} + b_{21}^{\pm'} b_{21}^{\mp'} - 2b_{11}^{\pm'} b_{22}^{\pm'} - 2b_{11}^{\pm'} b_{22}^{\mp'}] \\ & + h_r^2 \rho^2 k^{-2} x^{\frac{d-1}{2}} \sum_{\pm} [(\tilde{b}_{12}^{\pm'})^2 + (\tilde{b}_{21}^{\pm'})^2 - \tilde{b}_{12}^{\pm'} \tilde{b}_{12}^{\mp'} - \tilde{b}_{21}^{\pm'} \tilde{b}_{21}^{\mp'} + 2\tilde{b}_{11}^{\pm'} \tilde{b}_{22}^{\pm'} - 2\tilde{b}_{11}^{\pm'} \tilde{b}_{22}^{\mp'}] \\ & \left. + x^{\frac{d+1}{2}} \sum_{\pm} [(\check{b}_{12}^{\pm'})^2 + (\check{b}_{21}^{\pm'})^2 - \check{b}_{12}^{\pm'} \check{b}_{12}^{\mp'} - \check{b}_{21}^{\pm'} \check{b}_{21}^{\mp'} + 2\check{b}_{11}^{\pm'} \check{b}_{22}^{\pm'} - 2\check{b}_{11}^{\pm'} \check{b}_{22}^{\mp'}] \right], \end{aligned} \quad (\text{D.62})$$

and the bosonic contributions are given by

$$\begin{aligned} \eta_r^{\text{bos}} = & -\frac{32}{d-1} 2v_{d-1} k^{d-6} \hat{T} \sum_{\hat{p}_0} \tilde{\partial}_t \int dx x^{\frac{d-1}{2}} [U_{rr}^2 \rho^2 A'_{11} P_\pi^{-1'} \\ & + 2U_{rr} U_{rd} \rho d A'_{12} P_\pi^{-1'} + U_{rd}^2 d^2 A'_{22} P_\pi^{-1'}] \end{aligned} \quad (\text{D.63})$$

and

$$\begin{aligned} \eta_d^{\text{bos}} = & -\frac{16}{d-1} 2v_{d-1} k^{d-6} \hat{T} \sum_{\hat{p}_0} \tilde{\partial}_t \int dx x^{\frac{d-1}{2}} [d^2 U_{dd}^2 (A'_{22} - A'_{23})^2 \\ & + 2d\rho U_{dd} U_{rd} (A'_{13} A'_{23} + A'_{12} A'_{33}) + 2\rho^2 U_{rd}^2 (A'_{13}{}^2 + A'_{11} A'_{33})]. \end{aligned} \quad (\text{D.64})$$

D. Flow Equations for the (P)QMD Model

Fermionic anomalous dimension

The fermionic anomalous dimension is only driven by a fermionic loop diagram and is explicitly given by

$$\eta_\psi = \frac{1}{4} \frac{1}{d-1} 2v_{d-1} k^{d-4} \frac{d_\gamma}{4} \hat{T} \sum_{\hat{p}_0} \tilde{\partial}_t \int dx x^{\frac{d-1}{2}} (1 + r_{k,F}) \hat{\epsilon}_x^{-1} \left[h_r^2 (A'_{11} + N_B P_\pi^{-1}) + h_d^2 (A'_{22} + A'_{33}) (b_{11}^+ - b_{11}^- + b_{22}^+ - b_{22}^-) + 2i h_d^2 A'_{23} (b_{11}^+ - b_{11}^- - b_{22}^+ + b_{22}^-) \right]. \quad (\text{D.65})$$

Yukawa couplings

The flow of the Yukawa couplings receives contributions from two loop diagrams involving both fermions and bosons,

$$\partial_t h_r = (\eta_\psi + \frac{1}{2} \eta_r) h_r + \partial_t h_r^{\text{1st term}} + \partial_t h_r^{\text{2nd term}} \quad (\text{D.66})$$

$$\partial_t h_d = (\eta_\psi + \frac{1}{2} \eta_d) h_d + \partial_t h_d^{\text{1st term}} + \partial_t h_d^{\text{2nd term}}. \quad (\text{D.67})$$

$$\begin{aligned} \partial_t h_r^{\text{1st term}} = & 2v_{d-1} k^{d-5} \frac{d_\gamma}{4} \hat{T} \sum_{\hat{p}_0} \tilde{\partial}_t \int dx x^{\frac{d-3}{2}} \left[\right. \\ & \frac{2h_r^3 \rho}{k \hat{\epsilon}_x} [A_{11} U_{rr} \rho + A_{12} U_{rd} d] P_\pi^{-1} (b_{11}^+ - b_{11}^- + b_{22}^+ - b_{22}^-) \\ & \left. + 2h_r h_d [A_{21} U_{rr} \rho + A_{22} U_{rd} d] P_\pi^{-1} (-b_{12}^+ - b_{12}^- + b_{21}^+ + b_{21}^-) \right] \end{aligned} \quad (\text{D.68})$$

$$\begin{aligned} \partial_t h_d^{\text{1st term}} = & 2v_{d-1} k^{d-5} \frac{d_\gamma}{4} \hat{T} \sum_{\hat{p}_0} \tilde{\partial}_t \int dx x^{\frac{d-3}{2}} \left[\right. \\ & \frac{i h_r^2 h_d \rho}{k \hat{\epsilon}_x} [(A_{13} A_{22} - A_{23} A_{12}) d U_{dd} + (A_{13} A_{12} - A_{23} A_{11}) \rho U_{rd}] (b_{11}^+ - b_{11}^- - b_{22}^+ + b_{22}^-) \\ & + \frac{h_r^2 h_d \rho}{k \hat{\epsilon}_x} [(A_{13} A_{23} + A_{12} A_{33}) d U_{dd} + (A_{13}^2 + A_{11} A_{33}) \rho U_{rd}] (b_{11}^+ - b_{11}^- + b_{22}^+ - b_{22}^-) \\ & \left. + h_d^2 [(A_{23}^2 + A_{22} A_{33}) d U_{dd} + (A_{13} A_{23} + A_{12} A_{33}) \rho U_{rd}] (-b_{12}^+ - b_{12}^- + b_{21}^+ + b_{21}^-) \right] \end{aligned} \quad (\text{D.69})$$

$$\begin{aligned}
 \partial_t h_r^{\text{2nd term}} &= 2v_{d-1} k^{d-4} \frac{d_\gamma}{4} \hat{T} \sum_{\hat{p}_0} \tilde{\partial}_t \int dx x^{\frac{d-3}{2}} \left[\right. \\
 &\quad - (h_r^3 [A_{11} + (N_B - 2) P_\pi^{-1}] + h_r h_d^2 [A_{22} + A_{33}]) \sum_{\pm} [b_{11}^\pm b_{11}^\mp + b_{22}^\pm b_{22}^\mp + 2b_{12}^\pm b_{21}^\pm] \\
 &\quad + \frac{2i h_r^3 h_d A_{13} \rho}{k \hat{\epsilon}_x} (b_{21}^+ b_{11}^+ - b_{21}^- b_{11}^- - b_{22}^+ b_{21}^- + b_{22}^- b_{21}^+ - b_{11}^+ b_{12}^- + b_{11}^- b_{12}^+ + b_{12}^+ b_{22}^+ - b_{12}^- b_{22}^-) \\
 &\quad \left. + 2i h_d^2 h_r A_{23} \sum_{\pm} [b_{11}^\pm b_{11}^\mp - b_{22}^\pm b_{22}^\mp] \right]
 \end{aligned} \tag{D.70}$$

$$\begin{aligned}
 \partial_t h_d^{\text{2nd term}} &= 2v_{d-1} k^{d-4} \frac{d_\gamma}{4} \hat{T} \sum_{\hat{p}_0} \tilde{\partial}_t \int dx x^{\frac{d-3}{2}} \left[\right. \\
 &\quad + [h_d h_r^2 (A_{11} + N_B P_\pi^{-1}) + h_d^3 (A_{22} - A_{33})] \sum_{\pm} [(b_{21}^\pm)^2 + (b_{12}^\pm)^2 - 2b_{11}^\pm b_{22}^\mp] \\
 &\quad \left. + \frac{2i h_r^2 h_d^2 A_{13} \rho}{k \hat{\epsilon}_x} (b_{12}^+ b_{11}^+ - b_{12}^- b_{11}^- + b_{21}^+ b_{22}^+ - b_{21}^- b_{22}^- + b_{11}^+ b_{21}^- - b_{11}^- b_{21}^+ + b_{22}^+ b_{21}^- - b_{22}^- b_{21}^+) \right]
 \end{aligned} \tag{D.71}$$

Analytical limits

Despite of the rather complex structure of these equations one can verify that the expressions satisfy several important consistency conditions. Firstly, one easily verifies that all expressions are manifestly real using $(b_{11}^\pm)^* = -b_{22}^\mp$ and $(b_{12}^\pm)^* = -b_{21}^\mp$.

The second cross check involves the $d = 0$ limit. This implies in particular that $b_{ij}^\pm = 0$ for $i \neq j$ and the expressions for b_{ii}^\pm simplify accordingly. For an $SO(6)$ symmetric potential, setting in addition the diquark coupling to the chemical potential to zero which corresponds to $P_{dd} = 0$, one has $A_{11} = P_s^{-1}$ and $A_{ii} = P_\pi^{-1}$ for $i > 1$. In this case the flow equations have to reduce to the standard quark-meson model flow equations with $N_B + 2$ pions. These are given in the literature for the 1-flavor case at finite temperature [159, 110] and for the two flavor case at zero temperature for a 4d regulator in [42].

The last check is the case of zero chemical potential where one has to recover the full enlarged $SU(4)$ flavor symmetry, which implies that $\eta_r = \eta_d$ and $\partial_t h_r = \partial_t h_d$. This limit can be checked explicitly for the expression given above.

D. Flow Equations for the (P)QMD Model

Employing sharp 3-momentum regulators

For the sharp 3-momentum regulators

$$r_{k,Br} = \left(\frac{1}{x} - 1 \right) \Theta(1-x), \quad (\text{D.72})$$

$$r_{k,Bd} = \left(\frac{1}{x} - 1 \right) \Theta(1-x), \quad (\text{D.73})$$

$$r_{k,F} = \left(\frac{1}{\sqrt{x}} - 1 \right) \Theta(1-x), \quad (\text{D.74})$$

the formal derivatives acting on bosonic/fermionic fields read

$$\tilde{\partial}_t|_{Br} = \left(\frac{2}{x} - \eta_r \left(\frac{1}{x} - 1 \right) \right) \Theta(1-x) \frac{\partial}{\partial r_{k,Br}}, \quad (\text{D.75})$$

$$\tilde{\partial}_t|_{Bd} = \left(\frac{2}{x} - \eta_d \left(\frac{1}{x} - 1 \right) \right) \Theta(1-x) \frac{\partial}{\partial r_{k,Bd}}, \quad (\text{D.76})$$

$$\tilde{\partial}_t|_F = \left(\frac{1}{\sqrt{x}} - \eta_\psi \left(\frac{1}{\sqrt{x}} - 1 \right) \right) \Theta(1-x) \frac{\partial}{\partial r_{k,F}}. \quad (\text{D.77})$$

In particular this regulator choice allows to evaluate all momentum integrals analytically. The same applies in principle to the remaining Matsubara sums, although a numerical evaluation might turn out to be advantageous due to the rather complex structure of the equations.

Bibliography

- [1] N. Strodthoff, B.-J. Schaefer, and L. von Smekal, “Quark-meson-diquark model for two-color QCD,” *Phys.Rev.* **D85** (2012) 074007, [arXiv:1112.5401](#) [[hep-ph](#)].
- [2] K. Kamikado, N. Strodthoff, L. von Smekal, and J. Wambach, “Fluctuations in the quark-meson model for QCD with isospin chemical potential,” [arXiv:1207.0400](#) [[hep-ph](#)].
- [3] N. Strodthoff, S. Edwards, and L. von Smekal, “SU(3) Deconfinement in (2+1)d from Twisted Boundary Conditions and Self-Duality,” *PoS LATTICE2010* (2010) 288, [arXiv:1012.0723](#) [[hep-lat](#)].
- [4] L. von Smekal, S. Edwards, and N. Strodthoff, “Universal Aspects of Deconfinement: Interfaces, Flux Tubes and Self-Duality in 2+1 Dimensions,” *PoS LATTICE2010* (2010) 292, [arXiv:1012.0408](#) [[hep-lat](#)].
- [5] D. Gross, “The discovery of asymptotic freedom and the emergence of QCD,” *Proc.Nat.Acad.Sci.* **102** (2005) 9099–9108.
- [6] S. Bethke, “The 2009 World Average of $\alpha(s)$,” *Eur.Phys.J.* **C64** (2009) 689–703, [arXiv:0908.1135](#) [[hep-ph](#)].
- [7] S. Necco and R. Sommer, “The $N(f) = 0$ heavy quark potential from short to intermediate distances,” *Nucl.Phys.* **B622** (2002) 328–346, [arXiv:hep-lat/0108008](#) [[hep-lat](#)].
- [8] R. D. Pisarski and F. Wilczek, “Remarks on the Chiral Phase Transition in Chromodynamics,” *Phys.Rev.* **D29** (1984) 338–341.
- [9] K. Rajagopal and F. Wilczek, “Static and dynamic critical phenomena at a second order QCD phase transition,” *Nucl.Phys.* **B399** (1993) 395–425, [arXiv:hep-ph/9210253](#) [[hep-ph](#)].
- [10] J. Braun, L. Haas, F. Marhauser, and J. Pawłowski, “Phase Structure of Two-Flavor QCD at Finite Chemical Potential,” *Phys.Rev.Lett.* **106** (2011) 022002, [arXiv:0908.0008](#) [[hep-ph](#)].
- [11] S. Borsanyi *et al.*, “Is there still any T_c mystery in lattice QCD? Results with physical masses in the continuum limit III,” *JHEP* **1009** (2010) 073, [arXiv:1005.3508](#) [[hep-lat](#)].

Bibliography

- [12] S. Edwards, A. Sternbeck, and L. von Smekal, “Exploring a hidden symmetry with electrically charged quarks,” *PoS LATTICE2010* (2010) 275, [arXiv:1012.0768 \[hep-lat\]](#).
- [13] S. Edwards, A. Sternbeck, and L. von Smekal, “Fractional electric charge and quark confinement,” *PoS LATTICE2011* (2011) 264, [arXiv:1202.1477 \[hep-lat\]](#).
- [14] F. Karsch, “Deconfinement and chiral symmetry restoration,” *Proceedings of Strong and Electroweak Matter '98: Copenhagen, Denmark 2-5 December 1998* (1999) 101–111, [arXiv:hep-lat/9903031 \[hep-lat\]](#).
- [15] J. Braun and A. Janot, “Dynamical Locking of the Chiral and the Deconfinement Phase Transition in QCD,” *Phys.Rev.* **D84** (2011) 114022, [arXiv:1102.4841 \[hep-ph\]](#).
- [16] J. Braun and H. Gies, “Chiral phase boundary of QCD at finite temperature,” *JHEP* **0606** (2006) 024, [arXiv:hep-ph/0602226 \[hep-ph\]](#).
- [17] K. Yagi, T. Hatsuda, and Y. Miake, *Quark-Gluon Plasma: From Big Bang to Little Bang*. Cambridge Monographs on Particle Physics, Nuclear Physics and Cosmology. Cambridge University Press, 2008.
- [18] A. W. Steiner, J. M. Lattimer, and E. F. Brown, “The Neutron Star Mass-Radius Relation and the Equation of State of Dense Matter,” [arXiv:1205.6871 \[nucl-th\]](#).
- [19] W. Weise, “Nuclear chiral dynamics and phases of QCD,” *Prog.Part.Nucl.Phys.* **67** (2012) 299–311, [arXiv:1201.0950 \[nucl-th\]](#).
- [20] P. Braun-Munzinger and J. Wambach, “Colloquium: Phase diagram of strongly interacting matter,” *Rev.Mod.Phys.* **81** (2009) 1031–1050.
- [21] K. Fukushima and T. Hatsuda, “The phase diagram of dense QCD,” *Rept.Prog.Phys.* **74** (2011) 014001, [arXiv:1005.4814 \[hep-ph\]](#).
- [22] B. Friman, C. Höhne, J. Knoll, S. Leupold, J. Randrup, R. Rapp, and P. Senger, eds., *The CBM Physics Book: Compressed Baryonic Matter in Laboratory Experiments*, vol. 814 of *Lecture Notes in Physics*. Springer, 2011.
- [23] P. de Forcrand, “Simulating QCD at finite density,” *PoS LAT2009* (2009) 010, [arXiv:1005.0539 \[hep-lat\]](#).
- [24] M. G. Alford, A. Schmitt, K. Rajagopal, and T. Schafer, “Color superconductivity in dense quark matter,” *Rev.Mod.Phys.* **80** (2008) 1455–1515, [arXiv:0709.4635 \[hep-ph\]](#).

- [25] A. Andronic, P. Braun-Munzinger, and J. Stachel, “Thermal hadron production in relativistic nuclear collisions: The Hadron mass spectrum, the horn, and the QCD phase transition,” *Phys.Lett.* **B673** (2009) 142–145, [arXiv:0812.1186 \[nucl-th\]](#).
- [26] GSI Helmholtzzentrum für Schwerionenforschung GmbH. CBM Experiment.
- [27] A. Andronic, D. Blaschke, P. Braun-Munzinger, J. Cleymans, K. Fukushima, *et al.*, “Hadron Production in Ultra-relativistic Nuclear Collisions: Quarkyonic Matter and a Triple Point in the Phase Diagram of QCD,” *Nucl.Phys.* **A837** (2010) 65–86, [arXiv:0911.4806 \[hep-ph\]](#).
- [28] L. McLerran and R. Pisarski, “Phases of cold, dense quarks at large $N(c)$,” *Nucl.Phys.* **A796** (2007) 83–100, [arXiv:0706.2191 \[hep-ph\]](#).
- [29] Y. Hidaka, L. McLerran, and R. Pisarski, “Baryons and the phase diagram for a large number of colors and flavors,” *Nucl.Phys.* **A808** (2008) 117–123, [arXiv:0803.0279 \[hep-ph\]](#).
- [30] K. Fukushima, “Phase diagrams in the three-flavor Nambu-Jona-Lasinio model with the Polyakov loop,” *Phys.Rev.* **D77** (2008) 114028, [arXiv:0803.3318 \[hep-ph\]](#).
- [31] S. Carignano, D. Nickel, and M. Buballa, “Influence of vector interaction and Polyakov loop dynamics on inhomogeneous chiral symmetry breaking phases,” *Phys.Rev.* **D82** (2010) 054009, [arXiv:1007.1397 \[hep-ph\]](#).
- [32] J. Braun and H. Gies, “Scaling laws near the conformal window of many-flavor QCD,” *JHEP* **1005** (2010) 060, [arXiv:0912.4168 \[hep-ph\]](#).
- [33] J. Braun, C. Fischer, and H. Gies, “Beyond Miransky Scaling,” *Phys.Rev.* **D84** (2011) 034045, [arXiv:1012.4279 \[hep-ph\]](#).
- [34] K. Holland, P. Minkowski, M. Pepe, and U. Wiese, “Exceptional confinement in $G(2)$ gauge theory,” *Nucl.Phys.* **B668** (2003) 207–236, [arXiv:hep-lat/0302023 \[hep-lat\]](#).
- [35] A. Maas, L. von Smekal, B. Wellegehausen, and A. Wipf, “The phase diagram of a gauge theory with fermionic baryons,” [arXiv:1203.5653 \[hep-lat\]](#).
- [36] M. Hanada and N. Yamamoto, “Universality of Phases in QCD and QCD-like Theories,” *JHEP* **1202** (2012) 138, [arXiv:1103.5480 \[hep-ph\]](#).
- [37] A. Pelissetto and E. Vicari, “Critical phenomena and renormalization-group theory,” *Physics Reports* **368** (2002) 549–727, [arXiv:cond-mat/0012164](#).
- [38] P. Hohenberg and B. Halperin, “Theory of Dynamic Critical Phenomena,” *Rev.Mod.Phys.* **49** (1977) 435–479.

Bibliography

- [39] K. Wilson and J. Kogut, “The Renormalization group and the epsilon expansion,” *Phys.Rept.* **12** (1974) 75–200.
- [40] F. Wegner and A. Houghton, “Renormalization group equation for critical phenomena,” *Phys.Rev.* **A8** (1973) 401–412.
- [41] C. Wetterich, “Exact evolution equation for the effective potential,” *Phys.Lett.* **B301** (1993) 90–94.
- [42] J. Berges, N. Tetradis, and C. Wetterich, “Nonperturbative renormalization flow in quantum field theory and statistical physics,” *Phys.Rept.* **363** (2002) 223–386, [arXiv:hep-ph/0005122](#) [hep-ph].
- [43] H. Gies, “Introduction to the functional RG and applications to gauge theories,” [arXiv:hep-ph/0611146](#) [hep-ph].
- [44] J. Pawłowski, “Aspects of the functional renormalisation group,” *Annals Phys.* **322** (2007) 2831–2915, [arXiv:hep-th/0512261](#) [hep-th].
- [45] P. Kopietz, L. Bartosch, and F. Schütz, *Introduction to the Functional Renormalization Group*, vol. 798 of *Lecture Notes in Physics*. Springer, 2010.
- [46] B. Delamotte, “An Introduction to the nonperturbative renormalization group,” [arXiv:cond-mat/0702365](#) [cond-mat].
- [47] J. Zinn-Justin, *Quantum Field Theory and Critical Phenomena*. International Series of Monographs on Physics. Oxford University Press, USA, 2002.
- [48] M. Peskin and D. Schroeder, *An Introduction To Quantum Field Theory*. Advanced Book Program. Westview Press, 1995.
- [49] H. Gies and C. Wetterich, “Renormalization flow of bound states,” *Phys.Rev.* **D65** (2002) 065001, [arXiv:hep-th/0107221](#) [hep-th].
- [50] D. F. Litim and J. M. Pawłowski, “Completeness and consistency of renormalisation group flows,” *Phys.Rev.* **D66** (2002) 025030, [arXiv:hep-th/0202188](#) [hep-th].
- [51] D. Litim, “Optimized renormalization group flows,” *Phys.Rev.* **D64** (2001) 105007, [arXiv:hep-th/0103195](#) [hep-th].
- [52] T. Morris, “The Exact renormalization group and approximate solutions,” *Int.J.Mod.Phys.* **A9** (1994) 2411–2450, [arXiv:hep-ph/9308265](#) [hep-ph].
- [53] L. Canet, B. Delamotte, D. Mouhanna, and J. Vidal, “Nonperturbative renormalization group approach to the Ising model: A Derivative expansion at order partial**4,” *Phys.Rev.* **B68** (2003) 064421, [arXiv:hep-th/0302227](#) [hep-th].

- [54] D. Litim and D. Zappala, “Ising exponents from the functional renormalisation group,” *Phys.Rev.* **D83** (2011) 085009, [arXiv:1009.1948 \[hep-th\]](#).
- [55] D. Litim, “Critical exponents from optimized renormalization group flows,” *Nucl.Phys.* **B631** (2002) 128–158, [arXiv:hep-th/0203006 \[hep-th\]](#).
- [56] J.-P. Blaizot, R. Mendez-Galain, and N. Wschebor, “Non perturbative renormalisation group and momentum dependence of n-point functions (I),” *Phys.Rev.* **E74** (2006) 051116, [arXiv:hep-th/0512317 \[hep-th\]](#).
- [57] J.-P. Blaizot, R. Mendez-Galain, and N. Wschebor, “Non perturbative renormalization group and momentum dependence of n-point functions (II),” *Phys.Rev.* **E74** (2006) 051117, [arXiv:hep-th/0603163 \[hep-th\]](#).
- [58] N. Hasselmann, “Effective average action based approach to correlation functions at finite momenta,” [arXiv:1206.6121](#).
- [59] A. Sinner, N. Hasselmann, and P. Kopietz, “Functional renormalization group in the broken symmetry phase: Momentum dependence and two-parameter scaling of the self-energy,” *J.Phys.Condens.Matter* **20** (2008) 075208, [arXiv:0707.4110 \[cond-mat.stat-mech\]](#).
- [60] C. Wetterich. Talk at the 6th International Conference on the Exact Renormalization Group, ERG 2012.
- [61] M. Mitter, B.-J. Schaefer, N. Strodthoff, and L. von Smekal. in preparation.
- [62] O. Bohr, B. Schaefer, and J. Wambach, “Renormalization group flow equations and the phase transition in O(N) models,” *Int.J.Mod.Phys.* **A16** (2001) 3823–3852, [arXiv:hep-ph/0007098 \[hep-ph\]](#).
- [63] J. Adams, J. Berges, S. Bornholdt, F. Freire, N. Tetradis, *et al.*, “Solving nonperturbative flow equations,” *Mod.Phys.Lett.* **A10** (1995) 2367–2380, [arXiv:hep-th/9507093 \[hep-th\]](#).
- [64] F. Marhauser and J. Pawłowski, “Confinement in Polyakov Gauge,” [arXiv:0812.1144 \[hep-ph\]](#).
- [65] M. Leder, J. Pawłowski, H. Reinhardt, and A. Weber, “Hamiltonian Flow in Coulomb Gauge Yang-Mills Theory,” *Phys.Rev.* **D83** (2011) 025010, [arXiv:1006.5710 \[hep-th\]](#).
- [66] M. Jarrell, “Maximum entropy analytic continuation of quantum monte carlo data,” in *Lectures on the physics of strongly correlated systems XII: Twelfth Training Course in the Physics of Strongly Correlated Systems, Salerno, Italy, 1-12 October 2007*, A. Avella and F. Mancini, eds., vol. 1014 of *AIP conference proceedings*. American Institute of Physics, 2008.

Bibliography

- [67] M. Jarrell and J. Gubernatis, “Bayesian inference and the analytic continuation of imaginary-time quantum monte carlo data,” *Physics Reports* **269** no. 3, (1996) 133 – 195.
- [68] H. J. Vidberg and J. W. Serene, “Solving the Eliashberg equations by means of N-point Padé approximants,” *Journal of Low Temperature Physics* **29** (Nov., 1977) 179–192.
- [69] S. Floerchinger, “Analytic Continuation of Functional Renormalization Group Equations,” *JHEP* **1205** (2012) 021, [arXiv:1112.4374 \[hep-th\]](#).
- [70] H. Fujii, “Scalar density fluctuation at critical end point in NJL model,” *Phys.Rev.* **D67** (2003) 094018, [arXiv:hep-ph/0302167 \[hep-ph\]](#).
- [71] A. Arrizabalaga and U. Reinosa, “Renormalized finite temperature ϕ^4 theory from the 2PI effective action,” *Nucl.Phys.* **A785** (2007) 234–237, [arXiv:hep-ph/0609053 \[hep-ph\]](#).
- [72] A. Das, *Finite temperature field theory*. World Scientific, Singapore, 1997.
- [73] M. Le Bellac, *Thermal Field Theory*. Cambridge University Press, 1996.
- [74] G. Baym and N. D. Mermin, “Determination of thermodynamic green’s functions,” *Journal of Mathematical Physics* **2** no. 2, (1961) 232–234.
- [75] N. Dupuis, “Infrared behavior and spectral function of a bose superfluid at zero temperature,” *Phys. Rev. A* **80** (2009) 043627, [arXiv:0907.2779 \[cond-mat.quant-gas\]](#).
- [76] A. Sinner, N. Hasselmann, and P. Kopietz, “Spectral function and quasiparticle damping of interacting bosons in two dimensions,” *Phys. Rev. Lett.* **102** (2009) 120601, [arXiv:0811.0624 \[cond-mat.other\]](#).
- [77] R. Schmidt and T. Enss, “Excitation spectra and rf response near the polaron-to-molecule transition from the functional renormalization group,” *Phys. Rev. A* **83** no. 6, (2011) 063620, [arXiv:1104.1379 \[cond-mat.quant-gas\]](#).
- [78] K. Kamikado, N. Strodthoff, L. von Smekal, and J. Wambach. in preparation.
- [79] E. Svanes and J. Andersen, “Functional renormalization group at finite density and Bose condensation,” *Nucl.Phys.* **A857** (2011) 16–28, [arXiv:1009.0430 \[hep-ph\]](#).
- [80] C. Gattringer and C. Lang, *Quantum Chromodynamics on the Lattice: An Introductory Presentation*, vol. 788 of *Lecture Notes in Physics*. Springer, 2009.
- [81] T. Kanazawa, T. Wettig, and N. Yamamoto, “Singular values of the Dirac operator in dense QCD-like theories,” *JHEP* **1112** (2011) 007, [arXiv:1110.5858 \[hep-ph\]](#).

- [82] H. Georgi, *Lie Algebras In Particle Physics: from Isospin To Unified Theories*, vol. 54 of *Frontiers in Physics*. Westview Press, 1999.
- [83] G. Akemann, “Matrix Models and QCD with Chemical Potential,” *Int.J.Mod.Phys.* **A22** (2007) 1077–1122, [arXiv:hep-th/0701175](#) [hep-th].
- [84] S. Hands, I. Montvay, S. Morrison, M. Oevers, L. Scorzato, *et al.*, “Numerical study of dense adjoint matter in two color QCD,” *Eur.Phys.J.* **C17** (2000) 285–302, [arXiv:hep-lat/0006018](#) [hep-lat].
- [85] L. Pitaevskii and S. Stringari, *Bose-Einstein Condensation*. International Series of Monographs on Physics. Oxford University Press, USA, 2003.
- [86] C. Pethick and H. Smith, *Bose-Einstein Condensation in Dilute Gases*. Cambridge University Press, 2001.
- [87] I. Boettcher, J. M. Pawłowski, and S. Diehl, “Ultracold atoms and the Functional Renormalization Group,” *Nucl.Phys.Proc.Suppl.* **228** (2012) 63–135, [arXiv:1204.4394](#) [cond-mat.quant-gas].
- [88] M. M. Scherer, S. Floerchinger, and H. Gies, “Functional renormalization for the bardeen-cooper-schrieffer to bose-einstein condensation crossover,” *Philosophical Transactions of the Royal Society A: Mathematical, Physical and Engineering Sciences* **369** no. 1946, (2011) 2779–2799, [arXiv:1010.2890](#) [cond-mat.quant-gas].
- [89] S. Diehl, S. Floerchinger, H. Gies, J. Pawłowski, and C. Wetterich, “Functional renormalization group approach to the BCS-BEC crossover,” *Annalen Phys.* **522** (2010) 615–656, [arXiv:0907.2193](#) [cond-mat.quant-gas].
- [90] T. Cohen, “Functional integrals for QCD at nonzero chemical potential and zero density,” *Phys.Rev.Lett.* **91** (2003) 222001, [arXiv:hep-ph/0307089](#) [hep-ph].
- [91] T. Cohen, “Qcd functional integrals for systems with nonzero chemical potential,” in *From Fields to Strings: Circumnavigating Theoretical Physics*, M. Shifman, A. Vainshtein, and J. Wheeler, eds., Ian Kogan Memorial Collection Vol. 1. World Scientific, Singapore, 2005. [arXiv:hep-ph/0405043](#) [hep-ph].
- [92] G. Aarts, “Can stochastic quantization evade the sign problem? The relativistic Bose gas at finite chemical potential,” *Phys.Rev.Lett.* **102** (2009) 131601, [arXiv:0810.2089](#) [hep-lat].
- [93] D. Weir, “Studying a relativistic field theory at finite chemical potential with the density matrix renormalization group,” *Phys.Rev.* **D82** (2010) 025003, [arXiv:1003.0698](#) [hep-lat].
- [94] C. Gattringer and T. Kloiber, “Lattice study of the Silver Blaze phenomenon for a charged scalar ϕ^4 field,” [arXiv:1206.2954](#) [hep-lat].

Bibliography

- [95] J. Kogut, M. Stephanov, and D. Toublan, “On two color QCD with baryon chemical potential,” *Phys.Lett.* **B464** (1999) 183–191, [arXiv:hep-ph/9906346](#) [hep-ph].
- [96] J. Kogut, M. Stephanov, D. Toublan, J. Verbaarschot, and A. Zhitnitsky, “QCD - like theories at finite baryon density,” *Nucl.Phys.* **B582** (2000) 477–513, [arXiv:hep-ph/0001171](#) [hep-ph].
- [97] F. Karsch and M. Lutgemeier, “Deconfinement and chiral symmetry restoration in an SU(3) gauge theory with adjoint fermions,” *Nucl.Phys.* **B550** (1999) 449–464, [arXiv:hep-lat/9812023](#) [hep-lat].
- [98] T. Brauner, K. Fukushima, and Y. Hidaka, “Two-color quark matter: U(1)(A) restoration, superfluidity, and quarkyonic phase,” *Phys.Rev.* **D80** (2009) 074035, [arXiv:0907.4905](#) [hep-ph].
- [99] B.-J. Schaefer, J. Pawłowski, and J. Wambach, “The Phase Structure of the Polyakov–Quark–Meson Model,” *Phys.Rev.* **D76** (2007) 074023, [arXiv:0704.3234](#) [hep-ph].
- [100] C. Ratti, M. A. Thaler, and W. Weise, “Phases of QCD: Lattice thermodynamics and a field theoretical model,” *Phys.Rev.* **D73** (2006) 014019, [arXiv:hep-ph/0506234](#) [hep-ph].
- [101] J. Braun, H. Gies, and J. Pawłowski, “Quark Confinement from Color Confinement,” *Phys.Lett.* **B684** (2010) 262–267, [arXiv:0708.2413](#) [hep-th].
- [102] Z. Aouissat, G. Chanfray, P. Schuck, and J. Wambach, “A Nonperturbative treatment of the pion in the linear sigma model,” *Nucl.Phys.* **A603** (1996) 458–470, [arXiv:nucl-th/9604023](#) [nucl-th].
- [103] A. Bender, C. D. Roberts, and L. von Smekal, “Goldstone theorem and diquark confinement beyond rainbow ladder approximation,” *Phys.Lett.* **B380** (1996) 7–12, [arXiv:nucl-th/9602012](#) [nucl-th].
- [104] V. Skokov, B. Friman, E. Nakano, K. Redlich, and B.-J. Schaefer, “Vacuum fluctuations and the thermodynamics of chiral models,” *Phys.Rev.* **D82** (2010) 034029, [arXiv:1005.3166](#) [hep-ph].
- [105] C. Ratti and W. Weise, “Thermodynamics of two-colour QCD and the Nambu Jona-Lasinio model,” *Phys.Rev.* **D70** (2004) 054013, [arXiv:hep-ph/0406159](#) [hep-ph].
- [106] J. Andersen and T. Brauner, “Phase diagram of two-color quark matter at nonzero baryon and isospin density,” *Phys.Rev.* **D81** (2010) 096004, [arXiv:1001.5168](#) [hep-ph].

- [107] K. Splittorff, D. Toublan, and J. Verbaarschot, “Thermodynamics of chiral symmetry at low densities,” *Nucl.Phys.* **B639** (2002) 524–548, [arXiv:hep-ph/0204076](#) [hep-ph].
- [108] L. He, M. Jin, and P. Zhuang, “Pion superfluidity and meson properties at finite isospin density,” *Phys.Rev.* **D71** (2005) 116001, [arXiv:hep-ph/0503272](#) [hep-ph].
- [109] D. Litim and J. Pawłowski, “Non-perturbative thermal flows and resummations,” *JHEP* **0611** (2006) 026, [arXiv:hep-th/0609122](#) [hep-th].
- [110] J. Braun, “Thermodynamics of QCD low-energy models and the derivative expansion of the effective action,” *Phys.Rev.* **D81** (2010) 016008, [arXiv:0908.1543](#) [hep-ph].
- [111] L. Fister and J. Pawłowski, “Yang-Mills correlation functions at finite temperature,” [arXiv:1112.5440](#) [hep-ph].
- [112] T. Herbst, J. Pawłowski, and B.-J. Schaefer, “The phase structure of the Polyakov–quark-meson model beyond mean field,” *Phys.Lett.* **B696** (2011) 58–67, [arXiv:1008.0081](#) [hep-ph].
- [113] V. Skokov, B. Friman, and K. Redlich, “Quark number fluctuations in the Polyakov loop-extended quark-meson model at finite baryon density,” *Phys.Rev.* **C83** (2011) 054904, [arXiv:1008.4570](#) [hep-ph].
- [114] V. Skokov, B. Stokic, B. Friman, and K. Redlich, “Meson fluctuations and thermodynamics of the Polyakov loop extended quark-meson model,” *Phys.Rev.* **C82** (2010) 015206, [arXiv:1004.2665](#) [hep-ph].
- [115] J. Berges, D. Jungnickel, and C. Wetterich, “Two flavor chiral phase transition from nonperturbative flow equations,” *Phys.Rev.* **D59** (1999) 034010, [arXiv:hep-ph/9705474](#) [hep-ph].
- [116] B. Stokic, B. Friman, and K. Redlich, “The Functional Renormalization Group and O(4) scaling,” *Eur.Phys.J.* **C67** (2010) 425–438, [arXiv:0904.0466](#) [hep-ph].
- [117] S. Holtmann and T. Schulze, “Critical behavior and scaling functions of the three-dimensional O(6) model,” *Phys.Rev.* **E68** (2003) 036111, [arXiv:hep-lat/0305019](#) [hep-lat].
- [118] J. Kogut and M. Stephanov, *The Phases of Quantum Chromodynamics: From Confinement to Extreme Environments*. Cambridge monographs on particle physics, nuclear physics, and cosmology. Cambridge University Press, 2003.
- [119] B.-J. Schaefer, “Critical structure of the QCD medium,” *PoS* **CPOD07** (2007) 032, [arXiv:0709.4216](#) [hep-ph].

Bibliography

- [120] B.-J. Schaefer and J. Wambach, “The Phase diagram of the quark meson model,” *Nucl.Phys.* **A757** (2005) 479–492, [arXiv:nucl-th/0403039](#) [nucl-th].
- [121] V. Miransky, *Dynamical Symmetry Breaking in Quantum Field Theories*. World Scientific, 1993.
- [122] L. He, “Nambu-Jona-Lasinio model description of weakly interacting Bose condensate and BEC-BCS crossover in dense QCD-like theories,” *Phys.Rev.* **D82** (2010) 096003, [arXiv:1007.1920](#) [hep-ph].
- [123] J. Braun, K. Schwenzer, and H.-J. Pirner, “Linking the quark meson model with QCD at high temperature,” *Phys.Rev.* **D70** (2004) 085016, [arXiv:hep-ph/0312277](#) [hep-ph].
- [124] J. B. Kogut, D. Toublan, and D. Sinclair, “Diquark condensation at nonzero chemical potential and temperature,” *Phys.Lett.* **B514** (2001) 77–87, [arXiv:hep-lat/0104010](#) [hep-lat].
- [125] K. Fukushima, “Chiral effective model with the Polyakov loop,” *Phys.Lett.* **B591** (2004) 277–284, [arXiv:hep-ph/0310121](#) [hep-ph].
- [126] B. Lucini, M. Teper, and U. Wenger, “The High temperature phase transition in SU(N) gauge theories,” *JHEP* **0401** (2004) 061, [arXiv:hep-lat/0307017](#) [hep-lat].
- [127] S. Cotter, P. Giudice, S. Hands, and J.-I. Skullerud, “Towards the phase diagram of dense two-color matter,” [arXiv:1210.4496](#) [hep-lat].
- [128] T. K. Herbst, J. M. Pawłowski, and B.-J. Schaefer, “The Impact of Fluctuations on QCD Matter,” [arXiv:1202.0758](#) [hep-ph].
- [129] S. Hands, S. Kim, and J.-I. Skullerud, “A Quarkyonic Phase in Dense Two Color Matter?,” *Phys.Rev.* **D81** (2010) 091502, [arXiv:1001.1682](#) [hep-lat].
- [130] K. Fukushima and K. Iida, “Larkin-Ovchinnikov-Fulde-Ferrell state in two-color quark matter,” *Phys.Rev.* **D76** (2007) 054004, [arXiv:0705.0792](#) [hep-ph].
- [131] W. Detmold, K. Orginos, and Z. Shi, “Lattice QCD at non-zero isospin chemical potential,” [arXiv:1205.4224](#) [hep-lat].
- [132] D. Son and M. Stephanov, “QCD at finite isospin density,” *Phys.Rev.Lett.* **86** (2001) 592–595, [arXiv:hep-ph/0005225](#) [hep-ph].
- [133] F. Chevy and C. Mora, “Ultra-cold polarized fermi gases,” *Reports on Progress in Physics* **73** no. 11, (2010) 112401.
- [134] K. B. Gubbels and H. T. C. Stoof, “Imbalanced Fermi Gases,” [arXiv:1205.0568](#) [cond-mat.quant-gas].

- [135] F. Chevy and C. Salomon, “Thermodynamics of fermi gases,” in *The BCS-BEC Crossover and the Unitary Fermi Gas*, W. Zwerger, ed., vol. 836 of *Lecture Notes in Physics*, pp. 407–446. Springer Berlin / Heidelberg, 2012.
- [136] N. Strodthoff and L. von Smekal. in preparation.
- [137] J. Greensite, *An Introduction to the Confinement Problem*, vol. 821 of *Lecture Notes in Physics*. Springer, 2011.
- [138] P. de Forcrand and L. von Smekal, “t Hooft loops, electric flux sectors and confinement in SU(2) Yang-Mills theory,” *Phys.Rev.* **D66** (2002) 011504, [arXiv:hep-lat/0107018](#) [hep-lat].
- [139] S. Edwards and L. von Smekal, “SU(2) lattice gauge theory in 2+1 dimensions: Critical couplings from twisted boundary conditions and universality,” *Phys.Lett.* **B681** (2009) 484–490, [arXiv:0908.4030](#) [hep-lat].
- [140] L. von Smekal, “Universal Aspects of QCD-like Theories,” *Nucl.Phys.Proc.Suppl.* **228** (2012) 179–220, [arXiv:1205.4205](#) [hep-ph].
- [141] B. Svetitsky and L. Yaffe, “Critical Behavior at Finite Temperature Confinement Transitions,” *Nucl.Phys.* **B210** (1982) 423.
- [142] R. Savit, “Duality in Field Theory and Statistical Systems,” *Rev.Mod.Phys.* **52** (1980) 453.
- [143] G. ’t Hooft, “A Property of Electric and Magnetic Flux in Nonabelian Gauge Theories,” *Nucl.Phys.* **B153** (1979) 141.
- [144] L. von Smekal and P. de Forcrand, “Electric and magnetic fluxes in SU(2) Yang-Mills theory,” *Nucl.Phys.Proc.Suppl.* **119** (2003) 655–657, [arXiv:hep-lat/0209149](#) [hep-lat].
- [145] P. de Forcrand and L. von Smekal, “t Hooft loops and consistent order parameters for confinement,” *Nucl.Phys.Proc.Suppl.* **106** (2002) 619–621, [arXiv:hep-lat/0110135](#) [hep-lat].
- [146] F. Wu, “The Potts model,” *Rev.Mod.Phys.* **54** (1982) 235–268.
- [147] H. Park and M. den Nijs, “Universal finite-size-scaling amplitudes of the potts model on a torus,” *Phys. Rev. B* **38** (1988) 565–579.
- [148] C. Wozar, T. Kaestner, A. Wipf, T. Heinzl, and B. Pozsgay, “Phase structure of Z(3)-Polyakov-loop models,” *Phys.Rev.* **D74** (2006) 114501, [arXiv:hep-lat/0605012](#) [hep-lat].
- [149] A. Bugrii and V. Shadura, “Duality in 2-D spin models on torus,” [arXiv:hep-th/9706045](#) [hep-th].

Bibliography

- [150] I. Montvay and G. Munster, *Quantum fields on a lattice*. Cambridge Monographs on Mathematical Physics. Cambridge University Press, 1994.
- [151] N. Cabibbo and E. Marinari, “A New Method for Updating SU(N) Matrices in Computer Simulations of Gauge Theories,” *Phys.Lett.* **B119** (1982) 387–390.
- [152] P. de Forcrand, M. D’Elia, and M. Pepe, “A Study of the ’t Hooft loop in SU(2) Yang-Mills theory,” *Phys.Rev.Lett.* **86** (2001) 1438, [arXiv:hep-lat/0007034](#) [[hep-lat](#)].
- [153] J. Liddle and M. Teper, “The Deconfining phase transition in D=2+1 SU(N) gauge theories,” [arXiv:0803.2128](#) [[hep-lat](#)].
- [154] C. Legeland, J. Engels, F. Karsch, E. Laermann, M. Lutgemeier, B. Petersson, and T. Scheideler, “A Study of finite temperature gauge theory in (2+1)-dimensions,” *Nucl.Phys.Proc.Suppl.* **53** (1997) 420–422, [arXiv:hep-lat/9608099](#) [[hep-lat](#)].
- [155] B. Bringoltz and M. Teper, “A Precise calculation of the fundamental string tension in SU(N) gauge theories in 2+1 dimensions,” *Phys.Lett.* **B645** (2007) 383–388, [arXiv:hep-th/0611286](#) [[hep-th](#)].
- [156] P. de Forcrand and O. Jahn, “Deconfinement transition in (2+1)-dimensional SU(4) lattice gauge theory,” *Nucl.Phys.Proc.Suppl.* **129** (2004) 709–711, [arXiv:hep-lat/0309153](#) [[hep-lat](#)].
- [157] K. Holland, M. Pepe, and U.-J. Wiese, “Revisiting the deconfinement phase transition in SU(4) Yang-Mills theory in 2+1 dimensions,” *JHEP* **0802** (2008) 041, [arXiv:0712.1216](#) [[hep-lat](#)].
- [158] T. Brauner, “On the chiral perturbation theory for two-flavor two-color QCD at finite chemical potential,” *Mod.Phys.Lett.* **A21** (2006) 559–570, [arXiv:hep-ph/0601010](#) [[hep-ph](#)].
- [159] J. Braun, “The QCD Phase Boundary from Quark-Gluon Dynamics,” *Eur.Phys.J.* **C64** (2009) 459–482, [arXiv:0810.1727](#) [[hep-ph](#)].

Danksagung

An erster Stelle möchte ich mich bei Priv. Doz. Dr. Lorenz von Smekal bedanken für seinen Enthusiasmus, seine Neugier und die Vielzahl an physikalischen Einsichten, die er mit mir in endlosen Diskussionen geteilt hat. Seine Tür stand stets offen für mich, egal wie bedrohlich nah die nächste Deadline schon wirkte. Ebenso möchte ich mich bei Prof. Dr. Jochen Wambach für seine durchgehende Unterstützung in den letzten drei Jahren und an dieser Stelle auch noch einmal explizit für die Laudatio auf den HGS HIRe Graduate Days bedanken.

Ich möchte diese Gelegenheit auch nutzen, um mich für die gute und produktive Zusammenarbeit bei Sam Edwards, Kazuhiko Kamikado, Mario Mitter, Prof. Dr. Jan Pawlowski, Priv. Doz. Dr. Bernd-Jochen Schaefer und Prof. Dr. Jochen Wambach zu bedanken, die mir viel Spaß bereitet hat. Ich freue mich auf eine weitere Zusammenarbeit in der Zukunft.

Ebenso bedanke ich mich bei Jacqueline Bonnet, Pascal Büscher, Stefano Carignano, Raphael Flore, Dr. Markus Huber, David Scheffler und Arno Tripolt für interessante Gespräche über physikalische als auch nicht-physikalische Themen. Hervorheben möchte ich auch die besonders harmonische Atmosphäre innerhalb des Instituts, die ich an meiner Zeit in Darmstadt in besonderer Erinnerung behalten werde.

Für die finanzielle Unterstützung bedanke ich mich bei der Helmholtz Graduate School for Hadron and Ion Research.

Der größte Dank jedoch gebührt meiner Familie, meinen Eltern und meinem Bruder Claas, auf deren Unterstützung ich immer zählen kann.

Curriculum vitae

Name: Nils Strodthoff
Date of birth: 16/06/1985
Place of birth: Bremen
Marital status: single

Education and degrees:

1997-2004 Grammar School Cato-Bontjes van Beek Gymnasium Achim
23/06/2004 Higher education entrance qualification (grade: 1,0)
2004-2005 Military service: Lazarettregiment 31, Berlin and Wehrbereichsmusikkorps 1, Lüneburg
2005-2008 Study of Physics at Georg-August Universität Göttingen
24/10/2007 Vordiplom in Physik (grade: 1,0)
2008-2009 MSc course *Quantum Fields and Fundamental Forces* at Imperial College London
01/11/2009 MSc in *Quantum Fields and Fundamental Forces* with distinction
2009-2012 Postgraduate Study at Technische Universität Darmstadt